POLITECNICO DI MILANO

Scuola di Ingegneria Industriale

Corso di Laurea Magistrale in Ingegneria Energetica

APPLICATION OF NON-UNIFORM STEADY MAGNETIC FIELDS TO ENHANCE THE HEAT TRANSFER IN LIQUID METAL FLOWS

Relatore: Prof. Andrea Lucchini

Relatori esteri: Prof. Piero Colonna, Dr. Ing. Mauro Gallo

Tesi di Laurea di:

PASQUALE ATTROTTO

Matricola: 771363

Anno Accademico 2012-2013

Table of Contents

List of Figures

List of Tables

List of Symbols

Roman symbols

$\mathbf{A}$	vector magnetic potential	$T \cdot m$
A_c	flow cross-sectional area	m^2
$\mathbf{B}$	magnetic field	T
$\mathbf{B_{imp}}$	imposed magnetic field	T
$\mathbf{B_{ind}}$	inducted magnetic field	T
c_{v}	specific heat capacity at constant volume	J/kgK
c_{p}	specific heat capacity at constant pressure	J/kgK
D_H	hydraulic diameter	m
dw	distance between two consecutive wires	$-$
dwz	the distance of wires form the walls	$-$
$\mathbf{E}$	electrostatic field	$\frac{V}{m}$
$\mathbf{E_i}$	electrostatic field induced by a time-variant magnetic field	$\frac{V}{m}$
$\mathbf{E_s}$	electrostatic field induced by a charge distribution	$\frac{V}{m}$
$\mathbf{f}$	volumetric Lorentz force	$\frac{N}{m^3}$
$\mathbf{f_c}$	Lorentz force	N
H_a	Hartmann number	$[-]$
h	convective heat transfer coefficient	$\frac{W}{m^2 \cdot K}$

$\mathbf{I}$	electric current	A
$\mathbf{I_{enc}}$	enclosed electric current	A
$\mathbf{J}$	electric current density	$\frac{A}{m^2}$
k	thermal conductivity	$\frac{W}{m \cdot K}$
$\dot{m}_{\text{flow}}$	mass flow rate	kg/s
mfw	coordinate of the first wire	$-$
mlw	distance between the last wire and the end of the channel	$-$
N	Stuart number	$[-]$
nw	number of wires	$[-]$
P	power	W
p	pressure	Pa
Pe	Peclet number	$[-]$
Pe_τ	Friction Peclet number	$[-]$
Pr	Prandtl number	$[-]$
px	number of processors working in parallel	$[-]$
$\mathbf{q}$	heat flux	$\frac{W}{m^2}$
$\mathbf{q_w}$	heat flux on the wall	$\frac{W}{m}$
R	electric resistivity	Ω
r	radius	m
Re	Reynolds number	$[-]$
Re_τ	Friction Reynolds number	$[-]$
R_m	magnetic Reynolds number number	$[-]$
S	surface	m^2
T	temperature	K
T_c	Curie temperature	K
T_m	fluid bulk mean temperature	K
$T_{m,w}$	wall mean temperature	K
t	time	s
$\mathbf{u}$	velocity field	$\frac{m}{s}$
u	velocity component in streamwise direction	$\frac{m}{s}$
u_i	specific internal energy	$\frac{kJ}{Kg}$
u_b	bulk velocity	$\frac{m}{s}$
u_τ	Friction velocity	$\frac{m}{s}$
V	electrostatic potential	V
v	velocity component in span wise direction	$\frac{m}{s}$
w	velocity component in orthogonal to plates direction	$\frac{m}{s}$

Greek symbols

α	thermal diffusivity	$\frac{m^2}{s}$
λ	volumetric viscosity	$\frac{m^2}{s}$
λ_m	magnetic diffusivity	$\frac{m^2}{s}$
ϵ_0	vacuum permittivity	$\frac{F}{m}$
μ	dynamic viscosity	$Pa \cdot s$
μ_0	magnetic permeability of the free space	$\frac{H}{m} = \frac{N}{A^2}$
μ_m	magnetic permeability	$\frac{H}{m} = \frac{N}{A^2}$
μ_r	relative magnetic permeability	$-$
ν	kinematic viscosity	m^2/s^2
ξ	energy source term	$\frac{W}{m^3}$
ρ	density	$\frac{kg}{m^3}$
ρ_{cond}	electric resistivity	$\Omega \cdot m$
$\rho_e l$	electric density	$\frac{C}{m^3}$
σ	electric conductivity	$(\Omega \cdot m)^{-1}$
τ_e	charge relaxation time	s
χ	magnetic susceptibility	$-$

“Ergo qui desiderat pacem, præparet bellum.”
"If you wish for peace, prepare for war."

— *Publius Flavius Vegetius Renatus, Epitoma rei militaris, Book 3*

Abstract

One of the most effective ways to improve the efficiency of a gas turbine-based power plant is to increase the turbine inlet temperature (TIT). The latter, limited by the thermomechanical resistance of the blades material, is enhanced by cooling the blades from inside. The air cooling systems currently used have already reached such a complexity level that a drastic increase of the TIT may be possible only by using better heat transfer fluids as coolants, in particular liquids.

Due to many technological reasons, that are recalled and discussed here, liquid cooling systems did not reach commercial development so far. This work aims at boosting research in order to overcome these problems, by presenting a new high-potential concept for blade cooling with liquid metals as coolants.

Thanks to the high electric conductivity of liquid metals, it is possible to influence their flow by means of an external magnetic field. This can be specifically designed in order to enhance the heat exchange at the walls of the cooling channel, therefore allowing even higher TIT or lower blades temperatures. Furthermore, if the magnetic field is produced by electric currents the cooling intensity can be adjusted according to the thermal loads on the blades. Also a local control of the heat transfer coefficient would be possible in order to enhance the uniformity of temperature into the blades, reducing the thermal stresses. As a consequence the operating life of the gas turbine blades can also increase, with clear economic benefit.

Preliminary heat transfer simulations are performed on a simplified model of turbine blade. By using lithium as coolant, even in laminar regime, the maximum wall temperature is 300°C lower than the one with air flowing at high Reynolds number. Metals are able to achieve intense cooling, therefore to reduce the criticality related to the generation of magnetic fields at high temperatures.

Direct numerical simulations of a liquid metal flow in laminar regime between parallel plates are carried out. The heat transfer enhancement produced by different non-uniform magnetic fields is investigated. An increase of the Nusselt number up to 35% is achievable in a sodium flow by means of magnetic fields whose intensity is around 0.1 Tesla.

Keywords: turbine blades cooling, liquid metals, magnetohydrodynamics, direct numerical simulations.

Sommario

Una delle vie più efficaci per ottenere un aumento dell'efficienza in impianti di potenza basati su turbine a gas consiste nell'incremento della TIT (Turbine Inlet Temperature).

La vita utile delle pale di turbina è limitata dall'incorrere di fenomeni come *creep* viscoso, corrosione e fatica oligociclica. L'effetto di tali fenomeni si intensifica al crescere delle temperature operative che pertanto devono essere limitate.

La TIT delle turbine a gas commerciali è aumentata circa linearmente nel tempo nel corso degli ultimi decenni. La resistenza termica delle pale è migliorata grazie all'impiego di materiali sempre più pregiati ed all'utilizzo di processi di produzione sempre più sofisticati. La TIT è cresciuta anche per effetto dell'incremento di efficienza dei sistemi di raffreddamento delle pale. È ragionevole pensare che con il raffreddamento ad aria non saranno possibili ulteriori significativi incrementi di TIT, che potrebbero invece essere raggiunti impiegando refrigeranti più efficaci.

Nonostante le eccezionali proprietà di scambio termico dei liquidi, nessun sistema di raffreddamento a liquidi ha finora trovato sviluppo commerciale. Le principali ragioni sono le seguenti:

- gran parte degli investimenti nella ricerca sulle turbine a gas vengono fatti nel campo delle applicazioni aeronautiche. Il peso aggiuntivo che comporterebbe l' implementazione di un sistema di raffreddamento a liquido è un grande ostacolo perchè ridurrebbe la capacità dell'aeromobile in termini di carico pagante (*pay load*);
- le elevate velocità di rotazione dei rotori di turbina rende estremamente difficile la progettazione di un sistema affidabile per la circolazione del liquido;
- il peso del refrigerante liquido all'interno delle pale costringe a realizzare queste ultime con un profilo più robusto, dunque non ottimale da un punto di vista fluidodinamico.

Tra i liquidi acqua e metalli sono tra i migliori fluidi di scambio termico. I metalli liquidi presentano due vantaggi principali rispetto all'acqua:

- alcuni metalli sono meno densi dell'acqua, quindi comportano un minor carico centrifugo sulle pale rotoriche;
- avendo pressioni di vapore minori dell'acqua, i metalli liquidi possono fluire nei canali di raffreddamento a pressioni ridotte.

In questo lavoro di tesi si propone un sistema innovativo per la promozione dello scambio termico in un sistema di raffreddamento a metalli liquidi. L'idea presentata consiste nello sfruttare una caratteristica che distingue i metalli liquidi da altri fluidi: l'elevata conducibilità elettrica. Grazie a questa proprietà è possibile influenzare il flusso di un metallo liquido per mezzo di un campo magnetico esterno. Lo scambio termico tra pala e metallo può essere così incrementato permettendo TIT ancora maggiori. Se il campo magnetico viene prodotto per mezzo di correnti elettriche è inoltre possibile variarne facilmente l'intensità. In questo modo si può regolare l'entità del raffreddamento a seconda del carico termico sulla pala. Un controllo locale del coefficiente di scambio termico può anche essere sfruttato per migliorare l'uniformità della temperatura all'interno della pala riducendo così gli stress termici.

È stata condotta una valutazione semplificata dell'elevato potenziale dei metalli come fluidi refrigeranti. Si è considerato un condotto cilindrico investito ortogonalmente al suo asse da un flusso di aria calda ad alta velocità. Facendo scorrere aria internamente al condotto la massima temperatura della parete cilindrica supera i 900 °C, mentre i metalli si mostrano capaci di raffreddamenti molto più intensi. In particolare il litio mantiene la massima temperatura di parete di poco superiore a 600 °C. La generazione di un campo magnetico diventa sempre più critica all'aumentare della temperatura. La capacità dei metalli di raffreddare efficacemente le pale è fondamentale per ridurre questa criticità e rendere fattibile l'innovativo sistema proposto.

Per mezzo di un codice DNS (Direct Numerical Simulation) è stato simulato il flusso di un metallo liquido tra due lastre piane. Dei fili conduttori ideali percorsi da corrente elettrica continua generano un campo magnetico non uniforme. Essi sono posizionati dietro le due lastre e sono diretti ortogonalmente alla direzione del flusso. Quattro diverse configurazioni dei fili sono state valutate sulla base del loro effetto sulla distribuzione del numero di Nusselt lungo il canale. La configurazione più interessante presenta tutti i fili disposti dietro la medesima lastra e correnti in due fili adiacenti dirette nei versi opposti. Questa configurazione produce un considerevole aumento del coefficiente di scambio termico su una delle due pareti. Quando il flusso incontra il campo magnetico il numero di Nusselt cresce rapidamente portandosi ad un valore medio costante intorno al quale oscilla leggermente. Le altre configurazioni producono o distribuzioni più irregolari del numero di Nusselt o oscillazioni più ampie oppure incrementi più limitati.

Viene studiata l'influenza dei parametri adimensionali caratterizzanti il fenomeno. Questi parametri sono il numero di Reynolds, il numero di Prandtl, il numero di Stuart, la distanza tra i fili e la distanza dei fili dalla parete (dwz). La promozione dello scambio termico si intensifica al ridursi di dwz e dw e al crescere del numero di Reynolds e del Numero di Stuart. Quest'ultimo, meno noto degli altri, rappresenta il rapporto tra la forza di Lorentz e le forze di inerzia. Il Prandtl, nel range di valori che esso assume per i metalli liquidi ($10^{-2} \div 10^{-3}$), non influenza in maniera sensibile l'azione del campo magnetico sulla promozione dello scambio termico convettivo.

È stato inoltre analizzato un caso dimensionale: un flusso di sodio in regime laminare ($Re_{D_H} = 2000$) tra lastre distanti 5 mm l'una dall'altra. Risulta che un aumento del 35 % del numero di Nusselt può essere ottenuto per mezzo di un campo magnetico il cui valore massimo all'interno del canale è 0.11 Tesla. L'intensità del campo magnetico, a parità di incremento del numero di Nusselt, risulta inversamente proporzionale alla distanza tra le lastre.

Chapter 1

Introduction

It is well known that one of the most effective ways to improve gas turbines efficiencies and reach higher specific work outputs is to operate at higher Turbine Inlet Temperature (TIT). Although high temperatures, of the order of 2500 K, corresponding to the combustion of fuel under stoichiometric conditions, are theoretically possible, such temperatures can not be reached in practice. The best heat-resisting steels and alloys available nowadays can operate with gas temperatures of about 1200 K in long-life. This limitation is due mainly to:

- creep: this phenomenon causes slow but permanent deformation of a solid material under steady stress below the yield strength. Creep of a turbine blade will cause the blade to contact the casing, resulting in the failure of the blade. Creep always increases with temperature;
- corrosion: it caused by the high reactivity of the oxygen at high temperature;
- cycle fatigue: due to severe stress generated by thermal transients.

This difficulty is overcome nowadays, at a high cost in fuel consumption, by pumping more air than is actually required for combustion and using this excess to dilute the combustion products. The gases are thus delivered for expansion in the turbine at a temperature sufficiently low to allow an adequate life for the various turbomachinery components. To mitigate the reduction of efficiency due to this cause, much effort has been and is being expended on the use of means of improvement [2]. These can be distinguished in two main categories:

- development of new materials with ever higher thermal resistance threshold;
- development of cooling systems in order to allow higher TIT, keeping the blades temperature below their thermal resistance threshold.

The cooled parts in a gas turbine are disks, turbine case and above all the first $3 \div 4$ blades arrays, which are the most critical components, since they are directly crossed by the combustion gases hot flow. Currently, commercial gas turbines have open circuit air cooling systems: part of the air intaken by the compressor is bled and is used as coolant, afterwards it is mixed to the main flow of hot gases expanding into the turbine.

This system is relatively simple but it has some limits:

- part of the compressed air bypasses the combustor. Instead of being used as combustive agent, it is used as coolant. The fuel burned, is therefore less than that possible if all the compressed air was sent to the combustor, being equal the TIT. This, clearly, limits the gas turbine power;
- air is not a good heat transfer fluid. It has low heat capacity, low thermal conductivity and low density. The volumetric flow necessary for an effective cooling is therefore very high (around 20 % of the air intaken by the compressor). Being air a gas the work required for its compression is quite high, so the cycle efficiency is penalized. However, obviously the efficiency increase due to an higher TIT is greater;
- the air, after having cooled the turbine blade, mixes with the main flow, which so is cooled down an is therefore affected by a reduction of specific volume. The work of an expanding gas is $\int v \cdot dp$, so the turbine power is further penalized. Moreover, the main fluid stream is disturbed by the cooling flows when they are mixed, so it is hard to keep the optimal triangles of speed.

In the last sixty years the TIT of commercial gas turbine has been increasing about 12 K per year as it is shown in Figure 1-1.

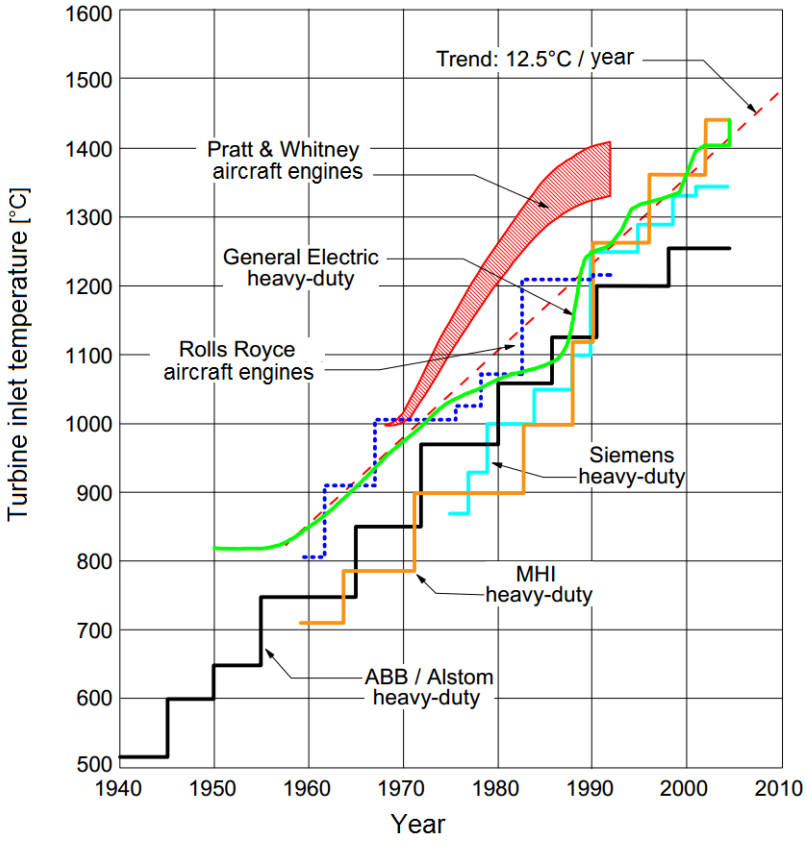

Figure 1-1: TIT trend in commercial gas turbines over time [3]

The thermal resistance threshold of materials has been increasing about $5K$ per year. The difference between this two values is $7K$ and it is due to the improving of cooling techniques.

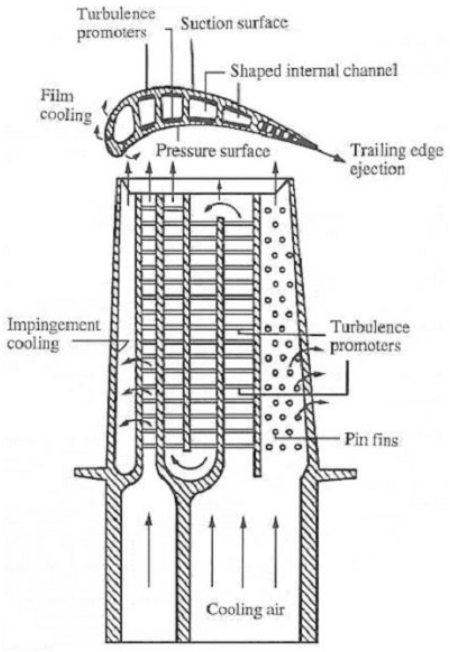

Figure 1-2: Typical internal cooling arrangement for a turbine blade [4]

Several heat transfer mechanisms are involved in gas turbine blades air cooling systems (Figure 1-2). The leading edge of the blade, which is the part exposed to the highest thermal load, is cooled by means of *impingement jets*. The central part of the blade is cooled by means of *internal forced convection*: the air passes through a serpentine-like cooling channel. This cooling channels are provided with turbulence promoters (*ribs*). They allow an heat transfer increase through the increasing of the turbulence, but also through the generation of impinging flows [5]. The region of the blade toward the trailing edge is cooled down by *pin fins*.

The currently implemented air cooling systems show very high complexity. It is reasonable to envisage that no big further improvement by air cooling can be obtained. This thesis work stems from the idea of an innovative cooling system, which leads to a drastic increase of TIT, therefore of the conversion efficiency of power plants.

The idea is to use a liquid metals as coolant. All the three disadvantages of current cooling systems listed above would be eliminated. Liquid metals in fact, as opposed to air, have high heat capacity, high density and high thermal conductivity. Their thermophysical properties make liquid metals excellent heat transfer fluids, capable of cooling high-density thermal sources, and diffuse thermal energy in confined space. Actually, not only an increase of the TIT could be achievable, but also lower hot sections part temperature, so a relevant cost reduction of the equipment, because less expensive materials could be employed.

Another noticeable physical property of liquid metals is their high electric conductivity. On this property is based the actual innovation of the idea proposed in this thesis. The high electric conductivity makes, in fact, liquid metals even more attractive from the technological point of view. Indeed, thanks to it is possible by a non-uniform and unsteady magnetic field to influence, in a controlled way, the structure of a liquid-metal flow with strong effects on

heat transfer to the wall.

An arguably innovative feature of the proposed cooling concept is chance to easily adjust it. Indeed if the magnetic field is produced by electric currents, its intensity can be rapidly changed acting on the electric current. This could be useful to adjust the intensity of the cooling depending on the TIT that varies with the turbine load.

The thesis is organized laid down as follows. In Chapter 2 a review of liquid cooling systems for gas turbine blades is given. The main liquid cooling methods studied and tested experimentally are described, with a particular focus on liquid metals as coolants. The technological barriers that have so far prevented the commercial development of these systems are recalled.

A simple numerical model of a blade cooling channel is constructed and used to evaluate the great potential of liquid metals as coolants with respect to air. In Chapter 3 the results of calculations made with this model are presented. The low wall temperatures achievable by using liquid metals are very important to make feasible the generation of a magnetic field inside the cooling channels.

Chapter 4 provides an introduction to Magnetohydrodynamics (MHD), the branch of physics dealing with interactions between electrically conductive fluid flows and magnetic fields [6]. The physics of characteristic phenomena is described and the governing equations are illustrated.

Some numerical simulation are carried out in order to evaluate the influence of non-uniform magnetic fields on a liquid metal flow. Changing some relevant parameters, the effects of magnetic fields on the velocity field and the heat transfer are presented. The simulations are carried out by means of a direct mumerical simulation (DNS) code, whose general description is given in Chapter 5. The simulation results are shown and commented in chapter 6.

Finally, Chapter 7 draws some conclusion of this thesis work.

Chapter 2

Turbine liquid cooling

2-1 Liquid cooling methods

An internal liquid cooling systems may be based on forced convection or free convection.

FORCED CONVECTION It is the same mechanism currently used for air cooling. The liquid is pumped through channels inside the blades, absorbing heat and keeping low the blades temperature.

The main advantage of the forced-convection liquid-cooling method is the potential for obtaining low metal temperatures, because high velocities are feasible. Some other advantages of this system are the simplicity and easy recovery of heat from spent coolant [1], in fact an heat exchanger external to the turbine can be used, unlike in two of the three free convection systems presented afterwards.

Current technology liquid metal pumps were found to be heavy and cumbersome, but with liquid metals could be also used electromagnetic pumps. These exploit the action of a magnetic field to induce the movement of the liquid metal fluid. Electromagnetic pumps are lighter and less bulky so they could be more suitable for aircraft applications. They have lower efficiency than conventional pumps, but the power required for the liquid pumping should be low, so the low efficiency of the pump should not be a problem.

A forced convection system can be used both for rotors and stators blades cooling.

FREE CONVECTION Systems for rotating blades called **thermosyphons** are based on natural convection.

The fluid motion is caused by a density difference, caused by a temperature difference, in a body force field. In the case of turbine wheel the body force field is the centrifugal force field due to rotation, and it is proportional to the product of the radius and the square of rotational speed. This can be as high as $20000 \div 30000$ g's for a typical turbine; thus, there is a large potential for heat transfer [1].

The basic types of thermosyphon studied and experienced are three: closed thermosyphon, open thermosyphon, closed-loop thermosyphon.

The **closed thermosyphon** is illustrated in figure 2-1 (a). A primary coolant heats up flowing into the blade cooling passages and then goes into an heat exchanger where gives up heat to a secondary coolant. Each cooling passage is a closed tube with the primary heat-transfer media sealed inside. Primary coolant near the tube wall is heated in the blade cooling passage; this hot, less dense, coolant flows and is displaced by cold, more dense fluid from the heat exchanger. This process is illustrated in figure 2-1 (b). In the heat exchanger end of the tube, heat is removed from the primary fluid near the tube wall. This cool, more dense fluid moves outward. In the region between the heat exchanger and the blade cooling passage hot and cold fluids collide. Hot fluid flowing in annular-type flow in the cooling passage must find its way to the central core in the heat exchanger end and vice versa for the cold fluid in the heat exchanger. Several possible mechanisms for this transfer exist, and they are discussed in ref. [1]. A secondary coolant removes heat from the heat exchanger and carries it away.

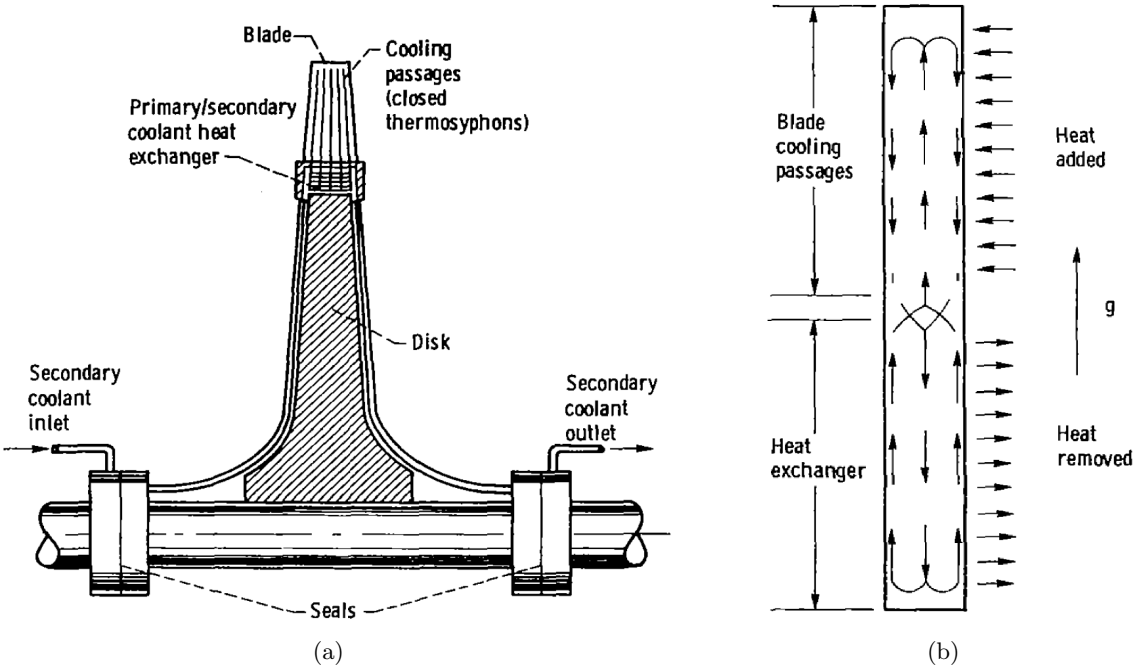

Figure 2-1: Closed thermosyphon system (a) and detail of a channel (b) [1]

Figure 2-2 shows the **open thermosyphon** system. The coolant enters a cavity or reservoir at the base of the blade. Cooling passages in the blade are open to this reservoir, and the fresh, more dense coolant in the reservoir displaces the hot fluid in the cooling passages. The hot fluid from the blade then mixes with the fluid in the reservoir that is continually being drained off and replaced with a cool fluid from the inlet. Each cooling passage is a closed tube as for the closed thermosyphon; Figure 2-3 shows the cross section of a single cooling passage. Fluid pressure at the blade tip is a function of the location of the free surface in the reservoir; thus, pressure within the blade can be higher than that for closed thermosyphon. If the length to diameter ratio of the thermosyphon is too large, performance will suffer because of the growth and mixing of the boundary layers of hot and cold fluids flowing in opposite

directions [1].

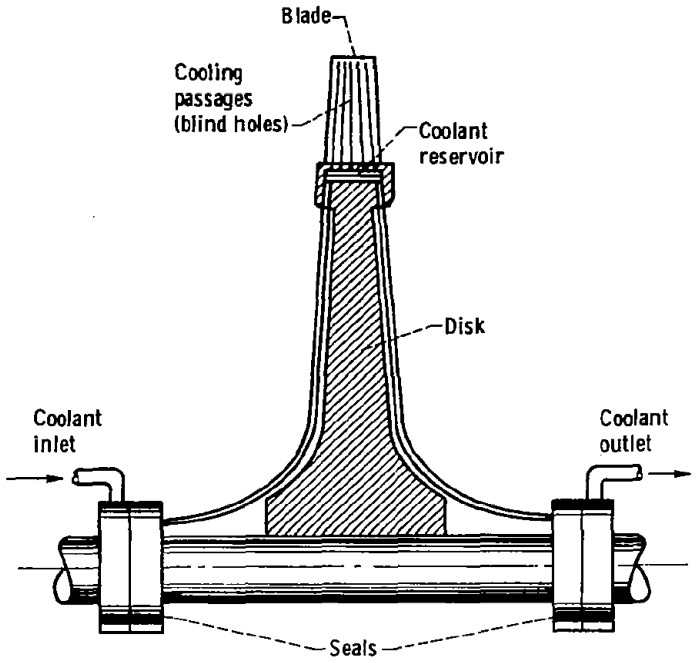

Figure 2-2: Open thermosyphon system [1]

The third type of thermosyphon is the **closed-loop thermosyphon**, shown in Figure 2-4 (a) in a possible turbine blade cooling configuration. Instead of the coolant flowing in two directions simultaneously in the cooling passages as in the closed or open thermosyphons, it flows in one direction in each passage. Cool, more dense fluid moves radially outward through the large central feed passages and is then manifolded at the tip to flow radially inward through the small cooling passages around the perimeter of the blade. Heated fluid in the cooling passages then moves inward to a heat exchanger where it is cooled by a secondary coolant. Details of the blade cooling passages and heat exchanger are depicted in Figure 2-4 (b).

The closed-loop thermosyphon has the same advantages and disadvantages as the closed thermosyphon respect to the open termosyphon. Two are the main disadvantages of all the closed systems. One is that if the primary coolant escapes through cracks all cooling stops, the blade temperature increase beyond the alloy resistance limits and the blade is irreversibly damaged. Conversely, open-loop thermosyphon system coolant leaks in the blade would not lead to blade failure from loss of coolant. The second disadvantage is that the closed systems require a primary to secondary coolant heat exchanger. It may be difficult to find adequate space on the turbine wheel for this and it may also be costly [1].

The advantage of closed systems is that they allow a wider choice of primary coolant since substances which would be unacceptable in the open thermosyphon because of toxicity, chemical instability, cost or sheer weight would be permanently enclosed in the completely-sealed tube. This brings liquid metals into the practical range of consideration as primary coolant [7]. Moreover, since the closed systems are completely sealed, clogging by foreign matter in

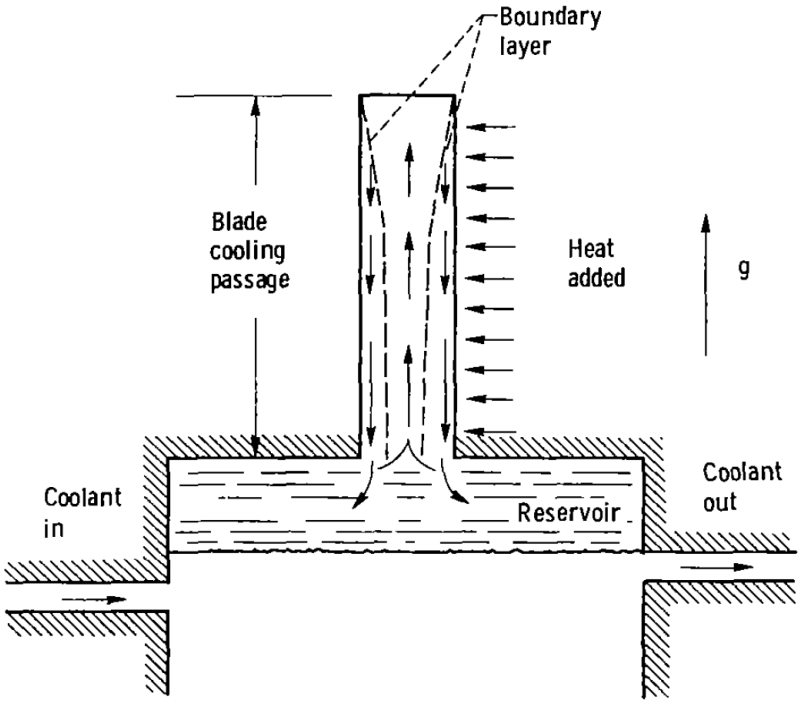

Figure 2-3: Open thermosyphon channel [1]

the coolant is not a problem, unlike open thermosyphon sysyem, where foreign matter in the coolant can collect at the blade tips because the cooling passages are blind holes.

In the closed-loop thermosyphon, because flow is unidirectional in all the passages, much longer passages can be utilized respect to the other two systems. Long, thin passages may be necessary in the turbine application to minimize thermal gradients within the blades.

Secondary coolant In a closed system fuel could be used as secondary coolant. It would be warmed up before entering in the combustion chamber [8]. The same could be done with combustive air. In both cases a good global efficiency could be gained, because less fuel would be needed to reach the same TIT, but the system complexity would grow up. Combustive air or fuel as secondary coolant would be applicable to aircraft systems, because they don't involve additional weight, while water, which has better heat exchange properties, could be used for ground-based machines.

2-2 Liquid coolants

Water Everybody knows how good is water as a heat-transferring medium by virtue of its high thermal conductivity, to say nothing of its non-toxic nature, chemical inertness and abundance. Of course to not incur in corrosion problems, water has to be strongly desalinated. Could be used both as primary and secondary coolant. Water has the one great disadvantage in that its critical temperature is so to keep it in the liquid status very high pressure could be needed [2].

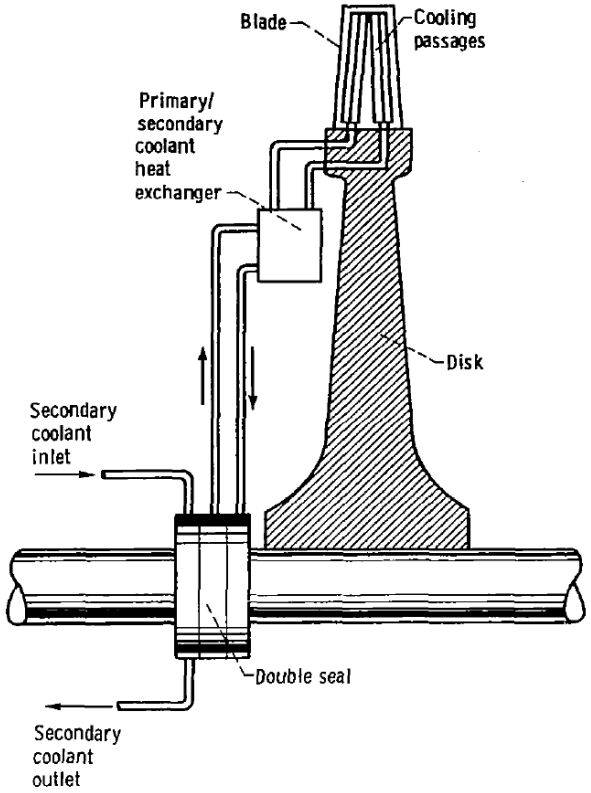

(a)

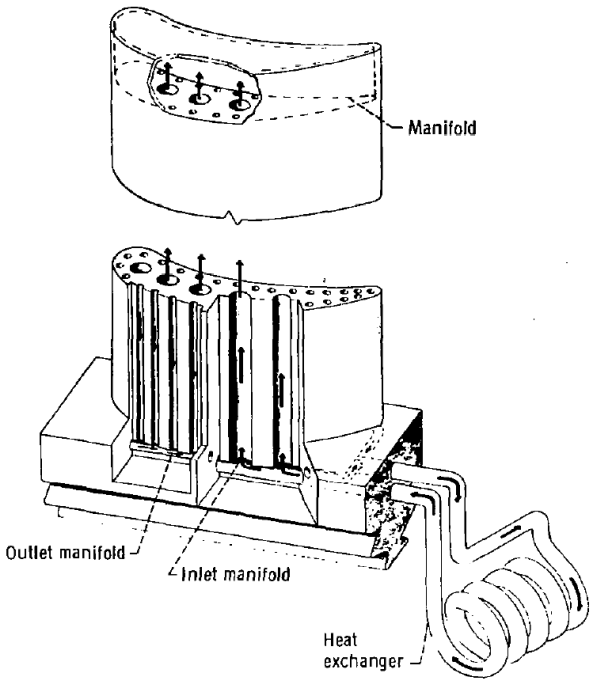

(b)

Figure 2-4: Closed-loop thermosyphon system (a) and details of blade cooling passages and heat exchanger (b) [1]

Liquid metals Low vapour pressure of liquid metals allows to low pressures inside the cooling channel. Another advantage of liquid metals over water is the smaller density of some of them, which means less mass, so lower mechanical load due to the centrifugal acceleration on the rotor blades. Some past attempts to use liquid metals for gas turbine cooling have failed due to chemical reaction between impurities, the liquid metal and the container. However a great deal of work has been done in the 70's in the USA and in Britain in connection with nuclear power systems, in particular those for use in space and for fast reactors. Using the correct techniques it should be possible to obtain lives of thousands of hours from liquid metal devices. The corrosion problem can largely be overcome by eliminating all traces of oxygen from the system and using 'getters' such as barium and zirconium. These also improve the wetting properties of the fluid [8].

Although nickel based alloys, which blades are made from, are not readily attacked by alkali metals they are slightly soluble at high temperatures. In non-evaporating systems metal will dissolve preferentially in the hotter parts of the system and be deposited in the cooler part. Refractory metals such as tungsten and molybdenum have very low solubilities in alkali metals but have very little oxidation resistance and are thus unsuitable for parts in contact with hot combustion gases. The problem could most likely be solved by using a refractory metal lining in a nickel alloy blade assembly. Thus could either be a fabricated liner with the nickel alloy cast around it, or a vapour deposited internal coating. This liner would also serve as a barrier against diffusion of alloying elements and adsorbed gases into the liquid metal [8].

2-3 Problems of liquid cooling

Some studies have been done on liquid cooling methods and also some experimental systems and demonstrator turbines have been built and tested. With regards to liquid metals, C. Henry and F. Bayley [2] describe some some interesting experimental tests made with sodium-potassium alloys. G. Fossen and S. Stepka [1] describe some some tests made with Mercury as coolant.

These works show in general considering thermodynamic advantages of liquid cooling on air cooling so it is reasonable to inquire why the liquid cooling methods described in the first paragraph of this chapter did not yet find commercial applications. There are several reasons. In the first place, the greatest success of the gas turbine has been in the aircraft engines field and especially in this field a lot of money are invested in research. Liquid cooling systems, especially those which require the carriage of large volumes of liquid, involve an extra weight. In the aircraft applications, as well known, is very important the gas turbines weight to be the smallest possible to allow the increasing of the "pay-load" of the aircraft.

Secondly, the mechanical difficulties of designing a reliable liquid-circulating system for high-speed turbine rotors have posed a formidable and, so far, an insuperable barrier even for marine and industrial engines.

Moreover, extra blade weight is a problem, not only because it directly adds to the total engine weight, but also because it increases the centrifugal loading on the blade and disc. The blades should be, therefore, more robust penalizing the rotor stage effectiveness.

Finally, liquid cooling system are more applicable to ground-based turbines. This is because the engine weight and design considerations used to incorporate liquid cooling into ground-based applications are less critical than those used in aircraft applications [1].

The ambition of this thesis work is to undertake a research course that gives a further reason to try to overcome these barriers to the development of commercial application with liquid cooling. This new stimulus is the advantages that a control of liquid metal flows inside the cooling channel by magnetic field can give.

Chapter 3

A magnetic field in a blade cooling channel

3-1 Magnetic field generation

From a physical point of view a magnetic fields can be generated by:
- intrinsic magnetic moments of elementary particles associated with a fundamental quantum property, their spin;
- moving electric charges.

From a practical point of view two kind of devices exist that can generate a magnetic field. These are **permanent magnets**, which are based on the first of the two point listed above, and **wires current carrying** or **electromagnets**, which are based on the second point.

3-1-1 Permanent magnets

In all materials each atom has a tiny magnetic dipole; it comes mainly from the quantum mechanical spin, but there is also a contribution from the orbital angular momentum of the electron about the nucleus. Based on the relative position of the magnetic dipoles of atoms in materials, four main structures of intrinsic magnetic moments can be distinguished: paramagnetism, ferromagnetism, ferrimagnetism and antiferromagnetism. Figure 3-1 shows this four main structures.

In ferromagnetic materials the moments are aligned and of the same magnitude. In ferrimagnetic materials there are moments whit two different magnitudes. The two kind of moments are aligned opposite, but since they have different magnitude a macroscopic magnetic field results. In antiferromagnetic materials there are two kind of moments. They are aligned opposite and have the same magnitude so no macroscopic magnetic field results.

For every material ferromagnetic or ferrimagnetic or antiferromagnetic a critical temperature exists, above which the thermal motion competes with the tendency for dipoles to align, so the

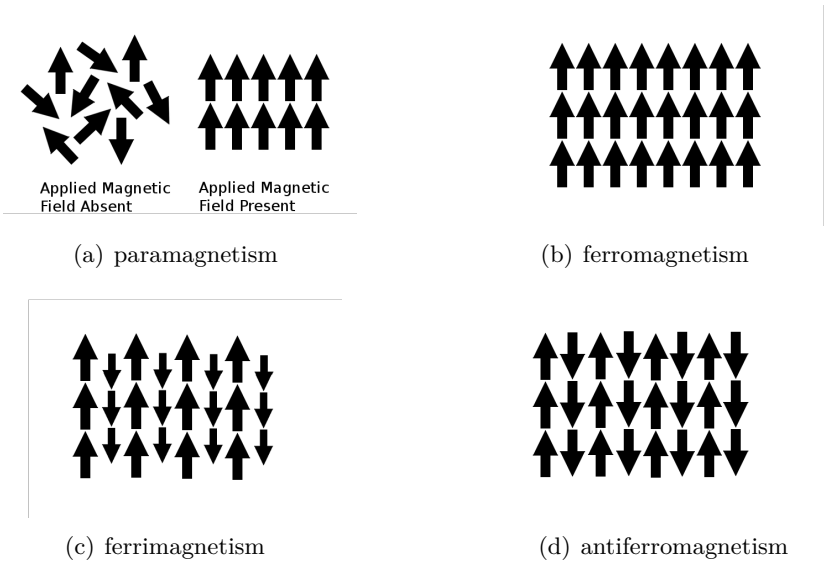

(a) paramagnetism (b) ferromagnetism

(c) ferrimagnetism (d) antiferromagnetism

Figure 3-1: Four different magnetic behaviours in materials [9]

material becomes paramagnetic. In paramagnetic materials (Figure 3-1 (a)) the moments are disordered in the absence of an applied magnetic field and ordered in the presence of an applied magnetic field. This critical temperature is called **Curie temperature** for ferromagnetic and ferromagnetic materials. Table 3-1 shows names of most common ferromagnetic and ferrimagnetic materials and their Curie temperature.

A **permanent magnet** (Figure 3-2) is an object that creates its own persistent magnetic field. This object has, therefore, to be made of a ferromagnetic (or ferrimagnetic) material and has to be immersed in powerful magnetic field during manufacture. This process, called magnetization, aligns all the dipoles moments within the atoms, so that their individual magnetic fields add together to create a measurable macroscopic field.

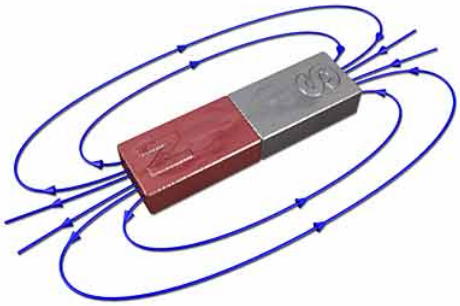

Figure 3-2: permanent magnet [10]

Only a few substances are ferromagnetic like iron, nickel, cobalt and most of their alloys, some compounds of rare earth metals, and a few naturally-occurring minerals such as lodestone.

3-1-2 Electric current

According to the **Ampère's circuital law**, reported below, an electric current creates a magnetic field:

$$\oint_C \mathbf{B} \cdot d\mathbf{l} = \mu_m \int_S \mathbf{J} \cdot d\mathbf{S} \tag{3-1}$$

Therefore any conductive wire current curring can generate a magnetic field.

Four of the metals commonly used in conductor cables production are copper, gold, silver and aluminum. Their melting point are 1084 °C, 1064 °C, 962 °C, and 660 °C respectively. By exploiting the excellent heat exchange properties of liquid metals it should be possible to keep the blade temperature below these value. Conductor wires in copper, gold, silver or aluminum could therefore keep the solid state also inside a turbine blade. These metals have a low electric resistivity. The latter, however, is a linearly increasing function of temperature, as shown in Figure 3-3. The electric power required to make a certain electric current flow into a wire increases linearly with the electric resistance:

$$P = R(T) \cdot I^2 \tag{3-2}$$

Therefore, the electric power required for the generation of a certain magnetic field increases linearly with temperature. Furthermore, this power is dissipated as heat by the wire, so cooling power provided by the metal coolant must augment.

In the electromagnets, to concentrate the magnetic field, the wire is wound into a coil with many turns of wire lying side by side. The magnetic field of all the turns of wire passes through the center of the **coil**, creating a strong magnetic field there.

Much stronger magnetic fields can be produced if a "**core**" of ferromagnetic material, such as soft iron, is placed inside the coil. The ferromagnetic core increases the magnetic field to thousands of times the strength of the field of the coil alone, due to the high **magnetic permeability** (μ) of the ferromagnetic material. This is called a ferromagnetic-core or **iron-core electromagnet**. Figure 3-4 shows the three basic devices to generate magnetic fields by electric currents.

The magnetic field intensity increases as the magnetic permeability of the medium ($\mu_m = \mu_0 \cdot \mu_r$) increases. The relative magnetic permeability (μ_r) depends from the magnetic susceptibility (χ) according to the following relation:

$$\mu_r = 1 + \chi \tag{3-3}$$

The **Curie-Weiss law** describes the magnetic susceptibility χ of a ferromagnetic material as a function of temperature above the Curie point (paramagnetic region):

$$\chi = \frac{C}{T - T_c} \tag{3-4}$$

C is a material-specific Curie constant, T and T_c are respectively the temperature and the Curie temperature measured in kelvin.

Finally, if electric currents are used there is not a thermal limit above which is not possible to have a magnetic field. However as the temperature increases the electric resistivity of the conductor increases. Moreover, if an iron-core electromagnet is used, above the Curie temperature of the core its magnetic permeability decreases as the temperature increases. In any case, being equal the magnetic field intensity, the electric power required increases with the temperature.

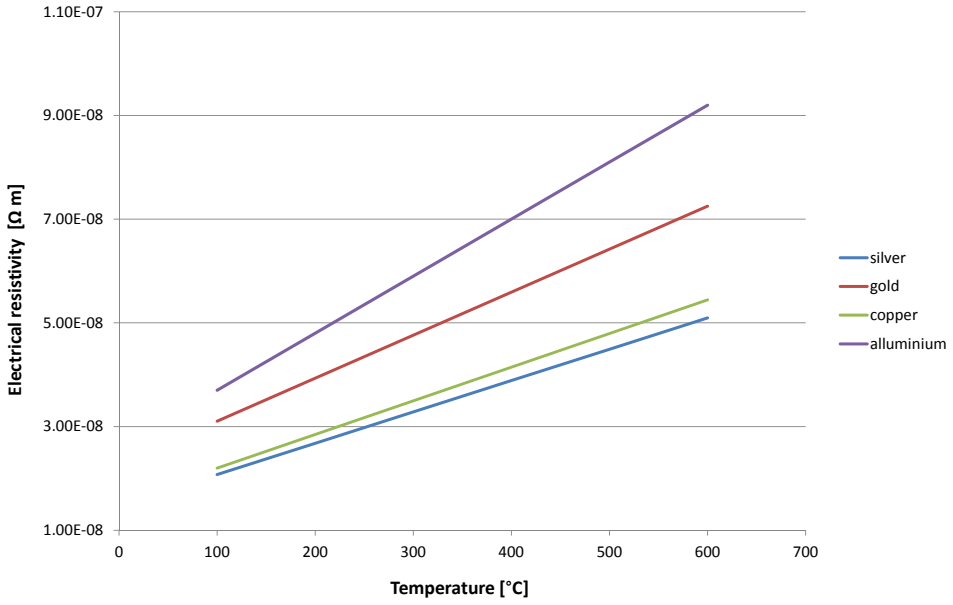

Figure 3-3: Electric resistivity - temperature

3-2 Blade cooling channel model

In the preceding section a brief reminder about the generation of magnetic fields and the influence of temperature on it was given. Is now clear how important is to keep low the blade temperature if a magnetic field into a blade cooling channel has to be generated.

Liquid metals are able to do that, thanks to their excellent heat exchange properties. In order to provide a quantitative evaluation of them, a simple heat exchange model of a cooling channel of a turbine blade was constructed.

Referring to the blade section in Figure 3-5 (a) a channel perfectly fitting the the leading edge was considered. The external and internal diameter of the pipe are respectively 7 mm and 5 mm, therefore the wall thickness is 1 mm. The cord of this blade is around 60 mm; considering a ratio blades highness - cord approximately 1 for the firs stator stage, the highness of the channel was set to 60 mm. The channel is considered to be immersed in an hot-air stream perpendicular to its axis, with coolant flowing inside it. The system is schematically shown in Figure 3-5 (b), where the geometric parameters of the channel are reported. In Figure 3-5 (b) temperature and velocity of air in cross flow are also indicated.

Material	**Curie temperature** [K]
Iron (Fe)	1043
Cobalt (Co)	1400
Nickel (Ni)	631
Gadolinium (Gd)	292
Dysprosium (Dy)	88
MnAs	318
MnBi	630
MnB	578
MnSb	587
CrO_2 (Gd)	386
$CrBr_3$	37
MnAs	318
EuO	69
EuS	16.5
Au_2MnAl	200
Cu_2MnAl	630
Cu_2MnIn	500
Iron (III) oxide (Fe_2O_3)	948
Iron (II, III) oxide ($FeOFe_2O_3$)	858
$NiOFe_2O_3$	858
$CuOFe_2O_3$	728
$MgOFe_2O_3$	713
$MnOFe_2O_3$	573
$Y_3Fe_5O_{12}$	560

Table 3-1: Curie temperature of materials [11] [12]

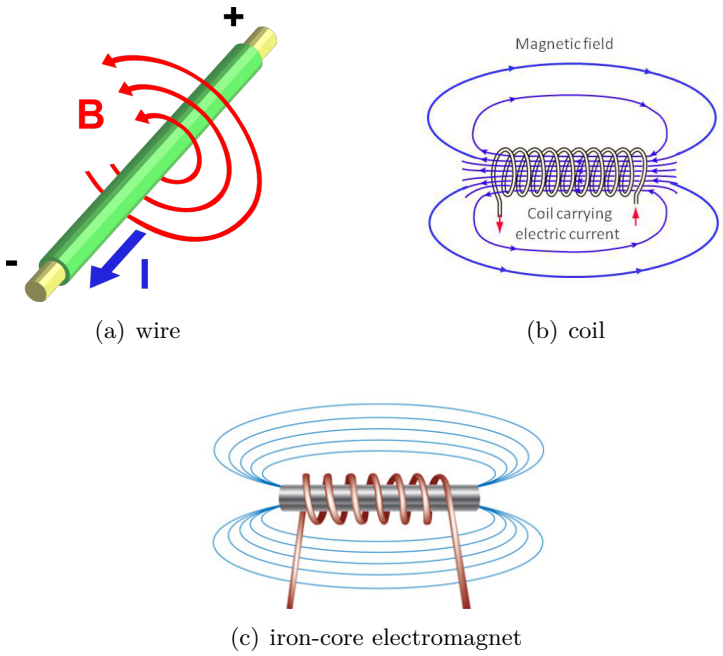

(a) wire (b) coil

(c) iron-core electromagnet

Figure 3-4: Magnetic field generation by electric currents

The thermal power (dq) flowing through an infinitesimal length of the channel (dx) from hot air to coolant can be described using the concept of thermal resistance specific per unit length; a scheme is illustrated in Figure 3-6.

$$dq(x) = \frac{T_{air} - T_{cool}(x)}{R_{conv,ext} + R_{cond} + R_{conv,int}} \cdot dx \quad [W] \tag{3-5}$$

The external and internal thermal resistances are:

$$R_{conv,ext} = \frac{1}{h_{ext} \cdot 2\pi r_{ext}} \quad \left[\frac{m \cdot K}{W}\right] \tag{3-6}$$

$$R_{conv,int} = \frac{1}{h_{int} \cdot 2\pi r_{int}} \quad \left[\frac{m \cdot K}{W}\right] \tag{3-7}$$

The conductive thermal resistance of the cylindrical wall is:

$$R_{cond} = \frac{ln\left(\frac{r_{ext}}{r_{int}}\right)}{2\pi k} \quad \left[\frac{m \cdot K}{W}\right] \tag{3-8}$$

For sake of simplicity k, h_{int} and h_{ext} are considered constant along the channel. k is set equal to 17 $W/m\ K$, that is the value of thermal conductivity of *Inconel 625* at 600 °C [14].

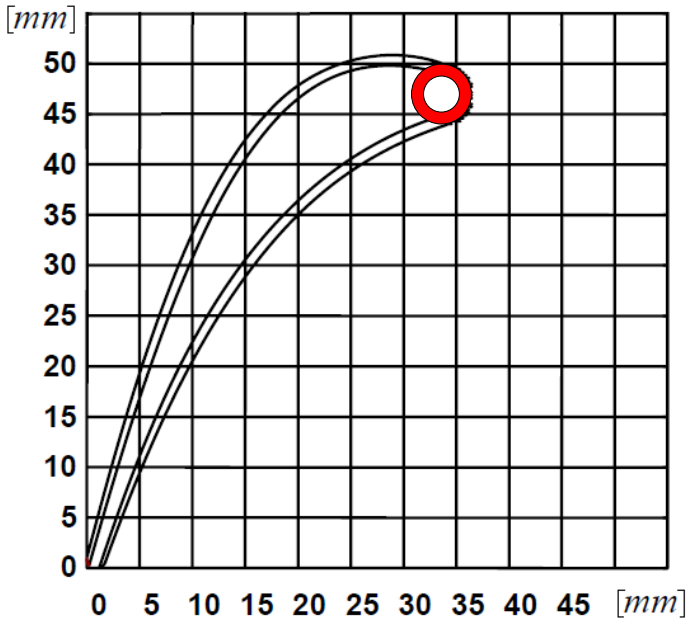

(a)

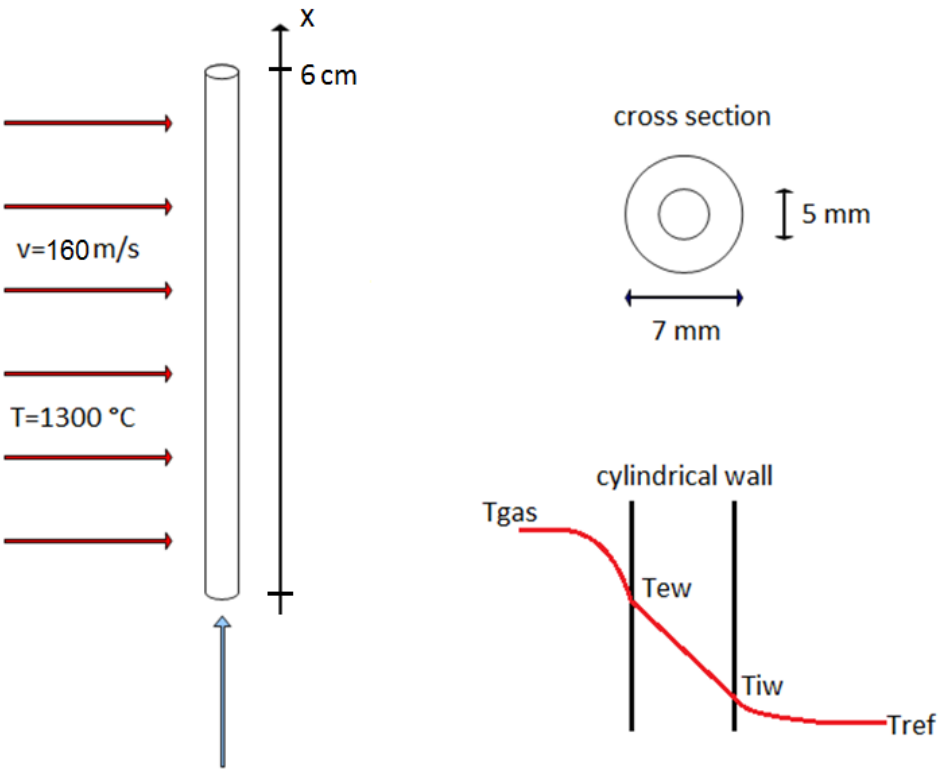

(b)

Figure 3-5: Reference blade section (a) [13] and channel model (b)

Figure 3-6: Heat transfer in an infinitesimal length of the channel

The details of the calculations of average convective heat transfer coefficients are given in Subsection 3-4-1.

The total thermal resistance is:

$$R_{eq} = \frac{1}{h_{ext} \cdot 2\pi r_{ext}} + \frac{ln\left(\frac{r_{ext}}{r_{int}}\right)}{2\pi k} + \frac{1}{h_{int} \cdot 2\pi r_{int}} \tag{3-9}$$

The problem can be simplified from conceptual and mathematical point of view. It can, in fact, be turned in a flow of coolant in a circular duct with constant temperature of internal wall. The external convective resistance and the wall conductive resistance are considered equal to zero and their effect is assigned to the internal convective resistance:

$$R_{eq} = \frac{1}{2\pi r_{int}} \left(\frac{r_{int}}{h_{ext} \cdot r_{ext}} + \frac{ln\left(\frac{r_{ext}}{r_{int}}\right) \cdot r_{int}}{k} + \frac{1}{h_{int}} \right) = \frac{1}{h_{eq} \cdot 2\pi r_{int}} \quad \left[\frac{m \cdot K}{W}\right] \tag{3-10}$$

So it results:

$$h_{eq} = \left(\frac{r_{int}}{h_{ext} \cdot r_{ext}} + \frac{ln\left(\frac{r_{ext}}{r_{int}}\right) \cdot r_{int}}{k} + \frac{1}{h_{int}} \right)^{-1} \quad \left[\frac{W}{m^2 \cdot K}\right] \tag{3-11}$$

Figure 3-7 shows this simplification.

We can therefore simply write:

$$dq(x) = \frac{T_{air} - T_{cool}(x)}{R_{eq}} \cdot dx \quad [W] \tag{3-12}$$

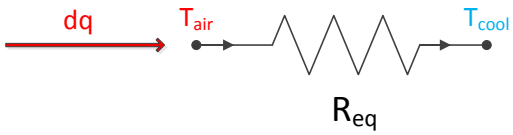

Figure 3-7: Equivalent thermal resistance

The Péclet number of all the considered coolants is enough high to allow to neglect the conduction in the axial direction. Thus the energy balance on an infinitesimal length of the channel (whose scheme is given in Figure 3-8) may be written as follows:

$$dq = \dot{m}_{cool} \cdot c_{p,cool} \cdot dT_{cool} \quad [W] \tag{3-13}$$

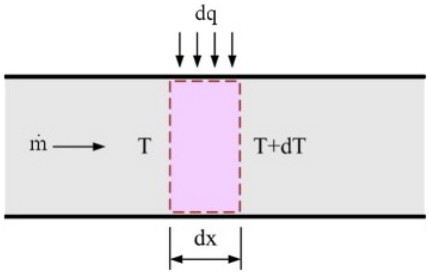

Figure 3-8: Energy balance [15]

By considering an average value of $c_{p,cool}$ constant along the channel and by combining Equations 3-12 and 3-13 the coolant temperature as function of the x coordinate can be obtained:

$$T_{cool}(x) = T_{air} - (T_{air} - T_{cool,in}) \cdot exp\left(-\frac{h_{eq} \cdot 2\pi r_{int}}{\dot{m}_{cool} \cdot c_{p,cool}} \cdot x\right) \tag{3-14}$$

Known $T_{cool}(x)$, $dq(x)$ can be calculated from:

$$dq(x) = \frac{T_{air} - T_{cool}(x)}{R_{eq}} \cdot dx \quad [W] \tag{3-15}$$

By using the model of thermal resistance illustrated in Figure 3-6 also external ($T_{e,w}$) and internal ($T_{i,w}$) wall temperatures can be expressed as functions of x coordinate:

$$dq(x) = \frac{T_{air} - T_{e,w}(x)}{R_{conv,ext}} \cdot dx \quad [W] \qquad \rightarrow \qquad T_{e,w}(x) = T_{air} - R_{conv,ext} \cdot \frac{dq(x)}{dx} \quad [K] \tag{3-16}$$

$$dq(x) = \frac{T_{i,w}(x) - T_{cool}(x)}{R_{conv,int}} \cdot dx \quad [W] \quad \rightarrow$$

$$\rightarrow \qquad T_{i,w}(x) = R_{conv,int} \cdot \frac{dq(x)}{dx} - T_{cool}(x) \quad [K] \tag{3-17}$$

The described model was implemented in *excel*, the channel was discretized in 21 points along its length, so that the discretization step is 3 mm.

Before to carry out calculations with liquid metals as coolants, air was considered in order to have a term of comparison. Conditions of air were used in which it could be when is bled form the compressor to be sent to the blades in a modern gas turbine (pressure=15 bar, temperature=400 °C).

A value of 160 m/s was chosen for the velocity of the air in cross flow on the cylinder. This value is lower than typical relative velocities in a gas turbine, but it was chosen in order to have a Mach number lower than 0.2. Therefore the air flow can be considered incompressible and a simple correlation (see Subsection 3-4-1) can be used to calculate the Nusselt number. A value of 100 m/s was chosen for the bulk velocity of the air coolant at the channel inlet, the corresponding Reynolds number is around 110000. The temperature of external air was set 1300 °C. The obtained temperatures profiles ($T_{coool}(x)$, $T_{e,w}(x)$, $T_{i,w}(x)$) are shown in Figure 3-9.

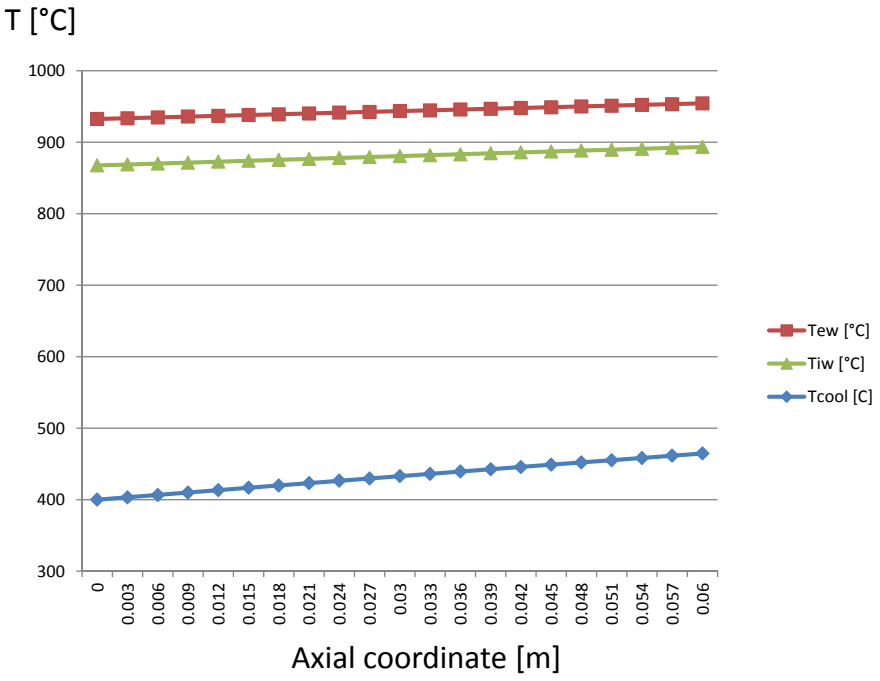

Figure 3-9: Air coolant: temperatures profiles

3-3 Liquid metals properties

To figure out which metals could be good coolants for this application, an analysis of the relevant properties of several metals was carried out. The references used for such analysis

are "Diffusion in liquid metal systems - final report" [16] , "Liquid-metals Handbook" [17] and "Liquid metals: an introduction to the physics and chemistry of metals in the liquid state" [18].

The most relevant physical properties for our application are:

- Melting point;
- Boiling point ;
- Density;
- Viscosity;
- Thermal conductivity;
- Heat capacity;
- Electrical resistivity.
- Magnetic susceptibility.

This properties are temperature dependent. In few cases *Ukanwa* [16] provides directly a function describing this dependence, but for the rest *Ukanwa* [16] and *Lyon* [17] provide for each property different values corresponding to different values of temperature. Since the dependence of properties on temperature is no means negligible, an interpolation of these data was done and relatives analytical functions were found. All those functions are given in appendix A from table A-1 to table A-8. Some graphical representations of those function are given, as examples, as well in Figure A-1(a) and Figure A-1(b). In the appendix A tables A-9 and A-10 show the physical properties of air at 15 bar and the considered liquid metal for different temperature values.

3-4 Liquid metals as coolants

The importance of keeping the blades temperature as lower as possible if a magnetic field has to be generated was discussed in Subsections 3-1-1 and 3-1-2.

Metals with high melting point would not allow low blade temperatures. Therefore, a first selection among metals was simply done on the basis of their melting point. By choosing as threshold value 500 °C, metals with higher melting point as Aluminum, Antimony, Calcium, Gold, Magnesium, Silver are discarded.

Some of the most common metals with melting point lower than 500 °C are Bismuth, Cadmium, Gallium, Lead, Lithium, Mercury, Potassium, Sodium. Their performances as coolants are assessed. For other metals with melting point lower than 500 °C, as Tin or Zinc, were not found enough data.

For all metals, except for lithium, adequate cooling of the channel was not achievable in laminar regime. Thus a turbulent flow was considered, since correlation for the calculation of the Nusselt number in transition regime are not available.

For all metals, except for lithium, the following criteria were applied:

- Péclet number = 510;
- coolant inlet temperature: $T_{cool}(x = 12\ mm) = T_{melting\ point} + 100K$;

The first item is a constrain given by the limit of validity for the used correlations for finding the Nusslet number in the thermal entry region (see Subsection 3-4-1). This correlation is valid only for $x > 2D$, therefore $x > 10\ mm$. For this reason the heat exchange for $x \geq 12\ mm$ was analyzed. Being unknown the heat exchanged between $x = 0$ and $x = 12\ mm$, the temperature in $x = 12\ mm$ was set 100 degrees higher than melting point to be sure that $T_{cool}(x = 0) > T_{melting}$.

Lithium is able to achieve an effective cooling of the channel cylindrical wall also in laminar regime ($Re = 2200$ at the outlet, where it is higher). A correlation to calculate the Nusselt number since the channel inlet was used (see Subsection 3-4-1). Therefore, lithium temperature at the channel inlet was set only 10 degrees higher than its melting point.

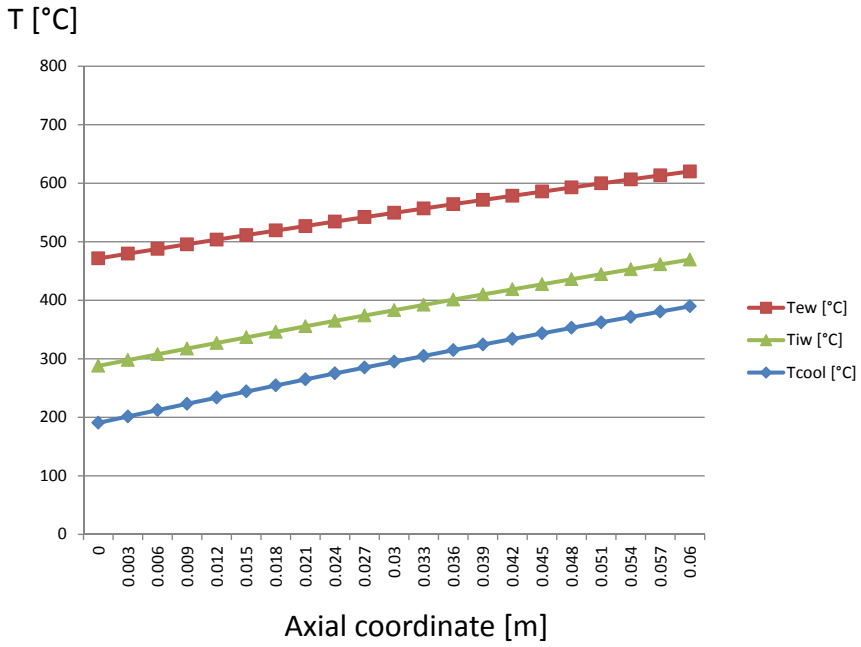

Figure 3-10: Lithium coolant: temperatures profiles

Graphs with temperature profiles along the channel are in Figures from 3-10 to 3-17. Figures Figure 3-18 (a) and (b) show respectively the internal and the external wall temperature at the channel outlet.

Lithium shows the higher potential as coolant from a thermodynamic point of view, especially because of its high value of heat capacity (around 4.19 $kJ/kg\ K$). Even in laminar regime lithium keeps the maximum channel temperature close to 600 °C.

Since in the proposed innovative cooling system the metal flows in presence of a magnetic field, its heat exchange performances are influenced both by the thermodynamic properties and the electro-magnetic ones. The latter, in particular, are electrical resistivity and magnetic permeability. Their importance is widely discussed in Chapters 4 and 6. At this stage it is anticipated that the effect of applied magnetic field on the fluid motion and heat exchange enhancement grows as the magnetic permeability of the fluid increases and its electrical

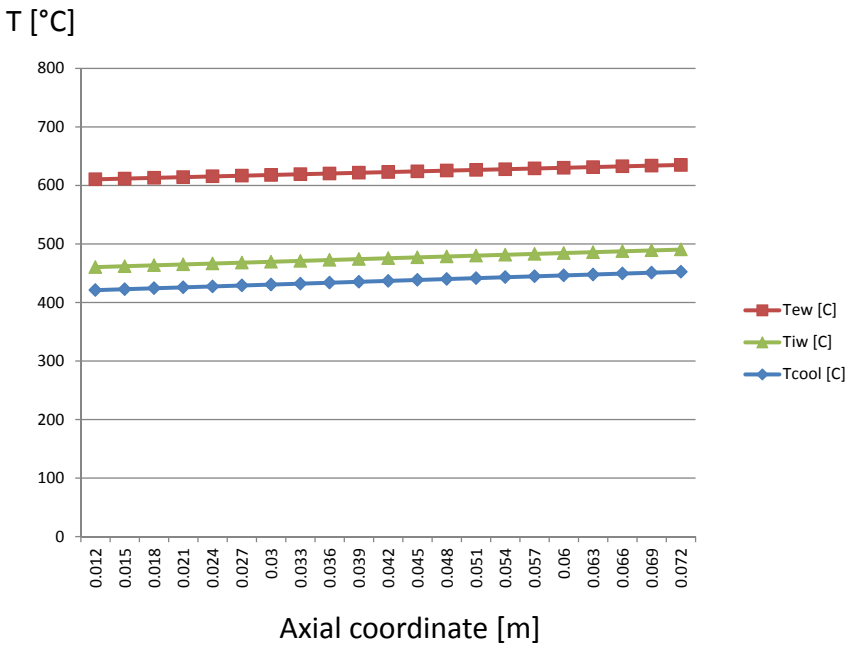

Figure 3-11: Cadmium coolant: temperatures profiles

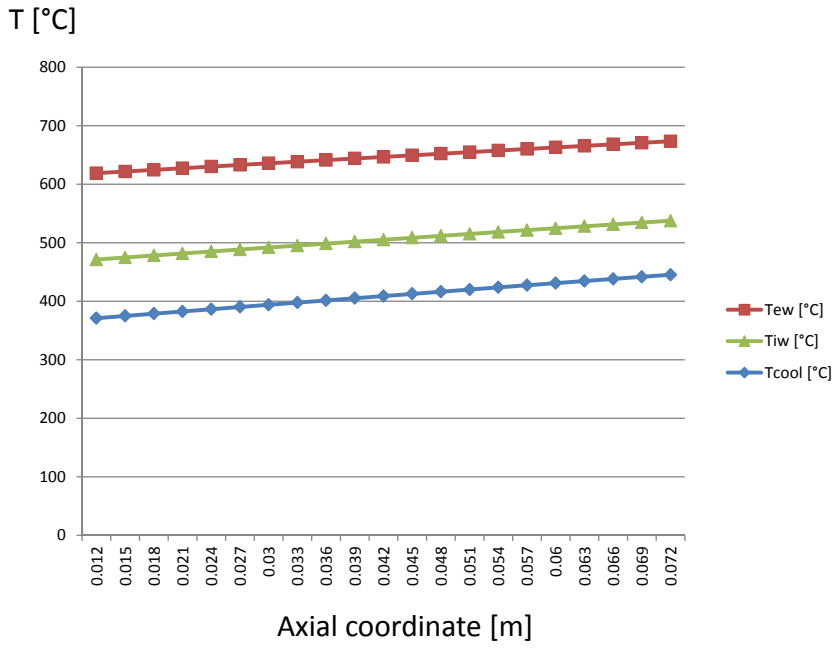

Figure 3-12: Bismuth coolant: temperatures profiles

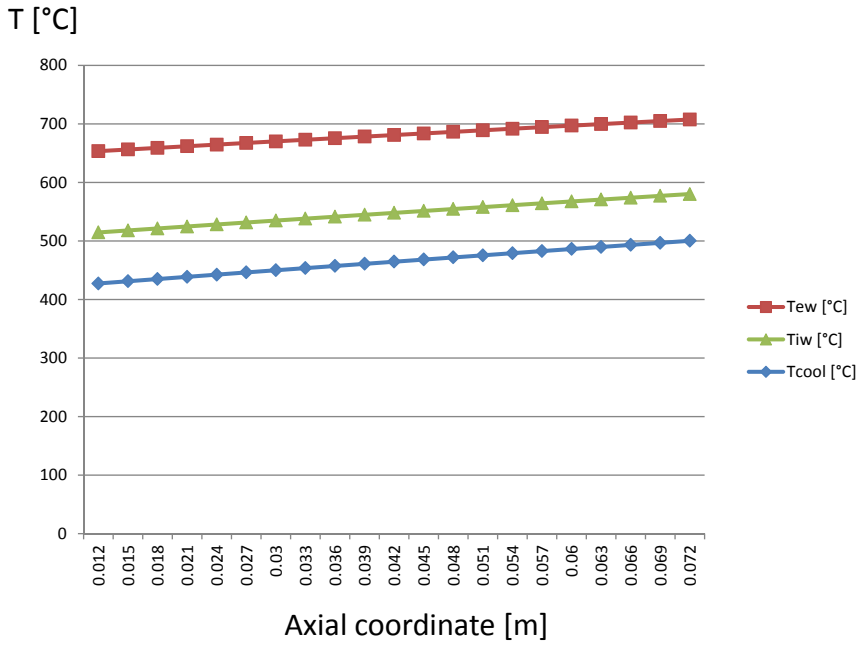

Figure 3-13: Lead coolant: temperatures profiles

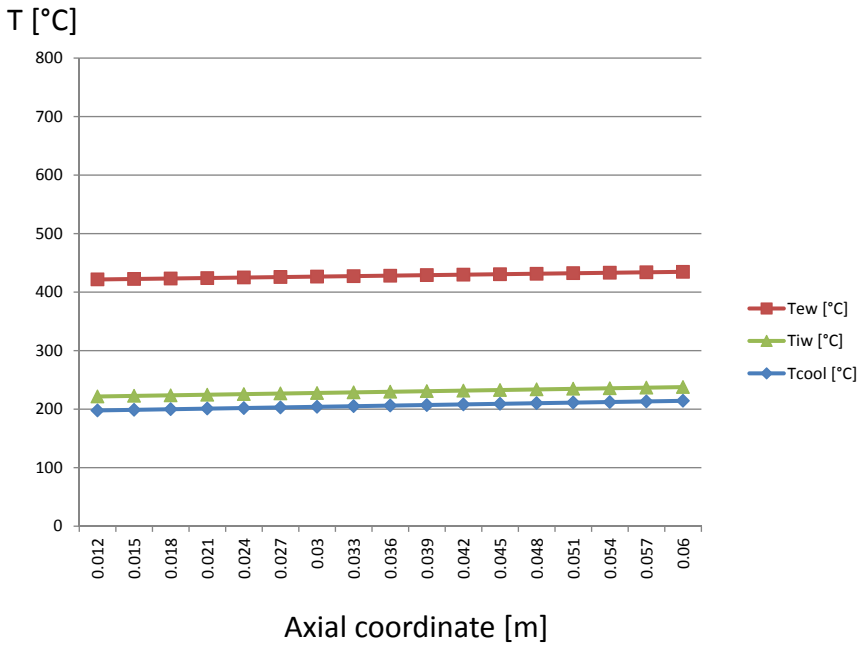

Figure 3-14: Sodium coolant: temperatures profiles

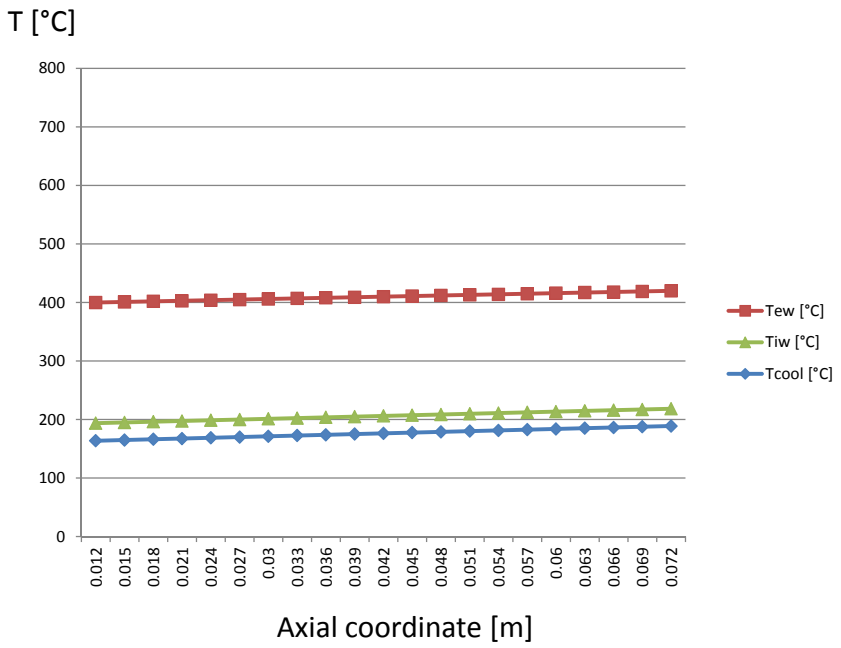

Figure 3-15: Potassium coolant: temperatures profiles

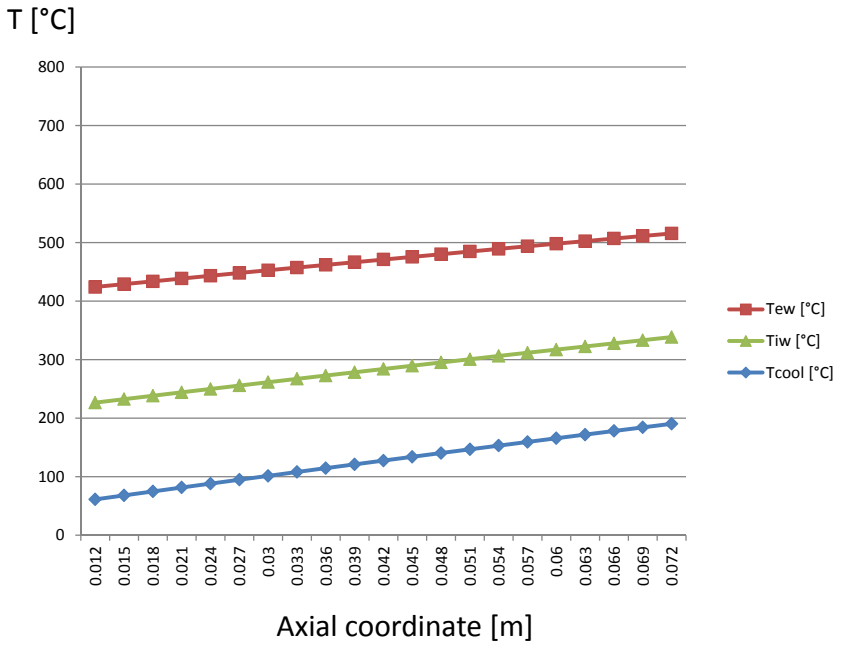

Figure 3-16: Mercury coolant: temperatures profiles

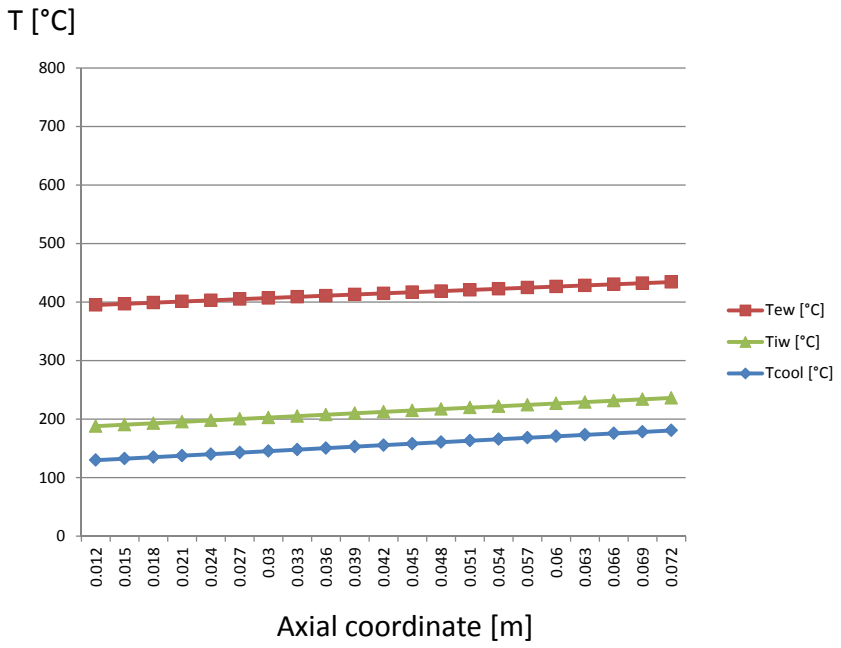

Figure 3-17: Gallium coolant: temperatures profiles

resistivity decreases. The electrical resistivity values are quite different between a metal and another. As shown in appendix A in table tables A-9 and A-10, among the analyzed metals Sodium has the lowest electric resistivity and Bismuth has the highest. *Shimoji* [18] provides magnetic susceptibility (χ) measurements for some metals at the melting point. The values of magnetic susceptibility for the considered metals is around $\pm 10^{-5} \div 10^{-6}$. The relative magnetic permeability (μ_r) comes therefore out to be a not relevant parameter in the choice of the most suitable metals for this application because it varies very little between a metal and an other:

$$\chi = \mu_r - 1 \quad \rightarrow \quad \mu_r = 1 + \chi \simeq 1 \pm 10^{-5} \div 10^{-6} \ \frac{H}{m} \tag{3-18}$$

Unfortunately metals with very high magnetic permeability as iron, nickel and cobalt have very high melting point, around 1500 °C.

It is worth now to anticipate another conceptual element that will be widely discussed in the next Chapters: the higher the velocity of the liquid metal flow, the higher the effect of the magnetic field on it and the consequent heat exchange enhancement. Figure 3-19 shows the value of the Reynolds number and of the velocity for each metal. Cadmium, potassium and sodium have much higher velocities than other metals.

The temperature difference between internal and external wall (ΔT_{wall}) is an important parameter because it is the cause of thermal stresses inside the wall due to different thermal dilatations. The maximum ΔT_{wall} along the tube occurs at the channel inlet, where the temperature difference between external air and coolant is the highest. Figure 3-18 (c) shows

the value of this maximum ΔT_{wall} for air and metals. For metals it is quite bigger with respect to air because of the much higher internal heat transfer coefficient. For air it is about 2500 W/m^2K, among the metals mercury has the lowest value of heat exchange coefficient which is about 21000 W/m^2K. Bismuth, lead and cadmium have the lowest value of temperature difference between external and internal wall. This value is anyway around 150 K, which is approximately 2.4 times the value with air.

3-4-1 Convection Correlations

The detail of the calculations of the internal and external convective coefficient in the used model are provided here.

The thermophysical properties of the fluid from which the heat exchange depends are:

- Thermal conductivity: $k \quad \left[\frac{W}{m\ K}\right]$
- Specific heat capacity: $c_p \quad \left[\frac{J}{kg\ K}\right]$
- Density: $\rho \quad \left[\frac{kg}{m^3}\right]$
- Dynamic viscosity: $\mu \quad [Pa\ s]$

From these properties two important parameters characterising the fluid are defined:

- Thermal diffusivity: $\alpha = \frac{k}{\rho\ c_p} \quad \left[\frac{m^2}{s}\right]$
- Kinematic diffusivity: $\nu = \frac{\mu}{\rho} \quad \left[\frac{m^2}{s}\right]$

The dimensionless groups describing a general convection phenomenon are:

- Reynolds number: $Re_D = \frac{u\ D}{\nu} = \frac{u\ D\ \rho}{\mu} \quad [-]$
- Prandtl number: $Pr = \frac{c_p\ \mu}{k} = \frac{\nu}{\alpha} \quad [-]$
- Péclet number: $Pe = Re_D\ Pr = \frac{u \cdot D}{\alpha} \quad [-]$
- Nusselt number: $Nu_D = \frac{h\ D}{k} \quad [-]$

In literature several correlations that give the value for the Nusselt number as a function of Reynolds and Prandtl numbers are available for different cases. Once the Nusselt number is known, from its definition the heat transfer coefficient (h) is easily findable.

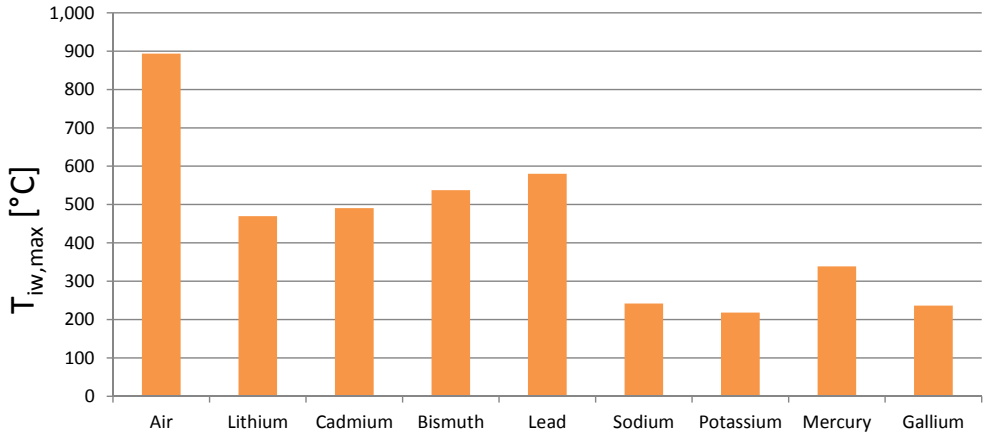

(a) Internal wall temperature at channel outlet

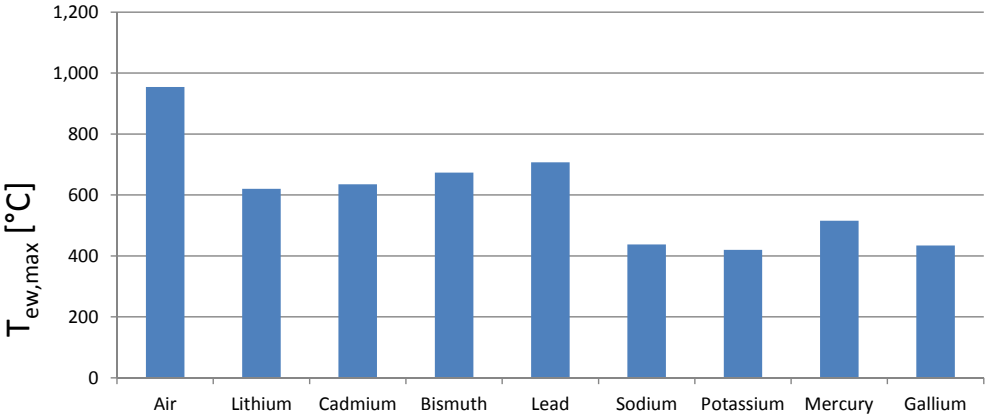

(b) External wall temperature at channel outlet

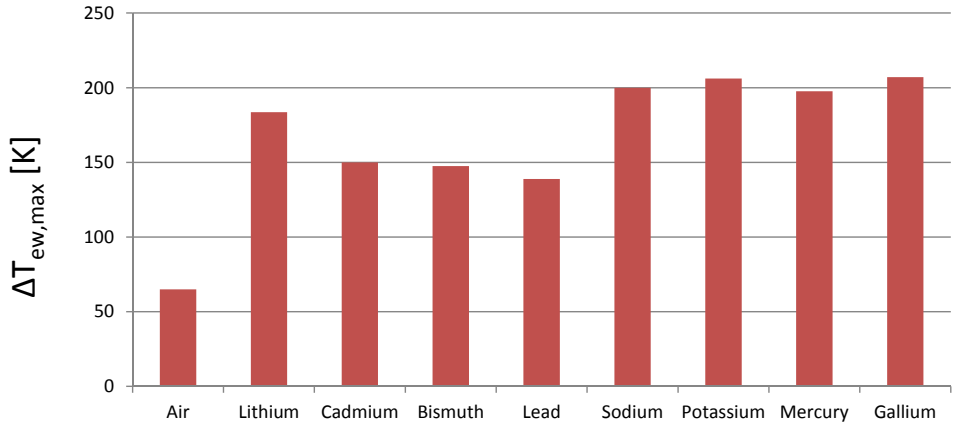

(c) Maximum temperature difference between external and internal wall

Figure 3-18: Wall temperatures

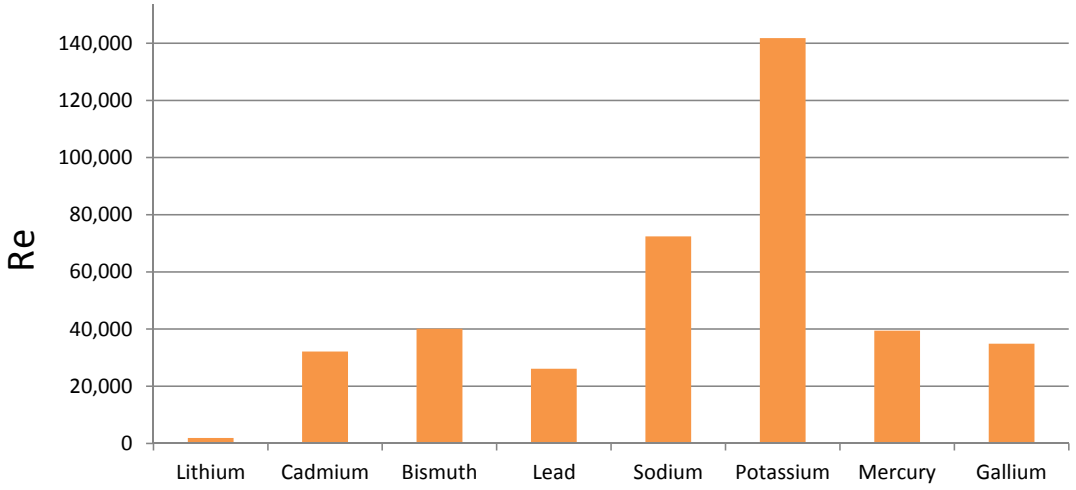

(a) Reynolds number

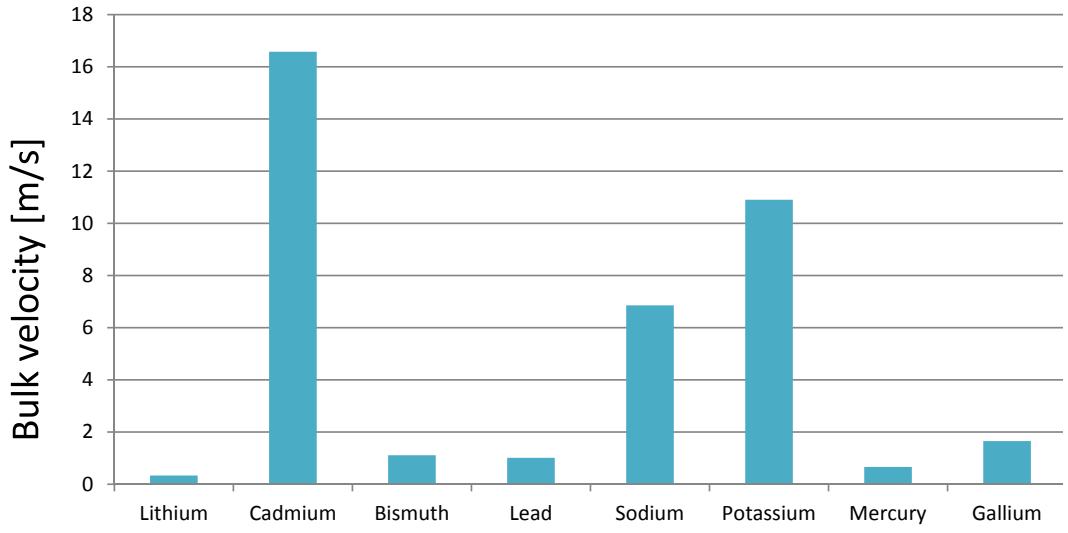

(b) Bulk velocity

Figure 3-19: Reynolds number and bulk velocity

Cylinder in cross flow D appearing in the above listed parameters is the external diameter of the pipe, u is the velocity of the upstream undisturbed flow.

The external average heat transfer coefficient was calculated by means of the empirical correlation due to Hileprt [19] :

$Nu_D = 0.027 \cdot Re^{0.805} \cdot Pr^{1/3}$

Ranges of validity for this correlation are:

- $40000 \lesssim Re_D \lesssim 400000$
- $Pr \gtrsim 0.7$

In our model $Re_D \simeq 77000$ and $Pr \simeq 0.76$

The speed of sound in air flowing at 160 m/s and 1300 °C is 770 m/s, therefore the Mach number is 0.2 and the flow can be considered incompressible, as required for the application of Hileprt correlation.

The thermophysical properties were evaluated at the average film temperature along the channel.

Internal convection with air in a circular duct D appearing in the above listed parameters is the internal diameter of the pipe, u is the bulk velocity of the coolant inside the channel.

For a turbulent flow the thermal entrance length is between 10 D and 60 D [19]. In this case $L = 12\ D$, therefore a thermally developing flow was considered. The mean Nusselt number ($N_{m,D}$) was calculated using Arabi's correlation [20]:

$$\frac{N_{m,D}}{Nu_{f.d.,D}} = 1 + \frac{C}{x/D} \tag{3-19}$$

$$C = \frac{(x/D)^{0.1}}{Pr^{1/6}} \left(0.68 + \frac{3000}{Re^{0.81}} \right) \tag{3-20}$$

Dittus-Boelter's correlation [19] was used to evaluate the Nusselt number of the thermally fully developed flow ($Nu_{f.d.,D}$):

$$Nu_{f.d.,D} = 0.023 \cdot Re_D^{4/5} \cdot Pr^{0.4} \tag{3-21}$$

Ranges of validity for this correlation are:

- $Re_D \gtrsim 10000$
- $0.6 \lesssim Pr \lesssim 160$

In our model when air is the coolant $Re_D \simeq 112000$, $Pr \simeq 0.72$.

The speed of sound in air flowing at 100 m/s and 400 °C is 517 m/s, therefore the Mach number is 0.19 and the flow can be considered incompressible, as required for the application of Dittus-Boelter's correlation.

The thermophysical properties are evaluated at the average of the coolant air temperature along the channel.

Internal convection with liquid metals in turbulent flow in a circular duct D appearing in the above listed parameters is the internal diameter of the pipe, u is the bulk velocity of the coolant inside the channel.

The thermal entrance length (TEL) for liquid metals in turbulent flow has been found by Genin [20]:

$$TEL = \frac{0.04\ Pe}{1 + 0.002\ Pe}\ D \tag{3-22}$$

In the thermal entry region the Local Nusselt number was found as proposed by Chen and Chiou [20]:

$$Nu(x) = \left[1 + \frac{2.4}{x/D} - \frac{1}{(x/D)^2}\right] \cdot (4.5 + 0.0156 \cdot Re_D^{0.85} \cdot Pr^{0.86}) \tag{3-23}$$

Ranges of validity for this correlation are:

- $x > 2D$
- $Pe > 500$

The first part of the channel (x < 2D) was not considered. For all the metals the Péclet number was imposed to be equal to 510 at the channel inlet, where it has lowest value.

Notter and Sleicher's correlation [20] was used to evaluate the internal heat transfer coefficient for liquid metals in fully developed turbulent flow:

$Nu_D = 4.8 + 0.0156 \cdot Re_D^{0.85} \cdot Pr^{0.93}$

Ranges of validity for this correlation are:

- $10^4 \lesssim Re_D \lesssim 10^6$
- $0.003 \lesssim Pr \lesssim 0.1$

These conditions are satisfied by all the metals.

In each of the points in which the channel is discretized the thermophysical properties are evaluated at the local coolant temperature. A local Nusselt number and then a local heat transfer coefficient are so calculated. The average of the heat transfer coefficients is used to calculate the average internal convective resistance.

Internal convection with in laminar flow in a circular duct The highest Reynolds number along the channel is at the outlet because the viscosity is the lowest, being maximum the coolant temperature. For lithium the Reynolds number at the channel outlet was set to 2200, lower than critical value (about 2300).

The thermal entrance length (TEL) was found as:

$$TEL = 0.0335 \cdot Pe \cdot D = 13\ mm \tag{3-24}$$

Shah [21] developed the following set of equations that gives the Nusselt number trend as function of spatial coordinate in streamwise direction:

$$\begin{cases} Nu_D(x^*) = 1.077 \cdot x^{*-1/3} - 0.7 & for \quad x^* \leq 0.01 \\ Nu_D(x^*) = 3.657 + 6.874 \cdot (10^3 x^{*-1/3})^{-0.488} \cdot e^{-75.2\ x^*} & for \quad x^* > 0.01 \end{cases} \tag{3-25}$$

Equations 3-24 and 3-25 are valid for $Pe > 50$; in this case lithium has $Pe \simeq 77$.

The value of Nusselt number was simply set equal to 3.66 in the fully developed region. This is the value for a fully developed laminar flow with Pe>5.

In each of the points in which the channel is discretized the thermophysical properties are evaluated at the local coolant temperature. A local Nusselt number and then a local heat transfer coefficient are so calculated. The average of the heat transfer coefficients is used to calculate the average internal convective resistance.

Chapter 4

Fundamentals of Magnetohydrodynamics

Magnetohydrodynamics (MHD) is the branch of physics dealing with interactions of electrically conducting fluid flows and magnetic fields [6].

The exact form of this interaction is analyzed in details in the following subsections. However, in order to have a brief understanding of the physical phenomenon, it is possible to split conceptually the process into three parts:

i) The relative movement of a conducting fluid and a magnetic field ($\mathbf{B}$) causes an Electromotive force (emf) according to **Faraday's law of induction** (Equation 4-1).

$$emf = -\frac{d}{dt}\int_S \mathbf{B} \cdot dS \tag{4-1}$$

Consequently, an induced current density distribution is generated inside the fluid.

ii) According to **Ampere's law** (Equation 4-2), this induced current density ($\mathbf{J}$) gives rise to a second, induced, magnetic field which adds to the imposed magnetic field ($\mathbf{B_{ind}}$).

$$\oint_C \mathbf{B_{ind}} \cdot d\mathbf{l} = \mu_m \int_S \mathbf{J} \cdot d\mathbf{S} \tag{4-2}$$

This induced magnetic field is generally directed so as to inhibit the imposed magnetic field ($\mathbf{B_{imp}}$).

iii) The resulting magnetic field interacts with the induced current density and produces a **Lorentz Force**, according to Equation 4-3.

$$\mathbf{f} = \mathbf{J} \times \mathbf{B} \tag{4-3}$$

This force is generally directed so as to inhibit the fluid motion.

This effect of mutual inhibition of the flow and the magnetic field is the hallmark of MHD [6]. However, under particular conditions, which we are interested in and which will be analyzed afterwards, the magnetic field only acts on the fluid flow inhibiting it. Conversely, the induced magnetic field can be neglected by comparison with imposed magnetic field that remains so unchanged.

4-1 The governing equations of electrodynamics

4-1-1 Charge conservation

The conservation of charge (Equation 4-4) states that the rate of change in time (t) of the charge density (ρ_e) in a point must equal the divergence of the current density ($\mathbf{J}$).

$$\frac{\partial \rho_e}{\partial t} = -\nabla \cdot \mathbf{J} \tag{4-4}$$

In other words the rate at which charge is decreasing inside a small volume must equal the rate at which charge flows out across the surface of that volume: ρ_e is always zero in the interior of a stationary conductors, because the electrostatic repulsion forces keeps the free charges on the surface. It can be demonstrated ([6]) that when there is motion, a finite charge density in the interior of a conductor can be sustained.

In conductors travelling at much lower speed than light, which we are interested in, ρ_e is so small that its change with time can be reasonably neglected [6], thus, eq. 4-4 simplifies to:

$$\nabla \cdot \mathbf{J} = 0 \tag{4-5}$$

4-1-2 Ampére's law

Ampére's circuital law (Equation 4-6) states that a given current distribution ($\mathbf{J}$) produces a magnetic field ($\mathbf{B_{ind}}$) such that the integral of $\mathbf{B_{ind}}$ over a closed loop C is proportional to the integral on the surface S (enclosed by C) of current density, i.e. to the total current passing through a surface S ($\mathbf{I}_{enc}$):

$$\oint_C \mathbf{B_{ind}} \cdot d\mathbf{l} = \mu \int_S \mathbf{J} \cdot d\mathbf{S} = \mu \mathbf{I}_{enc} \tag{4-6}$$

The local form of the equation, derived using Stoke's theorem, is:

$$\nabla \times \mathbf{B_{ind}} = \mu \mathbf{J} \tag{4-7}$$

Originally, Maxwell introduced another term to this equation called *displacement current*. The equation is therefore named **Ampére-Maxwell equation** and is expressed as:

$$\nabla \times \mathbf{B_{ind}} = \mu \left[\mathbf{J} + \varepsilon_0 \frac{\partial \mathbf{E}}{\partial t} \right] \tag{4-8}$$

However, for MHD purposes, this correction is not needed. Indeed, like the case of ρ_e in the charge conservation equation, the term $\varepsilon_0 \, \partial\mathbf{E}/\partial t$ is also very small for practical cases and such that $\varepsilon_0 \, \partial\mathbf{E}/\partial t \ll \mathbf{J}$. Thus, the pre-Maxwell's form of the Ampére Law (Eq. (4-7)) will be used.

It is important to notice that, by taking the divergence of Eq. (4-7), the charge conservation equation, Eq. (4-5), is also satisfied.

4-1-3 Faraday's Law of induction

The integral form of Faraday's Law (Equation 4-9) states that a magnetic field ($\mathbf{B}$) whose flux through a surface S changes over time (t) induces an emf around the closed loop that encloses that surface equal to the total rate of $\mathbf{B}$ flux change through the surface:

$$emf = \oint_C \mathbf{E_i} \cdot \mathrm{d}\mathbf{l} = -\frac{\mathrm{d}}{\mathrm{d}t} \int_S \mathbf{B} \cdot \mathrm{d}\mathbf{S} \tag{4-9}$$

$\mathbf{E_i}$ represents the induced electrostatic field. The flux can change due to a time-varying magnetic field or to the relative movement of the loop respect with the magnetic field, or because the loop is changing its shape.

Suppose that the loop is rigid and at rest, then the e.m.f. can only arise from a magnetic field which is time-dependent. For any and all fixed surfaces, by equating the integrands in the surface integrals, the differential form of Faraday's law is obtained:

$$\nabla \times \mathbf{E_i} = -\frac{\partial \mathbf{B}}{\partial t} \tag{4-10}$$

Therefore, the differential form of Faraday's Law is a special case of integral form. It is also a weaker statement because it only tells us about the electric field induced by a time-varying magnetic field.

Since $\mathbf{B}$ is solenoidal ($\nabla \cdot \mathbf{B} = 0$) the vector potential $\mathbf{A}$ can be defined by:

$$\mathbf{B} = \nabla \times \mathbf{A} \qquad\qquad \nabla \cdot \mathbf{A} = 0 \tag{4-11}$$

If we substitute $\mathbf{B}$ with $\nabla \times \mathbf{A}$ in Faraday's equation we obtain:

$\nabla \times \mathbf{E_i} = -\nabla \times \dfrac{\partial \mathbf{A}}{\partial t}$ from which:

$$\mathbf{E_i} = -\frac{\partial \mathbf{A}}{\partial t} \tag{4-12}$$

4-1-4 Ohm's Law

The conventional form of **Ohm's Law** (Equation 4-13) tells us that the current density ($\mathbf{J}$) in a stationary conductor is proportional to the electrostatic field ($\mathbf{E}$).

$$\mathbf{J} = \sigma \mathbf{E} \tag{4-13}$$

where σ is the electric conductivity of the fluid. If the conductor is moving in a magnetic field the Ohm's Law takes the following general form:

$$\mathbf{J} = \sigma(\mathbf{E_s} + \mathbf{E_i} + \mathbf{u} \times \mathbf{B}) \tag{4-14}$$

The term ($\mathbf{u} \times \mathbf{B}$) is a component of the electrostatic field generated by the interaction between the moving free charges and the external magnetic field.

While in a stationary conductors any charge moves out to the periphery as a result of mutual repulsion, if the conductor is moving the interaction between the moving free charges and the external magnetic field yields a charge distribution in the medium from which arises the electrostatic field component $\mathbf{E_s}$.

The field $\mathbf{u} \times \mathbf{B}$ produces, therefore, two components of $\mathbf{E}$, one direct and one indirect, as schematically shown in Figure 4-1.

Being generated by a charge distribution, according to the Coulomb's, $\mathbf{E_s}$ is irrotational, so it is possible to define the electrostatic potential (V) such that:

$$\mathbf{E_s} = -\nabla V \tag{4-15}$$

The Gauss' law sets the divergence of $\mathbf{E_s}$:

$$\nabla \cdot \mathbf{E_s} = -\nabla^2 V = \rho_e / \epsilon_0 \tag{4-16}$$

which simply tells us that the charge distribution in the fluid generates an electrostatic potential field in all the space.

If the magnetic field changes over time another component of the electrostatic field is generated ($\mathbf{E_i}$). This component comes from the Faraday's law of induction, which can be included in the ohm's law in the form of eq. 4-12 :

$$\mathbf{E_i} = -\frac{\partial \mathbf{A}}{\partial t} \tag{4-17}$$

From now on, Ohm's law will be used in the form:

$$\mathbf{J} = \sigma(-\nabla V - \frac{\partial \mathbf{A}}{\partial t} + \mathbf{u} \times \mathbf{B}) \tag{4-18}$$

By taking the divergence of eq. (4-18) we obtain:

$$\nabla \cdot \mathbf{J} = \sigma \cdot \nabla \cdot (-\nabla V - \frac{\partial \mathbf{A}}{\partial t} + \mathbf{u} \times \mathbf{B})$$

From equations 4-5 and 4-11 it results:

$$\nabla \cdot \mathbf{J} = 0 \qquad and \qquad \nabla \cdot \left(\frac{\partial \mathbf{A}}{\partial t} \right) = \frac{\partial}{\partial t}(\nabla \cdot \mathbf{A}) = \frac{\partial}{\partial t}(0) = 0$$

The equation from which it is possible to calculate the electrostatic potential V is therefore the following:

$$\nabla^2 V = \nabla \cdot (\mathbf{u} \times \mathbf{B}) \tag{4-19}$$

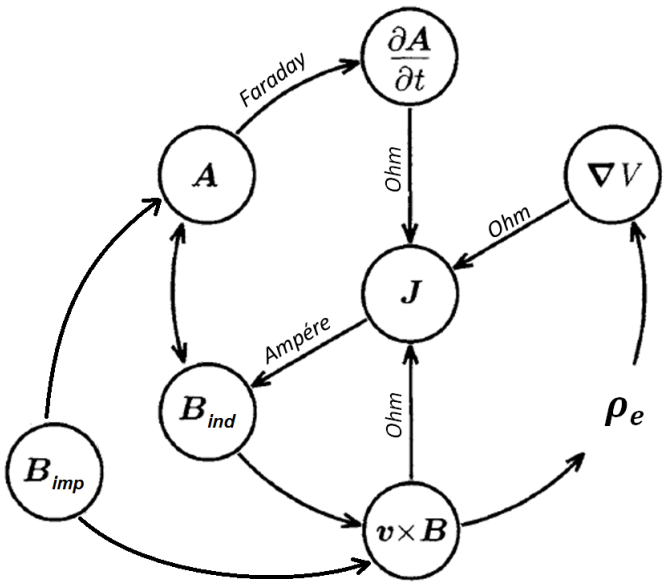

Figure 4-1: Ohm's Law schematic chart

4-1-5 The volumetric Lorentz Force

The total Lorentz force acting on a particle carrying a charge q and moving with velocity $\mathbf{u}$ in a magnetic field $\mathbf{B}$ and in an electrostatic field $\mathbf{E}$ is:

$$\mathbf{f_c} = q\mathbf{E} + q\mathbf{u} \times \mathbf{B} = q(\mathbf{E} + \mathbf{u} \times \mathbf{B}) \tag{4-20}$$

Since in MHD we are concerned with the force acting on the bulk of the fluid, we should sum up all the forces experienced by the charges to obtain the *Volumetric Lorentz Force* (force per unit volume) produced on the fluid:

$$\mathbf{f} = \rho_e \mathbf{E} + \mathbf{J} \times \mathbf{B} \tag{4-21}$$

In conductors traveling at speed much lower than light, which we are interested in, ρ_e is too low to produce any significant electric force, so the first term in eq. 4-21 is negligible and it reduces to:

$$\mathbf{f} = \mathbf{J} \times \mathbf{B} \tag{4-22}$$

4-2 The governing equations of MHD

4-2-1 The governing equations of fluid mechanics

Each phenomenon involving momentum, heat and mass transfer in a fluid is described by a set of equations based on basic laws of conservation of the physical quantities. For a **newtonian fluid** mass conservation (continuity), momentum and energy conservation equations in the local form are, respectively:

$$\begin{cases} \dfrac{\partial \rho}{\partial t} + \nabla \cdot (\rho \mathbf{u}) = 0 \\ \dfrac{\partial (\rho \mathbf{u})}{\partial t} + (\rho \mathbf{u} \cdot \nabla)\mathbf{u} = -\nabla p + \mu \nabla^2 \mathbf{u} + (\lambda + \mu)\nabla(\nabla \cdot \mathbf{u}) + \mathbf{f} \\ \dfrac{\partial}{\partial t}(\rho u_i) + (\rho \mathbf{u} \cdot \nabla) u_i = -p(\nabla \cdot \mathbf{u}) - \nabla \cdot \mathbf{q} + \xi \end{cases} \tag{4-23}$$

The species conservation equation is not mentioned since the fluid taken into consideration is pure and its chemical structure does not change. $\lambda, \mu, \mathbf{f}$ are the volumetric viscosity, the dynamic viscosity and the body forces term. u_i is the internal energy of the fluid, $\mathbf{q}$ is the heat flux vector and ξ is the energy source term [22].

In case of an horizontal flow in forced convection, like the one studied in Chapter 6, the effect of the gravitational force can be neglected by comparison with the other terms in the set of Eq. (4-23). If, in addition, for an incompressible fluid with thermophysical properties independent on temperature, continuity and momentum equations can be solved separately from energy equation and reduce to:

$$\begin{cases} \nabla \cdot \mathbf{u} = 0 \\ \dfrac{\partial \mathbf{u}}{\partial t} + (\mathbf{u} \cdot \nabla)\mathbf{u} = -\dfrac{\nabla p}{\rho} + \nu \nabla^2 \mathbf{u} + \dfrac{\mathbf{f}}{\rho} \end{cases} \tag{4-24}$$

$\nu = \mu/\rho$ is the kinematic viscosity or momentum diffusivity.

Once the velocity field is known, the energy equation can be solved separately. The internal energy equation of set 4-23 is modified by introducing Fourier's law of heat conduction

$$\mathbf{q} = -k \nabla T \tag{4-25}$$

Internal energy, u_i, is then expressed as a function of temperature

$$u_i = c_v T \tag{4-26}$$

where c_v is the specific heat at constant volume.

By introducing Eq. (4-25), Eq. (4-26) and in absence of energy source terms, the energy equation in 4-23 is recast as

$$\frac{\partial T}{\partial t} + (\mathbf{u} \cdot \nabla) T = \frac{k}{\rho c_v} \nabla^2 T \tag{4-27}$$

Note that the term $-p(\nabla \cdot \mathbf{u})$ is eliminated from Eq. (4-23) due to incompressibility.

4-2-2 The complete set of MHD equations

Incorporating the Lorentz Force into the Navier-Stokes equations

The conventional set of Navier-Stokes equations for an incompressible fluid in MHD is modified by introducing the external source term given by the Lorentz force. To calculate the Lorentz force term is necessary to solve the equations of electrodynamics introduced in the first section of this chapter.

The complete set of MHD equations is therefore:

$$\begin{cases} \nabla \cdot \mathbf{u} = 0 \\ \dfrac{\partial \mathbf{u}}{\partial t} + (\mathbf{u} \cdot \nabla)\mathbf{u} = -\dfrac{\nabla p}{\rho} + \nu \nabla^2 \mathbf{u} + \dfrac{\mathbf{J} \times \mathbf{B}}{\rho} \\ \dfrac{\partial T}{\partial t} + (\mathbf{u} \cdot \nabla)T = \dfrac{k}{\rho c_p} \nabla^2 T \\ \mathbf{J} = \sigma(-\nabla V - \dfrac{\partial \mathbf{A}}{\partial t} + \mathbf{u} \times \mathbf{B}) \\ \mathbf{B} = \nabla \times \mathbf{A} \\ \nabla^2 V = \nabla \cdot (\mathbf{u} \times \mathbf{B}) \\ \nabla \times \mathbf{B_{ind}} = \mu_m \mathbf{J} \\ \mathbf{B} = \mathbf{B_{imp}} + \mathbf{B_{ind}} \\ \nabla \cdot \mathbf{B} = 0 \end{cases} \tag{4-28}$$

The non-dimensional form of MHD equations and the dimensionless groups

The non-dimensional form of the previous set can be really useful in some cases and allows to identify some dimensionless parameters that characterize the flow and its interactions with the magnetic field. After introducing some characteristic quantities as reference, in particular length (L_0), velocity (u_0) and magnetic field (B_0), the non-dimensional set of equations becomes

$$\begin{cases} \nabla \cdot \mathbf{u}^* = 0 \\ \dfrac{\partial \mathbf{u}^*}{\partial t^*} + (\mathbf{u}^* \cdot \nabla)\mathbf{u}^* = -\nabla p^* + \dfrac{1}{Re}\nabla^2 \mathbf{u}^* + N(\mathbf{J}^* \times \mathbf{B}^*) \\ \dfrac{\partial T^*}{\partial t^*} + (\mathbf{u}^* \cdot \nabla)T^* = \dfrac{1}{Pe}\nabla^2 T^* \\ \mathbf{J}^* = -\nabla V^* - \dfrac{\partial \mathbf{A}^*}{\partial t^*} + \mathbf{u}^* \times \mathbf{B}^* \\ \mathbf{B}^* = \nabla \times \mathbf{A}^* \\ \nabla^2 V^* = \nabla \cdot (\mathbf{u}^* \times \mathbf{B}^*) \\ \mathbf{J}^* = \dfrac{1}{R_m}\nabla \times \mathbf{B^*_{ind}} \\ \mathbf{B}^* = \mathbf{B^*_{imp}} + \mathbf{B^*_{ind}} \\ \nabla \cdot \mathbf{B}^* = 0 \end{cases} \tag{4-29}$$

The star as superscript for every variable indicates that is a dimensionless variable. Four are the dimensionless numbers appearing in this set of dimensionless equations. Their definition, based on the reference quantities selected making dimensionless the equations is:

- **Reynolds number**:

$$Re = \frac{\rho\ u_0\ L_0}{\mu} = \frac{u_0\ L_0}{\nu} \tag{4-30}$$

  As in conventional fluid mechanics, it is representative of the ratio of inertia, $\partial \mathbf{u}/\partial t + (\mathbf{u} \cdot \nabla)\mathbf{u}$, to viscous forces, $\nu \nabla^2 \mathbf{u}$.

- **Stuart number** (sometimes named also interaction parameter):

$$N = \frac{\sigma\ B_0^2\ L_0}{\rho\ u_0} \tag{4-31}$$

  It is representative of the ratio of the Lorentz force, $\mathbf{J} \times \mathbf{B}/\rho$, and inertia forces, $\partial \mathbf{u}/\partial t + (\mathbf{u} \cdot \nabla)\mathbf{u}$.

- **Peclet number**:

$$Pe = \frac{u_0\ L_0}{\alpha} \tag{4-32}$$

  where α is the thermal diffusivity (m^2/s). As in conventional fluid mechanics and heat transfer problems, it is representative of the ratio of the advection to conduction heat transfer rates found in the energy equation.

- **magnetic Reynolds number**:

$$R_m = \mu_0\ \sigma\ u_0\ L_0 = \frac{u_0\ L_0}{\lambda_m} \tag{4-33}$$

Name	Symbol	Definition	Significance
Reynolds number	Re	$\frac{\rho u_0 L_0}{\mu}$	Ratio of inertia to viscous forces
Stuart number	N	$\frac{\sigma B_0^2 L}{\rho u_0}$	Ratio of Lorentz forces to inertia
Peclet number	Pe	$\frac{u_0 L_0}{\alpha}$	Ratio of advection to conduction heat transfer rates
Magnetic Reynolds number	R_m	$\frac{u_0 L_0}{\lambda_m} = \mu_0 \sigma u_0 L_0$	Ratio of advection to diffusion of B

Table 4-1: The dimensionless groups of MHD

The magnetic Reynolds number has the same form of the Reynolds number. Indeed, the magnetic diffusivity ($\lambda_m = (\mu_0 \sigma)^{-1} [m^2/s]$) appears in the formula rather than momentum diffusivity. The magnetic Reynolds number, which appears only in the Ampére's law, is representative of the ratio of the advection to diffusion which turns out into the ratio of the induced magnetic field and the imposed magnetic field.

The dimensionless groups exposed above are of relevant importance. In fact, when they are large or very small, they allow to neglect certain terms in the governing equations greatly simplifying the problem. Table 4-1 provide a summary list of this dimensionless numbers with their symbols, definition and physic significance.

4-2-3 MHD simplified equations at low R_m

The three parameters that affects the magnitude of R_m are u_0, σ and L_0 . u_0 is important because if it is too low there will not be any significant induced field and if it is too high it can substantially alter the imposed field. The same considerations can be made for σ. L_0 is the reference length of the system. For example for a flow in a duct L_0 is the diameter. Its value id important because a certain current density $\mathbf{J}$ spread over a large area can induce a high magnetic field.

There may be different situations in MHD where R_m can be very large or very small. Its magnitude influences in practice, the kind of mutual interaction between the velocity field and the magnetic field. In particular if $R_m \ll 1$ the magnetic field induced by motion is negligible by comparison with the imposed field ($\mathbf{B_{ind}} \ll \mathbf{B_{imp}}$). The velocity field leaves the imposed magnetic field unperturbed [6]. However, the generation of a Lorentz force in the flow, can be strong so that the imposed magnetic field can alter the velocity field. Under these conditions there is a one-way coupling of $\mathbf{B}$ and $\mathbf{u}$: the magnetic field controls the velocity field (through the Lorentz force) but the velocity field doesn't substantially alter the imposed field.

In laboratory experiments or in industrial processes involving liquid metals MHD R_m is generally really low. Also in our case, as is discussed in Chapter 3, typical of R_m parameters are:

- $\sigma \sim 10^6\ \Omega^{-1} m^{-1}$

- $u_0 < 10\ m/s$
- $L_0 < 0.01$
- $\lambda_m = (\mu_0 \sigma^{-1}) \sim 1\ m^2/s$

Therefore it results: $R_m = \dfrac{u_0\ L_0}{\lambda_m} = \mu_0\ \sigma\ u_0\ L_0 \sim 0.001 \ll 1$

From a mathematical point of view if $R_m \ll 1$ the Ampére's equations can be dropped and eliminated from our set of equations. Also the constraint for $\mathbf{B}$ to be solenoidal become useless since the inducted magnetic field has not to be calculated and imposed magnetic field is already known. The dimensionless set of equations is so further simplified:

$$\begin{cases} \nabla \cdot \mathbf{u}^* = 0 \\ \dfrac{\partial \mathbf{u}^*}{\partial t^*} + (\mathbf{u}^* \cdot \nabla)\mathbf{u}^* = -\nabla p^* + \dfrac{1}{Re}\nabla^2 \mathbf{u}^* + N(\mathbf{J}^* \times \mathbf{B}^*_{\mathbf{imp}}) \\ \dfrac{\partial T^*}{\partial t^*} + (\mathbf{u}^* \cdot \nabla)T^* = \dfrac{1}{Pe}\nabla^2 T^* \\ \mathbf{J}^* = -\nabla V^* - \dfrac{\partial \mathbf{A}^*}{\partial t^*} + \mathbf{u}^* \times \mathbf{B}^*_{\mathbf{imp}} \\ \mathbf{B}^*_{\mathbf{imp}} = \nabla \times \mathbf{A}^* \\ \nabla^2 V^* = \nabla \cdot (\mathbf{u}^* \times \mathbf{B}^*_{\mathbf{imp}}) \end{cases} \tag{4-34}$$

All the assumption and simplifications that brought us to this final set of equations are now recalled:

- The fluid is newtonian, electrically conducting, non-magnetic and incompressible;
- Gravitational force contribution is neglected in the momentum and energy equations;
- Absence of source terms and negligible viscous dissipation term in the energy equation;
- ρ_e plays no significant role in the Lorentz force equations and in charge conservation equation, because it is too small in conductors traveling at much lower speed than light;
- In the Ampére-Maxwell equation the second term of the second member, the displacement current, is negligible by comparison with the current density;
- The liquid metal flows at low R_m so that the induced magnetic field is negligible by comparison with the imposed field.

Chapter 5

The Code

The code simulates a fluid flow between two parallel plates, as schematically shown in Figure 5-1. The main features of the flow are:

- Unsteady flow;
- Laminar flow;
- Incompressible fluid;
- Constant thermophysical properties;
- Newtonian fluid.
- Low magnetic Reynolds number.

In a laminar flow the motion of the particles of fluid is very orderly with all particles moving in regular paths and following the same stream lines. No fluctuations of any component of velocity are there.

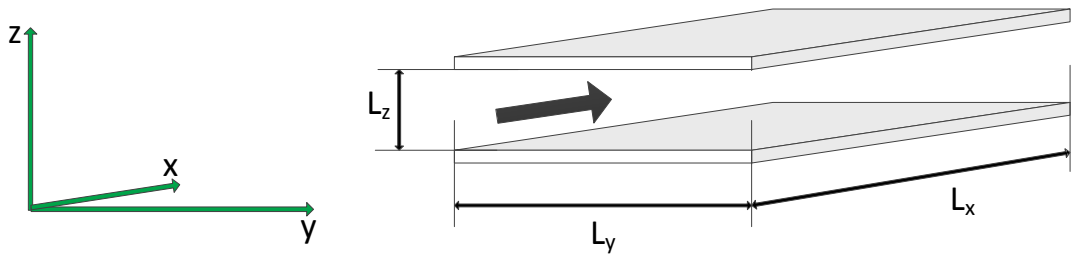

Figure 5-1: Flow between parallel plates

A fluid flow is laminar if the viscous forces overbear the inertia forces. The Reynolds number, defined as following, represents the ratio between the order of magnitude of inertial forces and viscous forces:

$$Re_{D_H} = \frac{u_b\ D_H}{\nu} = \frac{u_b\ D_H\ \rho}{\mu} = \frac{u_b\ 2\ L_z\ \rho}{\mu} \tag{5-1}$$

Where D_H and u_b are respectively the hydraulic diameter and bulk velocity, defined as:

$$D_H = \frac{4\ A_c}{P} = \frac{4\ L_y\ L_z}{2\ L_y} = 2\ L_z \quad [m] \tag{5-2}$$

$$u_b(x) = \frac{1}{A_c} \int_{A_c} u(y,z)\ dA_c \quad \left[\frac{m}{s}\right] \tag{5-3}$$

A_c is the flow cross-sectional area and P is the wetted perimeter of the channel. The bulk velocity is the same in each x coordinate of the channel for the mass conservation law.

When the Reynolds number is higher than a threshold value, called critical Reynolds number ($Re_{D_H,cri}$) the flow is not laminar anymore, but it becomes turbulent.

In turbulent flow the fluid particles do not travel in a well-ordered pattern. These particles possess velocities with macroscopic fluctuations at any point in the flow field. Even in steady turbulent flow, the local velocity components transverse to the main flow direction change in magnitude with respect to time [20].

For a parallel plate duct the critical Reynolds number is reported to be between 2200 and 3400, depending on the entrance configuration and disturbance sources [20].

5-1 Dimensionless equations

The code solves the following non-dimensional set of equations presented in the end of Chapter 4:

$$\begin{cases} \nabla \cdot \mathbf{u}^* = 0 \\ \dfrac{\partial \mathbf{u}^*}{\partial t^*} + (\mathbf{u}^* \cdot \nabla)\mathbf{u}^* = -\nabla p^* + \dfrac{1}{Re_\tau}\nabla^2 \mathbf{u}^* + N(\mathbf{J}^* \times \mathbf{B}^*_{\mathbf{imp}}) \\ \dfrac{\partial T^*}{\partial t^*} + (\mathbf{u}^* \cdot \nabla)T^* = \dfrac{1}{Pe_\tau}\nabla^2 T^* \\ \mathbf{J}^* = -\nabla V^* + \mathbf{u}^* \times \mathbf{B}^*_{\mathbf{imp}} \\ \nabla^2 V^* = \nabla \cdot (\mathbf{u}^* \times \mathbf{B}^*_{\mathbf{imp}}) \end{cases} \tag{5-4}$$

The term $-\dfrac{\partial \mathbf{A}^*}{\partial t^*}$ is here dropped in the Ohm's law since it is was not implemented in the code and only simulations with steady magnetic field were performed.

5-1-1 Reference values

The velocity profile for a fully developed laminar flow is parabolic:

$$u(z) = 6 \cdot u_b \, \frac{z}{L_z} \cdot \left(1 - \frac{z}{L_z}\right) \quad \left[\frac{m}{s}\right] \qquad 0 < \frac{z}{L_z} < 1 \tag{5-5}$$

The derivative of the velocity in wall-normal direction is:

$$\frac{du(z)}{dz} = 6 \cdot u_b \cdot \frac{1}{L_z} \cdot \left(1 - 2 \cdot \frac{z}{L_z}\right) \quad \left[\frac{1}{s}\right] \qquad 0 < \frac{z}{L_z} < 1 \tag{5-6}$$

Its value at the wall is:

$$\left.\frac{du(z)}{dz}\right|_{z=0} = \frac{6 \; u_b}{L_z} \quad \left[\frac{1}{s}\right] \tag{5-7}$$

Therefore in laminar flow the shear stress on the wall for a fully developed flow is:

$$\tau_w = \mu \left.\frac{du}{dz}\right|_{z=0} = \frac{6 \; \mu \; u_b}{L_z} \quad [Pa] \tag{5-8}$$

Equation 5-8 is important because the value of the shear stress at the wall appears in the definition of the friction velocity (u_τ). It is the velocity reference value used to make equations dimensionless and is defined in Equations 5-11.

The dimensionless value ψ^* of the generic quantity ψ is found by dividing that quantity by a reference value ψ_0 as follows:

$$\psi^* = \frac{\psi}{\psi_0} \tag{5-9}$$

All the quantities appearing in the equations and shown in the results presented afterwards are dimensionless. Here the reference values of all the quantities are listed:

- Length:

$$L_0 = L_z \; [m] \tag{5-10}$$

- Velocity:

$$u_0 = u_\tau = \sqrt{\frac{\tau_w}{\rho}} = \sqrt{\frac{6 \; \mu \; u_b}{L_z \; \rho}} = \sqrt{\frac{6 \; \nu \; u_b}{L_z}} \quad \left[\frac{m}{s}\right] \tag{5-11}$$

- Time:

$$t_0 = \frac{L_z}{u_\tau} \; [s] \tag{5-12}$$

- Electric current density in the liquid flow:

$$J_0 = \sigma \; u_\tau \; B_0 \left[\frac{A}{m^2}\right] \tag{5-13}$$

- Electrostatic potential:

$$V_0 = u_\tau \; B_0 \; L_z \; [V] \tag{5-14}$$

- Pressure difference:

$$\Delta p_0 = \rho \; u_\tau^2 \; [Pa] \tag{5-15}$$

- Lorentz force:

$$f_0 = \sigma \; u_\tau \; B_0^2 \; \left[\frac{N}{m^3}\right] \tag{5-16}$$

The reference value of magnetic field (B_0) and temperature difference (ΔT_0) are respectively derived in Subsection 5-1-3 and 5-1-4.

The physical properties appearing in these reference values are the properties of the fluid considered:

- Density: $\rho \left[\frac{kg}{m^3}\right]$;
- Electric conductivity: $\sigma \left[\frac{1}{\Omega \; m}\right] = \left[\frac{s^3 \; A^2}{kg \; m^3}\right]$;
- Dynamic viscosity: $\mu \left[\frac{kg}{m \; s}\right]$.

5-1-2 Dimensionless quantities

The set of equations 5-4 is made dimensionless using the reference values presented in the previous subsection. Here the dimensionless number appearing in the set of equations and other relevant dimensionless group are defined:

- Reynolds number:

$$Re = \frac{u_b \; L_z}{\nu} = \frac{\rho \; u_b \; L_z}{\mu} = \frac{Re_{D_H}}{2} \tag{5-17}$$

- Friction Reynolds number:

$$Re_\tau = \frac{u_\tau \; L_z}{\nu} = \sqrt{6 \; Re} \tag{5-18}$$

- Prandtl number:

$$Pr = \frac{\nu}{\alpha} = \frac{c_p \; \mu}{k} \tag{5-19}$$

- Friction Péclet number:

$$Pe_\tau = Re_\tau \; Pr \tag{5-20}$$

- Stuart number:

$$N = \frac{\sigma \; B_0^2 \; L_z}{\rho \; u_\tau} \tag{5-21}$$

5-1-3 Input parameters and magnetic field reference value

u_τ is used as reference velocity to make equations dimensionless. Therefore, Re_τ appears in the momentum equation of set 5-4 solved by the code. Re (defined in Eq. (5-17)) is set by the user as an input parameter and it directly relates to Re_τ from the Eq. (5-18).

Also the Stuart number (N) is imposed by the user. If the results of a simulation have to be converted in dimensional value ρ, σ, ν, L_z are known because they depend on the selected fluid and channel dimensions.

The friction velocity is found by Equation 5-18 as follows:

$$u_\tau = \frac{\nu}{L_z}\sqrt{6\ Re} \quad \left[\frac{m}{s}\right] \tag{5-22}$$

The magnetic field reference value (B_0) can finally be calculated from the definition of N (Eq. (5-21)):

$$B_0 = \sqrt{\frac{N\ \rho\ u_\tau}{\sigma\ L_z}} \quad [T] \tag{5-23}$$

The other input parameters are:

- Prandtl number: Pr
- Dimensionless length (L_x) and width (L_y) of the channel, being L_x the reference length;
- Mesh refinement: number of grid point in x, y and z direction (i_{max}, j_{max}, k_{max}).

5-1-4 Heat transfer consideration

The Nusselt number is here introduced. It is an important dimensionless group representative of the ratio between convective heat transfer and conductive heat transfer. The Nusselt number can be then expressed as:

$$Nu_{D_H} = \frac{h\ D_H}{k} \tag{5-24}$$

where h $[W/m^2K]$ is the local heat transfer coefficient and k $[W/m\ K]$ is the thermal conductivity of the fluid. All the simulations that were performed used the constant heat flux boundary condition on both the upper and lower wall.

Newton's law for convection gives the value of heat flux per unit area:

$$q_w = h\ (T_{m,w} - T_m) \quad \left[\frac{W}{m^2}\right] \tag{5-25}$$

T_m is the fluid bulk mean temperature that is computable from:

$$T_m(x) = \frac{1}{A_c \cdot u_b} \int_{A_c} u_x(y,z)\ T_x(y,z)\ dA \quad [K] \tag{5-26}$$

where A_c is the flow cross-sectional area and u_b is the bulk velocity, defined in Eq. (5-3). The bulk velocity is constant along all the channel for the mass conservation.

$T_{m,w}$ is the wall mean temperature defined as:

$$T_{m,w}(x) = \frac{1}{L_y} \int_{L_y} T_w(y,z)\ dy \quad [K] \tag{5-27}$$

By introducing the Newton's law in the Nusselt number definition it is obtained:

$$Nu = \frac{h\ D_H}{k} = \frac{q_w\ D_H}{k\ [T_{m,w}(x) - T_m(x)]} \tag{5-28}$$

The code calculates the Nusselt number by using dimensionless value. The Nusselt number definition based on dimensionless quantities is here derived:

$$Nu = \frac{h\ D_H}{k} = \frac{q_w\ D_H}{k\ (T_{m,w} - T_m)} = \frac{\frac{q_w\ L_z}{\Delta T_0\ k} \cdot \frac{D_H}{L_z}}{\frac{T_{m,w} - T_m}{\Delta T_0}} = \frac{q_w^*\ D_H^*}{T_{m,w}^* - \ T_m^*} \tag{5-29}$$

The dimensionless heat flux is therefore:

$$q_w^* = \frac{q_w\ L_z}{\Delta T_0\ k} \tag{5-30}$$

Being known the dimensional wall heat flux, q_w, the temperature difference reference value is readily found from Eq. (5-30)

$$\Delta T_0 = \frac{q_w\ L_z}{q_w^*\ k} \quad [K] \tag{5-31}$$

q_w^* is set to 1 in all the simulations. This choice is arbitrary and it was taken for sake of simplicity. Indeed, it has influence only on dimensionless quantities whereas, it does not affect the calculation of dimensional values. For instance if q_w^* doubles, the dimensionless fluid bulk mean temperature doubles as well in all the channel. However ΔT_0 is halved, so in the end the dimensional temperature field remains unchanged since :

$$T = T^* \Delta T_0 \quad [K] \tag{5-32}$$

5-2 Direct Numerical Simulation

The instantaneous set of equations can be solved in different ways. There are three methods used for solving the equations.

Turbulence models for the *Reynolds-averaged Navier-Stokes (RANS)* equations are the most used and focus their attention on the the mean flow and the effects of turbulence on the mean flow properties. In such models, the Navier-Stokes equations are firstly time averaged (or ensambled averaged in presence of time-dependent boundary conditions). Because of the interactions between various turbulent fluctuations, there are extra terms appearing in the averaged equations. These terms are modeled using classical turbulence models: among the best known are the $k - \varepsilon$ and the Reynolds stress models.

Another numerical method used for solving the Navier-Stokes equations is the *Large Eddy Simulation (LES)*: this is an intermediate form of turbulence calculations that intercepts the behavior of the larger eddies. The method involves space-filtering of the unsteady Navier-Stokes equations prior the computations, which passes the larger eddies and rejects the smaller ones. The latter are solved using an appropriate so-called sub-grid model. Since the unsteady equations are solved for the larger eddies, the LES is more demanding on computer resources in terms of storage and volume of calculations. However, this technique allows to approach even rather complex geometries.

A third method for solving the instantaneous set of Navier-Stokes equations is based on a *Direct Numerical Simulation (DNS)*. The equations are solved straightforwardly by means of discretization techniques only, without the use of turbulence models. The DNS makes use of spatial grids that are sufficiently fine to track even the smaller eddies length scales (the so-called Kolmogorov length scales) and with time steps sufficiently small to solve the period of the fastest fluctuations. On the other hand, this method is highly costly in terms of computational resources and therefore it is not used for industrial applications.

Moin and Mahesh [23] highlighted the benefits of using DNS (rather than RANS and LES). In first place, precise details of the turbulence parameters and their transport in the flow can be calculated with this method. This information can then be used to develop a qualitative understanding of the physics of the problem and lead to future developments of methods more easily implemented on a commercial scale (such as RANS). In second place, specific and advanced experimental techniques can be tested and evaluated in the DNS flow fields. Moreover, DNS approach is also the simplest from the conceptual point of view. On the other side it is more difficult to solve the equations with DNS because of the wide range of length and time scales caused by the appearance of eddies in the turbulent flow that would require to store big volumes of data and longer calculation times.

The code used in the project aims at investigating a laminar flow between two parallel plates and invested by a magnetic field. Therefore, there is no presence of turbulence structures and eddies and there is no need to track the properties of the flow at the smaller time and length scales. Furthermore, the geometry of the duct is very simple, so the mesh can be easily generated. Thus, requirements in terms of computational resources and calculation time are drastically reduced. This allows to easily apply the DNS method to the case studied. Note that the situation would be considerably different if the code needed to cope with a turbulent flow and more complex geometries.

5-3 The code's algorithm

In the this section the general functioning of the code is described and analyzed.

When a simulation is run, the following operation are executed before the starting of the main loop:

1) Initialization of velocity and temperature field in the all domain;
2) Definition of the magnetic field in all the domain;
3) Time-step upgrade.

The main loop solving algorithm is then executed; if it is not interrupted by the user it stops when it reaches a preset value of time iterations. The main algorithm steps are listed here:

4) Calculation of predicted velocity;
5) Calculation of temperature;
6) Solution of Poisson equation for pressure and correction of velocity field;
7) Solution of Poisson equation for electrostatic potential and calculation of Lorentz force;
8) Continuity equation check;
9) Generation of the outputs.

It is recalled that all the variables handled by the code (geometrical, thermo-dynamic, fluid-dynamic and magnetic) are dimensionless. From here on, for sake of simplicity, the symbol * is not used anymore, except in few cases in order to diversify dimensional and dimensionless variables.

In the next subsections a general description of the algorithm's conceptual steps is given.

1) Initialization of velocity and temperature field in the all domain

A hydrodynamically fully developed flow is defined before the main loop starts. The velocity component in y and z directions, respectively v and w are set to zero. The velocity component in x direction, u, is set as a parabolic function of the z coordinate in all the domain, as it follows:

$$u(z) = 6 \cdot u_b \cdot (z - z^2)$$

Velocities are initialized this way for all the simulation, except in the simulations performed for the hydrodynamic validation of the code presented in Subsection 5-5-1.

The temperature is always initially set to zero in all the domain.

2) Definition of the magnetic field in all the domain

As already discussed in Chapter 4, the induced magnetic field is negligible for low R_m flows, as those that the used code is able to simulate.

The imposed magnetic field is thus defined before the main loop starting and it remain the same for all the simulation. The equations and the system used to define the magnetic field are discussed in Chapter 6, where the simulations results are presented.

The magnetic field inside the channel is generated by a certain number of ideal wires current carrying. They are placed behind the plates and are directed orthogonally to the flow direction. Figure 5-2 shows by way of example one of possible wires layout. The Biot-Savart law describes the module of the magnetic field produced in the space by a wire current carrying as inversely proportional to the distance from the wire (r).

$$|\mathbf{B}(r)| = \frac{\mu_m \cdot I}{2\pi r} \quad [T] \tag{5-33}$$

μ_m $[H/m]$ is the magnetic permeability of the medium where the magnetic field is produced, I $[A]$ is the electric current flowing through the wire.

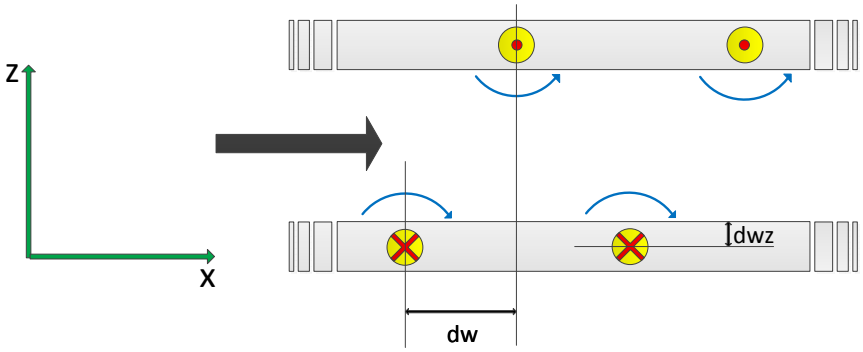

Figure 5-2: Magnetic field generation

The yellow circles indicate wires. The red crosses and the red dots represent respectively entering currents and outgoing currents. The blue arrows show the directions of the magnetic field generated by each wire. The black arrow represents the liquid metal flow.

In the code the dimensionless magnetic field ($\mathbf{B}^*$) produced by a single wire is calculated as follows:

$$|\mathbf{B}^*(r^*)| = \frac{0.5}{r^*} \quad [-] \tag{5-34}$$

Where r^* is the dimensionless distance of the considered point in the channel from the wire. The numerator of Eq. (5-34) was arbitrarily set to 0.5. This choice has influence only on dimensionless quantities whereas does not affect the calculation of dimensional values.

The total magnetic field in the all domain is calculated as the addition of the magnetic field generated by each single wire.

3) Time-step upgrade

The code calculates two characteristic time steps in every point of the grid, one related to the momentum equation and one to the energy equation. These two time steps differ for the presence of two different non-dimensional diffusivities: $1/Re_\tau$ and $1/Pe_\tau$, namely the momentum and energy diffusivities.

$$\Delta t_m = \left(\frac{|u|}{\Delta x} + \frac{|v|}{\Delta y} + \frac{|w|}{\Delta z} + \frac{\frac{1}{\Delta x^2} + \frac{1}{\Delta y^2} + \frac{1}{\Delta z^2}}{Re_\tau} \right)^{-1}$$
$$\Delta t_e = \left(\frac{|u|}{\Delta x} + \frac{|v|}{\Delta y} + \frac{|w|}{\Delta z} + \frac{\frac{1}{\Delta x^2} + \frac{1}{\Delta y^2} + \frac{1}{\Delta z^2}}{Pe_\tau} \right)^{-1} \tag{5-35}$$

The first three terms of these time steps are related to the advective terms of momentum and energy equations while the fourth term relates to the diffusive terms. The inverse of the terms links to the time step required for the calculation of advective and diffusive terms, respectively. The lower Δt_m and Δt_e the lower the time required to perform calculations.

The smallest of the two values in the domain is selected and the code checks if it respects the Courant-Friedrichs-Lewy (CFL) condition. Hence, the characteristic time is multiplied by the *Courant number* (C), which in the code is set to 0.1 and it is checked if it is lower than a threshold value ($\Delta t_{max} = 10^{-4}$):

$$min\{\Delta t_m, \Delta t_e\} \cdot C \leq \Delta t_{max} \tag{5-36}$$

If the above condition is respected, the code upgrades the time step to the new value, otherwise it uses the threshold value. A small Courant number and, therefore, a small Δt allows to decrease oscillations, improve accuracy of the solution and decrease numerical dispersion.

The subroutine executing time-step upgrade is called before the main loop but also at the beginning of every new iteration when the main loop starts.

4) Calculation of predicted velocity

The first step of the main loop consists of the discretization of the three momentum equations, and of the energy equation, in its form with temperature. These equation are

$$\begin{aligned}
&\frac{\partial u}{\partial t}+(\mathbf{u}\cdot\nabla)u=-\frac{\partial p}{\partial x}+\frac{1}{Re_\tau}\nabla^2 u+N(\mathbf{J}\times\mathbf{B})_x\\
&\frac{\partial v}{\partial t}+(\mathbf{u}\cdot\nabla)v=-\frac{\partial p}{\partial y}+\frac{1}{Re_\tau}\nabla^2 v+N(\mathbf{J}\times\mathbf{B})_y\\
&\frac{\partial w}{\partial t}+(\mathbf{u}\cdot\nabla)w=-\frac{\partial p}{\partial z}+\frac{1}{Re_\tau}\nabla^2 w+N(\mathbf{J}\times\mathbf{B})_z\\
&\frac{\partial T}{\partial t}+(\mathbf{u}\cdot\nabla)T=\frac{1}{Pe_\tau}\nabla^2 T
\end{aligned} \tag{5-37}$$

The set of momentum equations is first solved without pressure, having only three equations in the three velocity components. Subsequently, the pressure term is solved and used to advance the velocity field in time. Prior the time advancing procedure, the quantities $\partial u/\partial t$, $\partial v/\partial t$, $\partial w/\partial t$ are calculated using the velocities calculated at the previous, *n-th*, iteration. These three terms will be subsequently used in the time advancing method. The Lorentz force components of Eq. (5-37) are explicit and will be added afterwards, in the time advancing procedure. Therefore, the discretized set of Eq. (5-37), at time iteration n, without pressure gradient and source term is

$$\begin{aligned}
&\frac{\partial u}{\partial t}+\frac{\partial(uu)}{\partial x}+\frac{\partial(uv)}{\partial y}+\frac{\partial(uw)}{\partial z}=\frac{1}{Re_\tau}\left(\frac{\partial^2 u}{\partial x^2}+\frac{\partial^2 u}{\partial y^2}+\frac{\partial^2 u}{\partial z^2}\right)\\
&\frac{\partial v}{\partial t}+\frac{\partial(vu)}{\partial x}+\frac{\partial(vv)}{\partial y}+\frac{\partial(vw)}{\partial z}=\frac{1}{Re_\tau}\left(\frac{\partial^2 v}{\partial x^2}+\frac{\partial^2 v}{\partial y^2}+\frac{\partial^2 v}{\partial z^2}\right)\\
&\frac{\partial w}{\partial t}+\frac{\partial(wu)}{\partial x}+\frac{\partial(wv)}{\partial y}+\frac{\partial(ww)}{\partial z}=\frac{1}{Re_\tau}\left(\frac{\partial^2 w}{\partial x^2}+\frac{\partial^2 w}{\partial y^2}+\frac{\partial^2 w}{\partial z^2}\right)\\
&\frac{\partial T}{\partial t}+\frac{\partial(Tu)}{\partial x}+\frac{\partial(Tv)}{\partial y}+\frac{\partial(Tw)}{\partial z}=\frac{1}{Pe_\tau}\left(\frac{\partial^2 T}{\partial x^2}+\frac{\partial^2 T}{\partial y^2}+\frac{\partial^2 T}{\partial z^2}\right)
\end{aligned} \tag{5-38}$$

A prediction of the velocities time derivative at time iteration n is calculated as it follows:

$$\begin{aligned}
&\left(\frac{\partial u}{\partial t}\right)_p=-\frac{\partial(uu)}{\partial x}-\frac{\partial(uv)}{\partial y}-\frac{\partial(uw)}{\partial z}+\frac{1}{Re_\tau}\left(\frac{\partial^2 u}{\partial x^2}+\frac{\partial^2 u}{\partial y^2}+\frac{\partial^2 u}{\partial z^2}\right)\\
&\left(\frac{\partial v}{\partial t}\right)_p=-\frac{\partial(vu)}{\partial x}-\frac{\partial(vv)}{\partial y}-\frac{\partial(vw)}{\partial z}+\frac{1}{Re_\tau}\left(\frac{\partial^2 v}{\partial x^2}+\frac{\partial^2 v}{\partial y^2}+\frac{\partial^2 v}{\partial z^2}\right)\\
&\left(\frac{\partial w}{\partial t}\right)_p=-\frac{\partial(wu)}{\partial x}-\frac{\partial(wv)}{\partial y}-\frac{\partial(ww)}{\partial z}+\frac{1}{Re_\tau}\left(\frac{\partial^2 w}{\partial x^2}+\frac{\partial^2 w}{\partial y^2}+\frac{\partial^2 w}{\partial z^2}\right)
\end{aligned} \tag{5-39}$$

The Central Differencing Scheme (CDS) is used for both first and second spatial derivatives. Given a scalar quantity φ, the discretization of the first and second derivative around the

node i gives:

$$\left(\frac{\partial\varphi}{\partial x}\right)_i \approx \frac{\varphi_{i+1}-\varphi_{i-1}}{x_{i+1}-x_{i-1}}$$
$$\left(\frac{\partial^2\varphi}{\partial x^2}\right)_i \approx \frac{\varphi_{i+1}+\varphi_{i-1}-2\varphi_i}{(x_{i+1}-x_{i-1})^2} \tag{5-40}$$

Therefore, the spatial discretization method has a *second-order accuracy*. InFigure 5-3 the grid used for the discretization is shown. Each point is identified by the three indices *i, j, k* in the x, y and z directions respectively. The code uses a staggered arrangement for the grid. In this arrangement the scalar quantities (temperature, pressure and electric potential) and the magnetic field are calculated at nodal points whereas the flux components (velocity and current density) are calculated on a **staggered grid** centered around the cell faces. With this expedient, non-physical behaviors of the discretized momentum equations, due to oscillating pressure fields, can be avoided. Furthermore the velocity components are calculated exactly in the required positions for the scalar quantities calculations and the velocity components interpolation is not needed.

By way of example the staggered grid arrangement in $y-x$ plan is schematically represented in Figure 5-3.

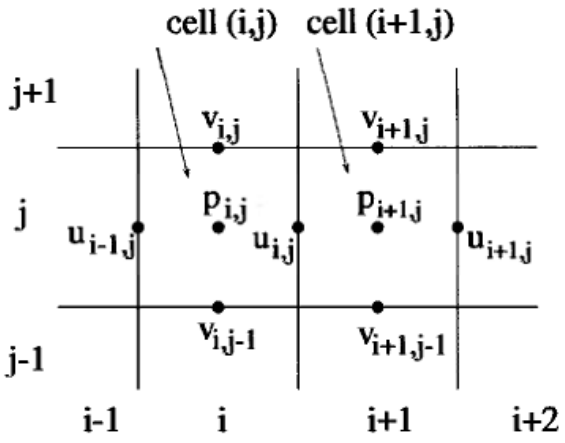

Figure 5-3: The staggered grid arrangement.

In the staggered configuration u and v are defined at the cell faces.

By applying the CDS for space discretization, the derivatives $\partial(uu)/\partial x$, $\partial(uv)/\partial y$ and $\partial^2 u/\partial x^2$ are respectively:

$$\frac{\partial(uu)}{\partial x} \cong \frac{u_{i+1/2}\ u_{i+1/2} - u_{i-1/2}\ u_{i-1/2}}{\Delta x} =$$

$$= \frac{\left(\frac{u(i,j,k)+u(i+1,j,k)}{2}\right)^2 - \left(\frac{u(i,j,k)+u(i-1,j,k)}{2}\right)^2}{\Delta x}$$

$$\frac{\partial(uv)}{\partial y} \cong \frac{(u_{j+1/2}\ v_{i+1/2}) - (u_{j-1/2}\ v_{i+1/2,\ j-1})}{\Delta y}$$

$$u_{j+1/2}\ v_{i+1/2} = \left(\frac{u(i,j,k)+u(i,j+1,k)}{2}\right)\left(\frac{v(i,j,k)+v(i+1,j,k)}{2}\right)$$

$$u_{j-1/2}\ v_{i+1/2,\ j-1} = \left(\frac{u(i,j,k)+u(i,j-1,k)}{2}\right)\left(\frac{v(i,j-1,k)+v(i+1,j-1,k)}{2}\right)$$

$$\frac{\partial^2 u}{\partial x^2} \cong \frac{u_{i+1} + u_{i-1} - 2u_i}{(\Delta x)^2} \tag{5-41}$$

A method for advancing velocity and temperature field in time is needed to gain the values at the new, $n+1$, iteration.

The code uses a **predictor-corrector method** for solving the pressure-velocity coupling, the **fractional step method**. This method (also called *projection method*) is an effective means of numerically solving time-dependent incompressible fluid-flow problems. It was originally introduced by Alexandre Chorin in 1967 and independently by Roger Temam as an efficient means of solving the incompressible Navier-Stokes equations [23]. The key advantage is that the computations of the velocity and the pressure fields are decoupled. A schematic representation of the main steps of the code and of the prediction-corrector algorithm is given in Figure 5-4

As it will be explained in detail in the next subsections, the method consists of a predictor step and then a corrector step. In the first one a "predicted" velocity field is found. Then, a specific equation provides the correction term to calculate the "corrected" velocity field. The predictor and corrector steps are derived from a multipoint method that advances the velocity field in time, the second-order **Adams-Bashforth method**. The method is applied to the three momentum equations in the following form:

$$\begin{aligned}
u^{n+1} &= u^n + \Delta t \left[\frac{3}{2}\left(\frac{du}{dt}\right)_p^n - \frac{1}{2}\left(\frac{du}{dt}\right)_p^{n-1} + \frac{\partial p}{\partial x}^{n+1} + {f_x}^n\right] \\
v^{n+1} &= v^n + \Delta t \left[\frac{3}{2}\left(\frac{dv}{dt}\right)_p^n - \frac{1}{2}\left(\frac{dv}{dt}\right)_p^{n-1} + \frac{\partial p}{\partial y}^{n+1} + {f_y}^n\right] \\
w^{n+1} &= w^n + \Delta t \left[\frac{3}{2}\left(\frac{dw}{dt}\right)_p^n - \frac{1}{2}\left(\frac{dw}{dt}\right)_p^{n-1} + \frac{\partial p}{\partial z}^{n+1} + {f_z}^n\right]
\end{aligned} \tag{5-42}$$

n refers to the current time iteration, *n+1* refers to the new iteration and *n-1* to the old. Δt is the time step used for the time discretization. The time discretization method has a *second-order accuracy.*

The subscript "p" indicates that the quantity stems from the predictor step of the predictor-corrector method. The predicted velocity derivatives are the one calculated by Equations 5-39. The quantity f indicates the Lorentz force; it is explicit, so it is calculated at the *n-th* iteration.

Eq. (5-42) can be decomposed into two parts, as following

$$\begin{aligned}
u_p^{n+1} &= u^n + \Delta t \left[\frac{3}{2}\left(\frac{du}{dt}\right)_p^n - \frac{1}{2}\left(\frac{du}{dt}\right)_p^{n-1} + {f_x}^n \right] \\
u^{n+1} &= u_p^{n+1} - \Delta t \, \frac{\partial p}{\partial x}^{n+1} \\
v_p^{n+1} &= v^n + \Delta t \left[\frac{3}{2}\left(\frac{dv}{dt}\right)_p^n - \frac{1}{2}\left(\frac{dv}{dt}\right)_p^{n-1} + {f_y}^n \right] \\
v^{n+1} &= v_p^{n+1} - \Delta t \, \frac{\partial p}{\partial y}^{n+1} \\
w_p^{n+1} &= w^n + \Delta t \left[\frac{3}{2}\left(\frac{dw}{dt}\right)_p^n - \frac{1}{2}\left(\frac{dw}{dt}\right)_p^{n-1} + {f_z}^n \right] \\
w^{n+1} &= w_p^{n+1} - \Delta t \, \frac{\partial p}{\partial z}^{n+1}
\end{aligned} \tag{5-43}$$

Therefore, for each direction, now two equation appear. The first of the two equations contains only velocity, its derivative in time at different time iterations and the force term. It is named the **predictor step**. Hence, the predicted values of velocities (u_p^{n+1},v_p^{n+1},w_p^{n+1}) from the known values of the previous n-th iteration, are calculated at iteration *n+1*. The second equation corresponds to the correction of the first equation by means of the new pressure gradient. This is called **corrector step**. Further details on the calculation of the pressure gradient term are given in the next subsection.

However, as it will be highlighted subsequently, the velocity will be corrected with the value of the gradient at the *n+1* iteration, in the correction step. At the end of the Adams-Bashforth iteration process, the values of the predicted du/dt , dv/dt , dw/dt at the iteration n become the values at the iteration $n-1$ in the next time cycle.

5) Calculation of temperature

The energy equation is discretized in time and solved differently from momentum equation. A semi-implicit discretization technique is used. The diffusive terms are discretized implicitly

while the convective terms explicitly. By separating the values of temperature at iteration $n+1$ from the values at n yields:

$$\frac{T^{n+1}}{\Delta t}Pe_\tau - \left(\frac{\partial^2 T^{n+1}}{\partial x^2} + \frac{\partial^2 T^{n+1}}{\partial y^2} + \frac{\partial^2 T^{n+1}}{\partial z^2}\right) = Pe_\tau \left(-\frac{T^n}{\Delta t} - \frac{\partial (Tu)^n}{\partial x} + \frac{\partial (Tv)^n}{\partial y} + \frac{\partial (Tw)^n}{\partial z}\right) \tag{5-44}$$

Space discretization using the CDS, Eq. (5-40), is applied to straightforwardly calculate the right-hand side of Eq. (5-44). Then, the code solves the equation firstly reducing it to a pentadiagonal system and secondly using a cyclic reduction algorithm. The temperature field T^{n+1} is therefore calculated at the new, $n+1$, iteration.

6) Poisson equation for pressure and correction of velocity field

The vectorial expression for the correction step equations of predictor-corrector method is:

$$\mathbf{u}^{n+1} = \mathbf{u_p}^{n+1} - \Delta t \ \frac{\partial p}{\partial \mathbf{x}}^{n+1} \tag{5-45}$$

where $\mathbf{u}^{n+1} = \mathbf{u}^{n+1}(u^{n+1}, v^{n+1}, w^{n+1})$ and $\mathbf{x} = \mathbf{x}(x, y, z)$. An equation for pressure is built up by taking the divergence of Eq. (5-45) and inserting continuity equation. Thus,

$$\nabla \cdot \mathbf{u}^{n+1} = \nabla \cdot \mathbf{u_p}^{n+1} - \Delta t \ \left(\nabla \cdot \frac{\partial p}{\partial \mathbf{x}}^{n+1}\right) \tag{5-46}$$

Since $\nabla \cdot \mathbf{u}^{n+1} = 0$ for continuity, the equation reduces to

$$\nabla^2 p^{n+1} = - \ \frac{\nabla \cdot \mathbf{u_p}^{n+1}}{\Delta t} \tag{5-47}$$

and using Cartesian coordinates

$$\frac{\partial^2 p}{\partial x^2}^{n+1} + \frac{\partial^2 p}{\partial y^2}^{n+1} + \frac{\partial^2 p}{\partial z^2}^{n+1} = -\frac{1}{\Delta t}\left(\frac{\partial u_p}{\partial x}^{n+1} + \frac{\partial v_p}{\partial y}^{n+1} + \frac{\partial w_p}{\partial z}^{n+1}\right) \tag{5-48}$$

This expression represents the **Poisson equation for pressure** or *pressure correction equation*. In the code this equation is solved, in all directions, using the CDS for space derivatives. At each time iteration, the implemented algorithm first calculates the right hand side of Eq. (5-48) and then solves the left hand side (Laplacian of pressure) using a numerical method based on Fourier transforms.

Once the new pressure field is found, the velocity field must be updated in order to introduce the new pressure gradient inside Eq. (5-42). The correction is made by adding the three components of the pressure gradient advanced in time (velocities corrections) to the three velocity components. At the $n+1$ iteration, the correction is such that the new values are

$$
\begin{aligned}
u^{n+1} &= u_p^{n+1} - \Delta t \left(\frac{p(i+1,j,k) - p(i,j,k)}{\Delta x} \right)^{n+1} \\
v^{n+1} &= v_p^{n+1} - \Delta t \left(\frac{p(i,j+1,k) - p(i,j,k)}{\Delta y} \right)^{n+1} \\
w^{n+1} &= w_p^{n+1} - \Delta t \left(\frac{p(i,j,k+1) - p(i,j,k)}{\Delta z} \right)^{n+1}
\end{aligned} \quad . \tag{5-49}
$$

where u^{n+1},v^{n+1} and w^{n+1} indicate the new, corrected values.

7) Poisson equation for the electrostatic potential and calculation of Lorentz force

As seen in Chapter 4, the reduced set of MHD equations comprises the Poisson equation for the electrostatic potential, V. This equation is solved similarly to the Poisson equation of pressure. The explicit equation for the potential is the following

$$\nabla^2 V = \nabla \cdot (\mathbf{u} \times \mathbf{B}) \tag{5-50}$$

$$\frac{\partial^2 V}{\partial x^2} + \frac{\partial^2 V}{\partial y^2} + \frac{\partial^2 V}{\partial z^2} = \frac{\partial}{\partial x}(vB_z - wB_y) + \frac{\partial}{\partial y}(wB_x - uB_z) + \frac{\partial}{\partial z}(uB_y - vB_x) \tag{5-51}$$

The above equation is discretized in the three directions and is solved using the Fourier transforms method. Then, at each iteration, the first term of current density vector is calculated as follows

$$\mathbf{J} = \mathbf{u} \times \mathbf{B} \tag{5-52}$$

that in the three direction reads

$$
\begin{aligned}
J_x &= vB_z - wB_y \\
J_y &= wB_x - uB_z \\
J_z &= uB_y - vB_x
\end{aligned} \quad . \tag{5-53}
$$

Then the V gradient is calculated and and embedded as the second term of Ohm's law. In the three directions the final values of the current density are

$$J_x = J_x - \frac{V(i+1,j,k) - V(i,j,k)}{\Delta x}$$
$$J_y = J_y - \frac{V(i,j+1,k) - V(i,j,k)}{\Delta y} \quad . \tag{5-54}$$
$$J_z = J_z - \frac{V(i,j,k+1) - V(i,j,k)}{\Delta z}$$

Once the electric current is corrected in the three directions, the code calculates the Lorentz force terms appearing in the momentum equations by taking the cross product of **J** and **B**:

$$f_x = N(\mathbf{J} \times \mathbf{B})_x = N(J_y B_z - J_z B_y)$$
$$f_y = N(\mathbf{J} \times \mathbf{B})_y = N(J_z B_x - J_x B_z) \quad . \tag{5-55}$$
$$f_z = N(\mathbf{J} \times \mathbf{B})_z = N(J_x B_y - J_y B_x)$$

Finally, this terms can be added to set of Eq. (5-42) in the new time iteration. A graphical representation of the overall code algorithm is given in Figure 5-4.

8) Continuity equation check

Once the velocity values are updated, the code provides a check on the discrete continuity equation. Numerical divergence is calculated in all the points of the grid. The code allows only solutions with a tolerance less than 10^{-10}.

9) Generation of the outputs

The code produces the following output:

- Nusselt number profiles on upper and lower walls along the x coordinate of the channel;
- Maps of the relevant variables (temperature, velocity components ...) in $z-x$ plan for $y = L_y/2$;
- 3-d maps of the relevant variable.

Outputs of the simulations performed for this thesis work are presented in the rest of this Chapter and in Chapter 6.

5-3-1 Boundary conditions

The dimensionless boundary condition imposed for the solution of equations are described here. They are classified according to the three spatial directions:

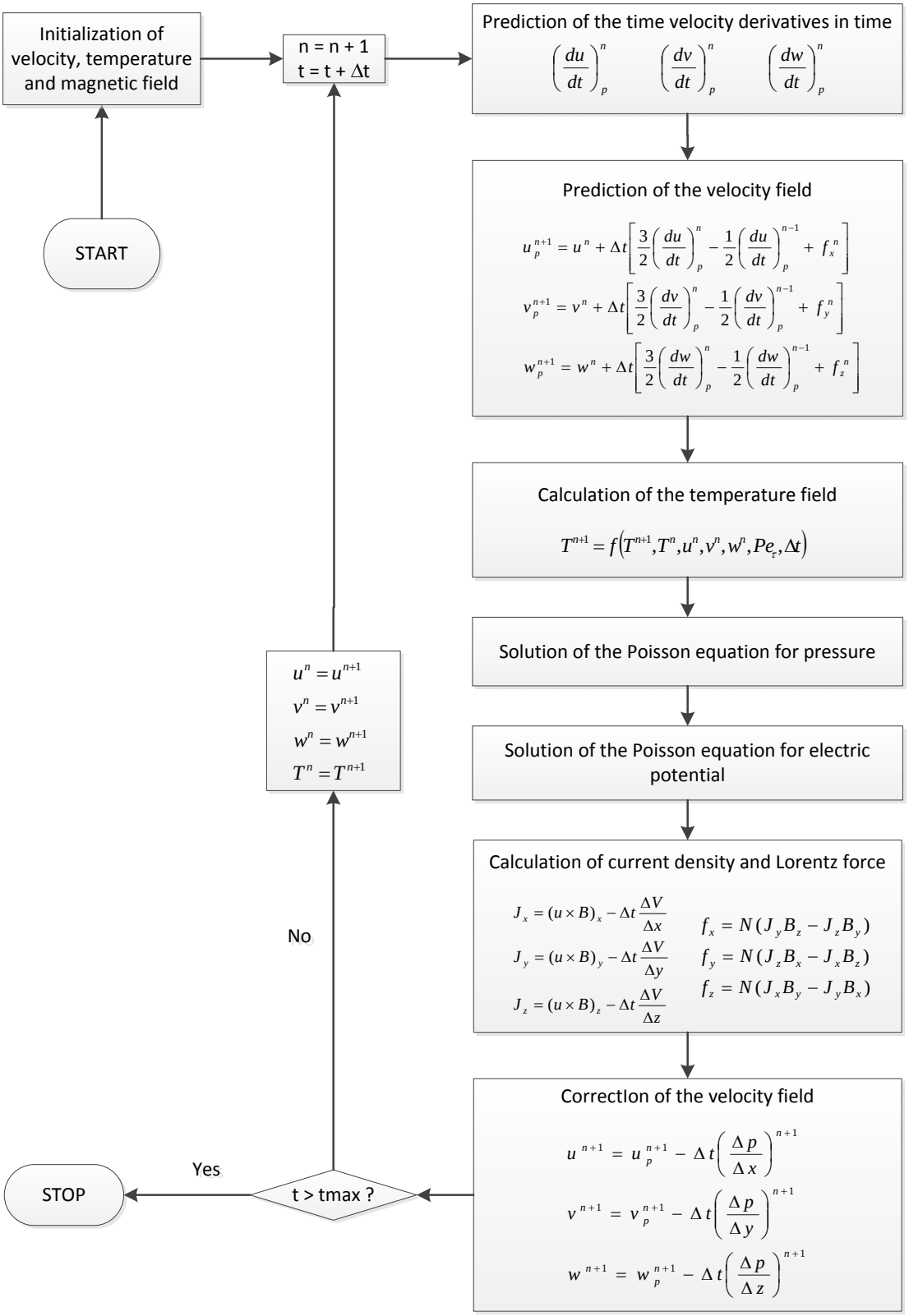

Figure 5-4: The code algorithm

Wallnormal direction

- Uniform and constant heat flux at each wall:

$$q_w = -\frac{dT}{dz}\bigg|_{z=0} \qquad q_w = -\frac{dT}{dz}\bigg|_{z=1} \tag{5-56}$$

- Non slip condition:

$$u(z=0)=0 \qquad v(z=0)=0 \qquad u(z=1)=0 \qquad v(z=1)=0 \tag{5-57}$$

- Walls impenetrability condition:

$$w(z=0)=0 \qquad w(z=1)=0 \tag{5-58}$$

- Electrically perfectly insulating wall:

$$J_z(z=0)=0 \qquad J_z(z=1)=0 \tag{5-59}$$

The Nusselt number calculation is based on the difference between wall temperature and bulk temperature (see Eq. (5-29)). Boundary condition of imposed heat flux at the walls was chosen instead of constant walls temperature boundary condition. This allows to have a finite value of the temperature difference independently on the length of the channel.

Spanwise direction

For the variables $u, v, w, T, J_x, J_y, J_z$ periodic boundary condition is applied in spanwise direction. This means that, as schematically shown in Figure 5-5, the value of the generic variable ψ in $y = 0$ is set equal to the value in $y = L_y$.

$$\psi(y=0) = \psi(y=L_y) \tag{5-60}$$

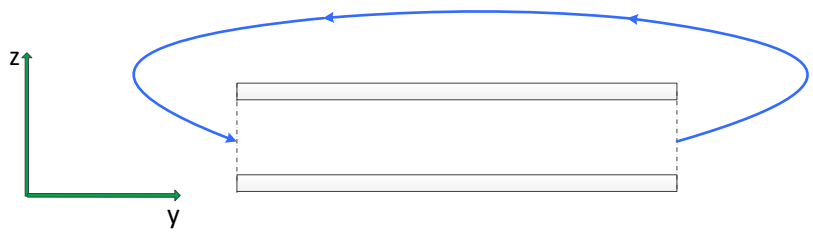

Figure 5-5: Periodic boundary condition in spanwise direction

This choice allows to avoid the influence of edges in y-direction, as if it was infinite.

Streamwise direction

Except for the simulations performed for the hydrodynamic validation of the code, which are presented in Subsection 5-5-1, an hydrodynamically fully developed flow is always considered at the channel inlet. The velocity components in y and z directions, respectively v and w, are set to zero. The velocity component in x direction, u, is set as a parabolic function of the z coordinate, as it follows:

$$u_{x=0}(z) = 6 \cdot u_b \cdot (z - z^2) \qquad v(x=0) = 0 \qquad w(x=0) = 0 \tag{5-61}$$

The temperature is always set to zero at the channel inlet.

$$T(x=0) = 0 \tag{5-62}$$

The extrapolation condition requires the derivatives of all the velocities in the direction normal to the boundary to be zero:

$$\left.\frac{\partial u}{\partial x}\right|_{x=L_x} = 0 \qquad \left.\frac{\partial v}{\partial x}\right|_{x=L_x} = 0 \qquad \left.\frac{\partial w}{\partial x}\right|_{x=L_x} = 0 \tag{5-63}$$

5-4 Parallel computing

The solution domain is subdivided in x direction into 16 sub-domains with dimensions $L_x/16, L_y, L_z$ (see Figure 5-6). 16 processors working in parallel were used, each of them running the code in a sub-domain. The objective of this subdivision is to reduce the calculation time by giving each processor the same amount of work to do. Exchange of data at the interface between two adjacent sub-domains is realized by means of specific Fortran functions.

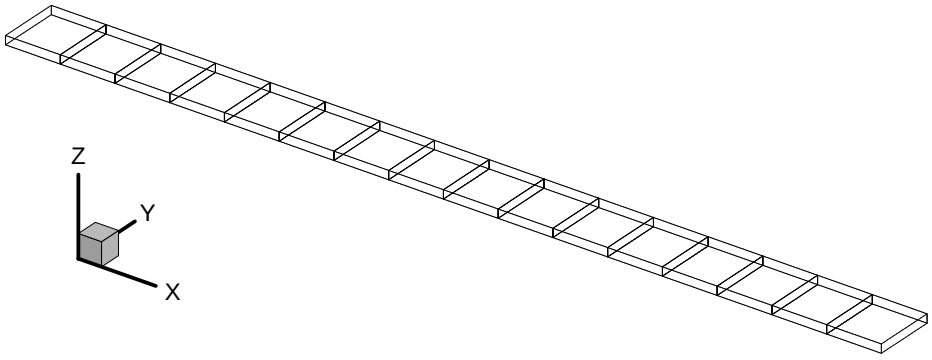

Figure 5-6: Domain subdivision

5-5 Code validation

5-5-1 Hydrodynamic entrance length

An *hydrodynamically developing flow* was simulated. In this type of flow velocity profile varies in the flow direction, in other words, the hydrodynamic boundary layer is developing [20].

The distance over which the velocity profile changes, i.e. the hydrodynamic layer develops is termed *hydrodynamic entrance length*. The latter can be defined as the length that leads to $u_c/u_{c,fd}$ equal to a certain value close to 1. u_c is the value of the velocity at the centerline, $u_{c,fd}$ is the value of the velocity at the centerline for the fully hydrodynamically developed flow.

A constant velocity profile at the inlet was given. For the simulated case, the hydrodynamic entrance length (HEL), defined based on $u_c/u_{c,fd}$ approaching the value 0.99, can be find as *Chen* (1973) proposed, by the following formula:

$$HEL \simeq 2\left(0.011 \cdot Re_{D_H} + \frac{0.315}{1 + 0.0175 \cdot Re_{D_H}}\right) \tag{5-64}$$

The hydrodynamic entrance length given by Eq. (5-64) is dimensionless, being L_z the reference length.

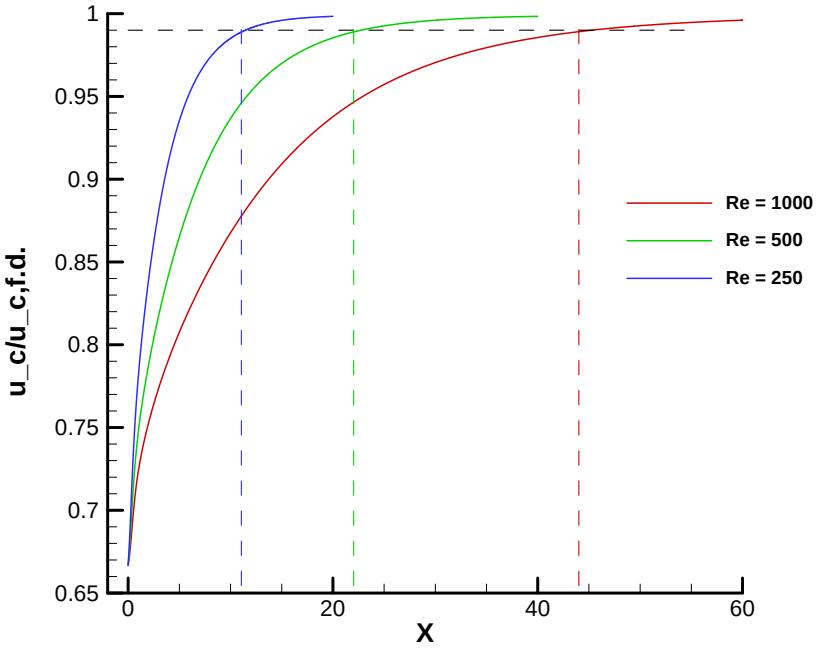

Figure 5-7: Validation: Hydrodynamic entrance length

Figure 5-7 shows $u_c/u_{c,fd}$ as a function of x coordinate for $Re_{D_H} = 500$, $Re_{D_H} = 1000$ and $Re_{D_H} = 2000$ (respectively $Re = 250$, $Re = 500$ and $Re = 1000$, from equation 5-17). The

theoretical hydrodynamic entrance lengths are respectively about equal to 11, 22 and 44. They are represented by the ashed vertical lines that cross the respective curve in $u_c/u_{c,fd} = 0.99$, as required by the analytical solutions [20].

5-5-2 Nusselt number profile

A *thermally developing flow* was simulated. In this type of flow, alternatively termed *thermal entrance flow*, the temperature profile is developing whereas the velocity profile is already developed [20]. In other words, the hydrodynamic boundary layer is already developed while the thermal boundary is developing.

As discussed previously, boundary condition of uniform heat flux at each wall is set, being the heat fluxes equal to each other.

Shah [21] developed the following set of equations that gives the Nusselt number trend as function of spatial coordinate in streamwise direction. These functions reproduce the results of the exact analytical solution within better than ± 1 %:

$$\begin{cases} Nu_{D_H}(x^*) = 1.490 \cdot x^{*-1/3} & for \quad x^* \leq 0.0002 \\ Nu_{D_H}(x^*) = 1.490 \cdot x^{*-1/3} - 0.4 & for \quad 0.0002 < x^* \leq 0.001 \\ Nu_{D_H}(x^*) = 8.235 + 8.68 \cdot (1000 \cdot x^*)^{-0.506} \cdot e^{-164 \cdot x^*} & for \quad x^* > 0.001 \end{cases} \tag{5-65}$$

Where x^* is defined as: $x^* = \dfrac{x}{Re_{D_H} \cdot Pr \cdot D_H}$

For the kind of boundary conditions used, analytical solution gives for thermally developed condition: $Nu_{D_H}(\infty) = 140/7 \simeq 8.235$.

The distance over which the Nusselt number changes, i.e. the thermal boundary layer develops is termed *thermal entrance length*. The thermal entrance length (TEL), defined based on Nu_{D_H} approaching the value of 140/17 within 5%, is [24]:

$$x^* = THL \simeq 0.0115439 \tag{5-66}$$

$$Nu_{D_H}(THL) \simeq 1.05 \cdot Nu_{D_H}(\infty) \simeq 1.05 \cdot 8.235 \simeq 8.647 \tag{5-67}$$

Figure 5-8 shows the comparison between the calculated Nusselt profile (thin blue Line) and the theoretical profile (thick green line) for Re=1000 and different values of Prandtl Number (10, 1 and 0.1), which are indicated in the captions. The set of Equations 5-65 reproduces the results of the analytical solution considering negligible the axial conduction. Such approximation is valid for $Pe = Re_{D_H} \cdot Pr > 50$ [20]. This condition is respected in all the three cases, for Re_{D_H}=2000 ($Re = 1000$) and Pr=0.1, in fact, Pe=200.

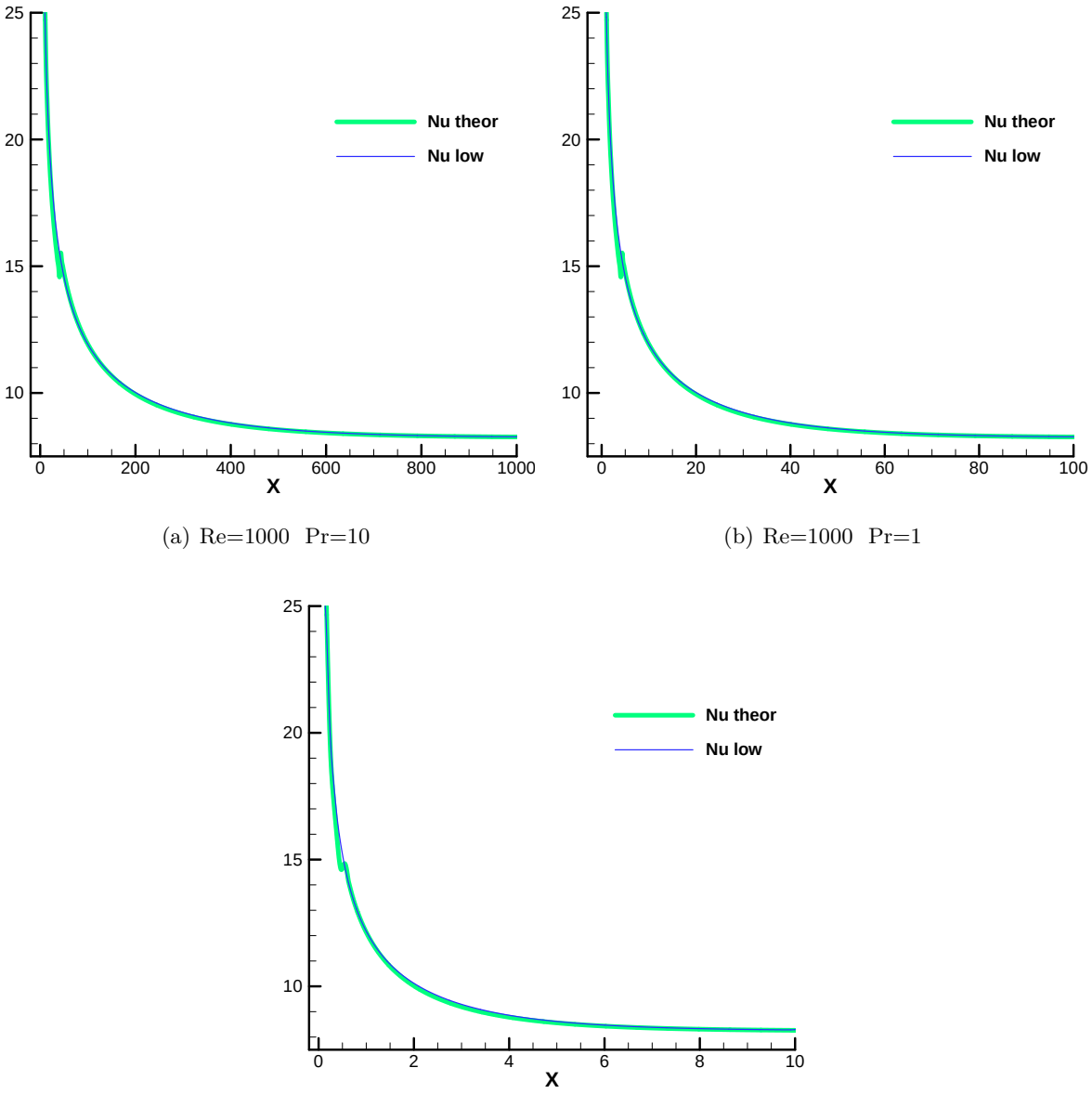

(a) Re=1000 Pr=10

(b) Re=1000 Pr=1

(c) Re=1000 Pr=0.1

Figure 5-8: Validation: Nusselt number profile

5-5-3 Hartmann flow

It is wanted now to give a proof of correct operation of subroutines describing the influence of magnetic field on the velocity field. In order to do that a flow between the two parallel plates with an imposed uniform magnetic field acting in the direction orthogonal to the plates was simulated. Figure 5-9 shows schematically the described phenomenon. A laminar flow of an electrically conducting and viscous liquid in the condition above described is one of the simplest problems in Magnetohydrodynamics (MHD). It was studied for the first time by Hartmann and it is therefore called **Hartmann flow** [6].

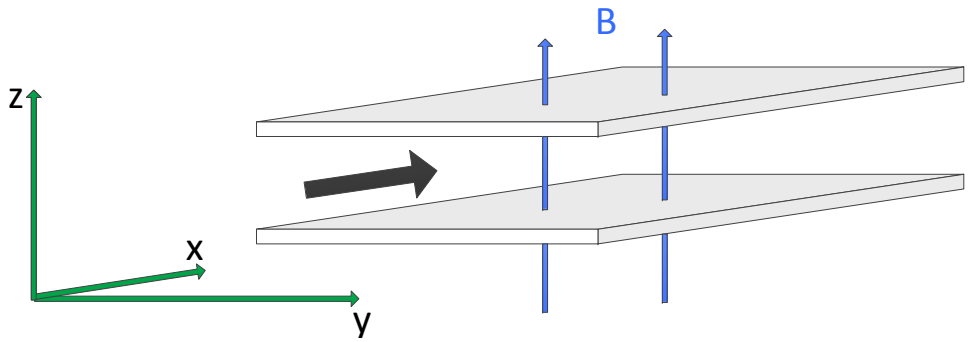

Figure 5-9: Hartmann problem

The gray arrow represents the liquid metal flow, the two blue arrows crossing the plates represent the uniform magnetic field.

For this problem it is possible to find analytically the velocity profile, which comes out to be:

$$u(z) = \frac{C}{u_b} \cdot \left[1 - \frac{cosh\left(\frac{1}{2} Ha \cdot (2z-1) \right)}{cosh\left(\frac{1}{2} Ha \right)} \right] \qquad 0 \leq z \leq 1 \tag{5-68}$$

$$C = \int_{L_z} \left[1 - \frac{cosh\left(\frac{1}{2} Ha \cdot (2z-1) \right)}{cosh\left(\frac{1}{2} Ha \right)} \right] dz \tag{5-69}$$

The Hartmann number (Ha) is a dimensionless number given by the combination of Re_τ and N:

$$Ha = \sqrt{Re_\tau \cdot N} = B_0 \cdot L_z \cdot \sqrt{\frac{\sigma}{\rho \nu}} \tag{5-70}$$

$(Ha)^2$ represents the ratio of the Lorentz force to viscous forces.

The value of B_0 in the Hartmann number definition is the value of the imposed magnetic field. Therefore the value to be assigned to the dimensionless uniform magnetic field in the code is 1:

$$B = B^* \cdot B_0 = 1 \cdot B_0 = B_0 \tag{5-71}$$

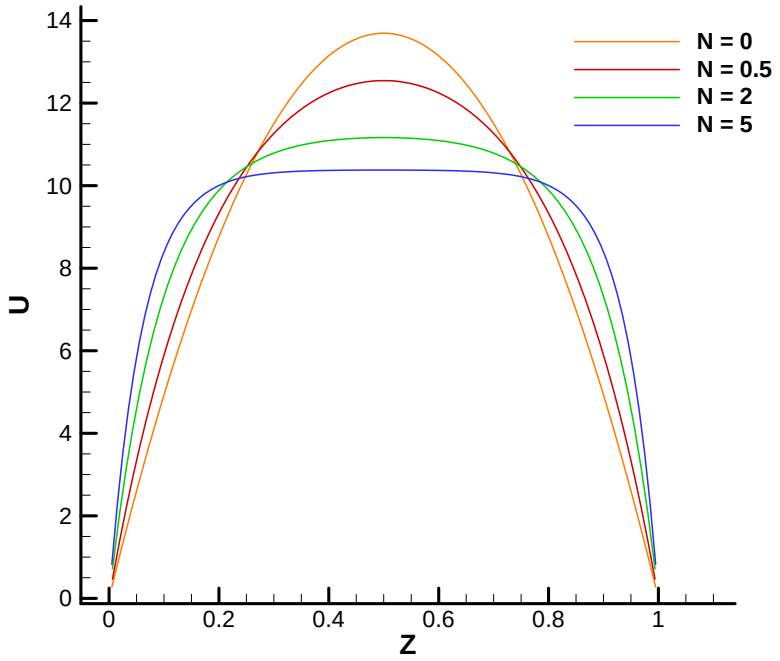

Figure 5-10: Velocity profiles of Hartmann flows with Re=500 and different Stuart number (N)

Velocity profiles, analytically calculated, of a flow with $Re = 500$ and different values of Stuart number are shown in Figure 5-10. The analysis of this simple problem can help to understand the kind of action that the magnetic field has on the velocity field. The higher the Stuart number, the flatter the velocity profile; if $N = 5$, for instance, the velocity profile has a shape that reminds the one of a turbulent flow.

The Lorentz force, in fact, acts in a direction opposite to that of the motion. By using the right hand rule we find the direction of the current density ($\mathbf{J} = \mathbf{u} \times \mathbf{B}$) to be oriented in the positive direction of y axis. By using again the right hand rule we find the direction of the Lorentz force ($\mathbf{f} = \mathbf{J} \times \mathbf{B}$) to be oriented in the negative direction of x axis, i.e. in the direction opposite to the fluid flow.

Figure 5-11 shows electric current density and Lorentz force for $Re = 500$ and $N = 0.5$ in $x - z$ plans. Their value is not function of x and y coordinate. A portion of the channel with x between 45 and 49 is shown. Only the y direction component of the current density and the x direction component of the Lorentz force are shown because other components are equal to zero in all the domain.

The comparison between analytical and numerical velocity profiles is depicted in Figure 5-12. The maximum error of the numerically calculated profile respect to the analytical solution is less than 1 % in all four cases. In fact the thin blue line, which represents the profile calculated by the code, almost perfectly overlaps the thick green line, which represents the exact analytical solution.

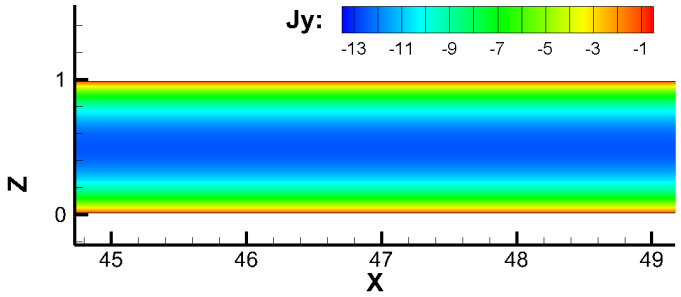

(a) Current density in y direction

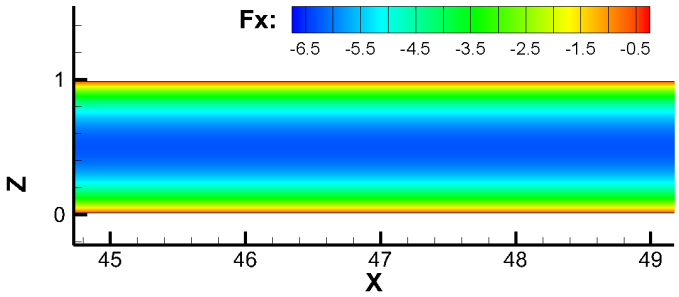

(b) Lorentz force in x direction

Figure 5-11: Hartmann flow: current density and Lorentz force for $Re = 500$ and $N = 0.5$

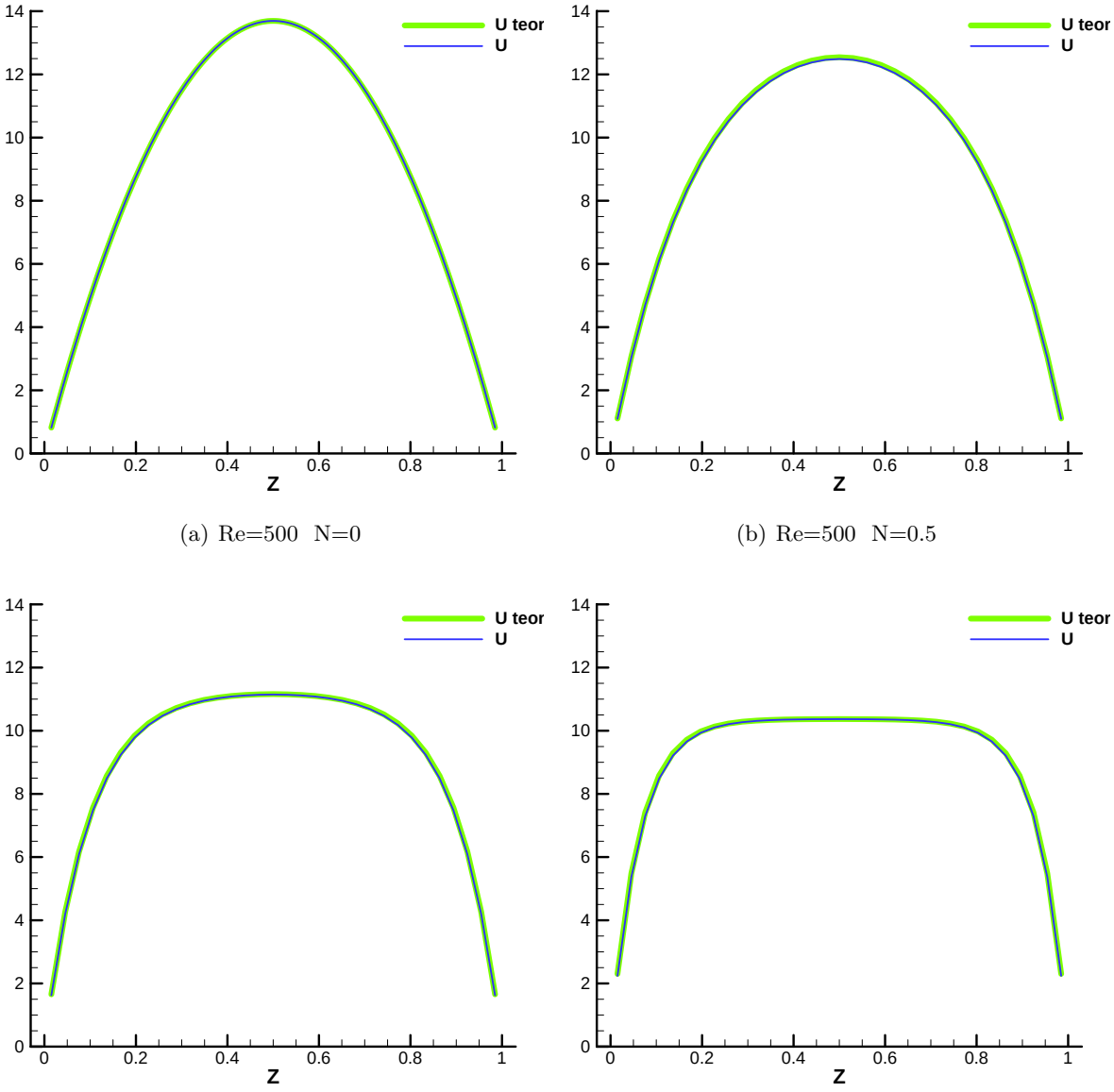

(a) Re=500 N=0

(b) Re=500 N=0.5

(c) Re=500 N=2

(d) Re=500 N=5

Figure 5-12: Validation: Hartmann flow

Chapter 6

Simulation Results

When the work with the DNS code described, in Chapter 5, began the input parameters were the following:

- Dimensionless groups: Re, Pr, N;
- Number of wires (nw);
- Number of processors working in parallel (px);
- Three dimensions of channel: L_x, L_y and L_z, indicated in Figure 6-1;
- Mesh refinement: number of grid point in x, y and z direction (i_{max}, j_{max}, k_{max}).

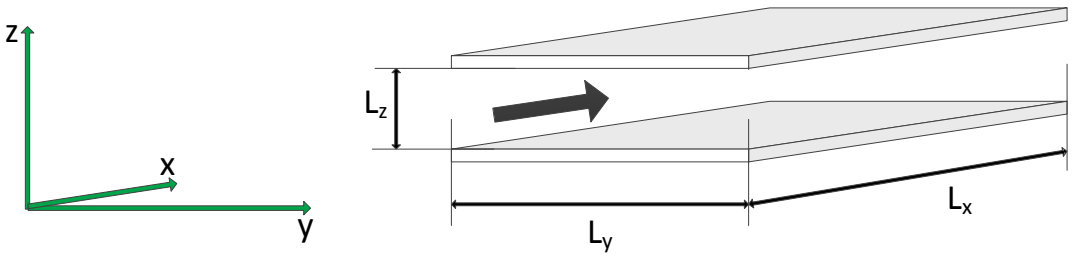

Figure 6-1: Parallel plates duct

The aim of the simulations performed and presented in this chapter is to study the effect of non-uniform magnetic fields on the convective heat transfer of a liquid metal flow. To modify the magnetic field inside the channel the wires layout has to be changed. In order to allow the user to easily choose some parameters characterizing the wires configuration, the following new input parameters were introduced:

- mfw: x coordinate of the first wire;
- dw: distance in x direction between two consecutive wires;
- mlw: the distance between the last wire and the end of the channel;

- dwz: distance of wires from the walls;
- A parameter that allows to choose whether to put even wires (second, fourth, sixth ...) under the bottom plate or over the upper plate;
- A parameter that allows to choose whether the current of even wires has to be entering or outgoing.

Figure 6-2(a) shows a graphic representation of these parameters. After their introduction L_x was not anymore a parameter directly set, but it was dependent on nw, mfw and mlw;

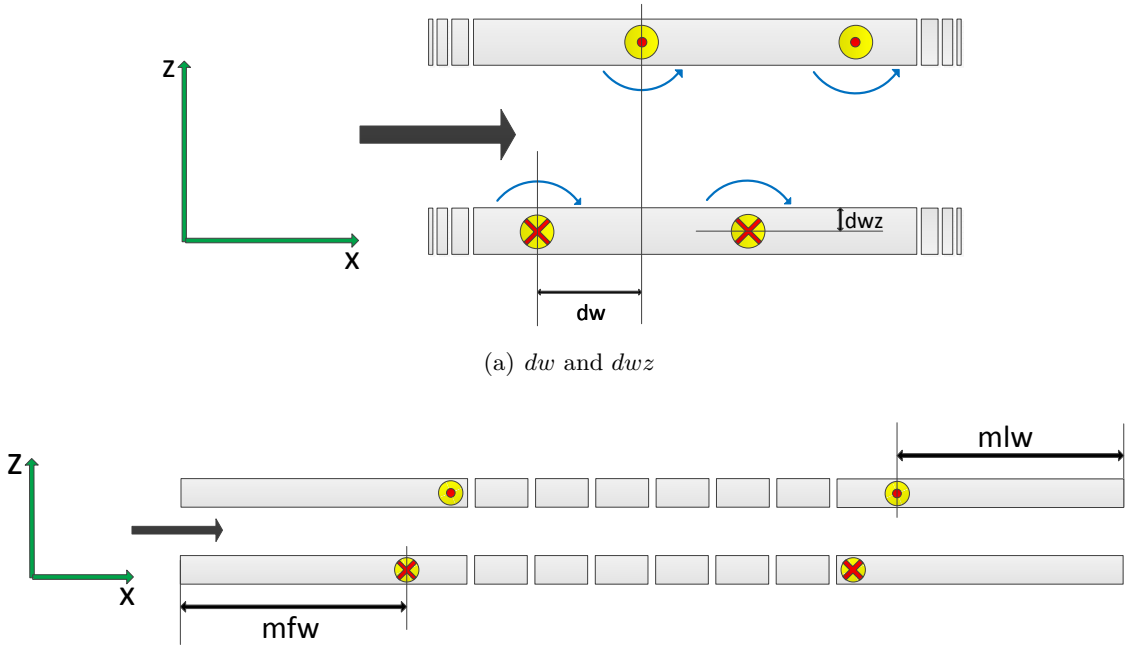

(a) dw and dwz

(b) mfw and mlw

Figure 6-2: Wires layout parameters

The yellow circles indicate the wires, directed orthogonally to the plan $z - x$. The red crosses and the red dots represent respectively entering currents and outgoing currents. The blue arrows show the directions of the magnetic field generated by each wire. The black arrow represents the liquid metal flow.

Four different wires layouts were evaluated on the basis of the produced Nusselt number distribution along the channel. An analysis of relevant physical quantities inside the channel, as magnetic field and velocity, was performed. Finally the influence of some dimensionless parameters on the heat transfer enhancement was assessed.

6-1 Different wires configurations

Position and current direction of odd wires cannot be changed. It is however possible to select the position and the current direction of even wires. In other words it is possible to choose whether wires have to be staggered or all of them behind the same wall and whether

the currents flowing in odd and even wires have to be the same or the opposite. The possible configurations are consequently four; they are schematically shown in Figure 6-3.

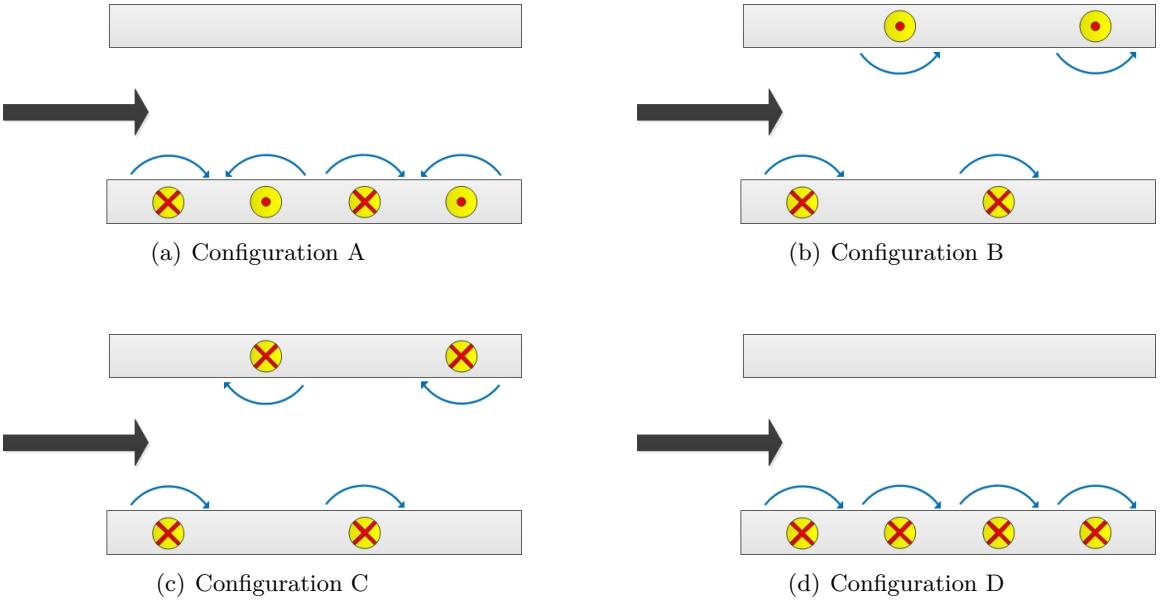

(a) Configuration A (b) Configuration B

(c) Configuration C (d) Configuration D

Figure 6-3: Four possible wires configurations

This four configurations were compared on the basis of the Nusselt number profile along streamwise direction. In the four simulated cases, a part from the wires position and currents direction, all the others characteristic parameters are the same:

- nw (number of wires) $= 30$
- dw (distance between wires in x direction) $= 3$
- dwz (distance between wires and walls) $= 0.5$
- $Re = 500$
- $Pr = 0.03$
- $N = 2$

It is recalled that the parameters dw and dwz are dimensionless, being L_z the reference length.

In all the simulations presented in this Chapter the flow is hydrodynamically developed at the channel inlet (parabolic velocity profile). The dimensionless temperature is set equal to zero in all the channel at the simulation starting. Always boundary condition of constant heat flux at both the walls was used, being the dimensionless heat flux equal to one. All the simulations results presented here concern the steady state. The achievement of steady state conditions was graphically verified, in particular the simulation was stopped when the Nusselt number profile along x did not change in time anymore.

As mentioned in Chapter 5, the Nusselt number value in absence of magnetic field is 8.235 for the thermally developed flow with uniform heat fluxes at the channel walls. This value is the reference used to evaluate the effectiveness of a magnetic field application in order to enhance the heat transfer between wall and liquid metal. Figure 6-4 and Figure 6-5 show the

Nusselt profiles for the four different configurations on the lower and upper wall, respectively represented with red and blue line.

6-1-1 Configuration A

Figure 6-4 (a) - The first wire is at $x = 20$. The Nusselt number on the upper wall reaches quickly an average value 9 % higher than 8.235. After the last wire, positioned at $x = 107$ the Nusstelt number gets rapidly back to 8.235. The effect on the lower wall is analogous, but the Nusselt number decreases of about 5 %. The oscillations of the Nusselt number around the average value have a spatial period equal to dw and they are greater on the upper wall.

6-1-2 Configuration B

Figure 6-4 (b) - The first wire is at $x = 20$. The magnetic field lines are oriented respect to the upper wall exactly as they are respect to the lower wall. Consequently the Nusselt profiles on the upper and on the lower wall are identical, but offset from each other by dw. The average Nusselt number is 1.4 % higher than the non-magnetic case and the fluctuations amplitude is greater than that obtained with *configuration A*.

6-1-3 Configuration C

Figure 6-5 (a) - The Nusselt number profiles on the two walls are very similar. They start increasing well before the first wire, which is positioned at $x = 70$. The Nusselt number on the two walls do not oscillate around a constant value, but around an "U" shape curve. The amplitude of oscillations decreases going from the external wires toward the internal ones. On the first wire the Nusselt numbers has the highest peak (around 13.5 % higher than 8.235 on the upper wall). The peak on the last wire is a bit lower. On the central wires the average Nusselt numbers value is around the undisturbed value (8.235).

6-1-4 Configuration D

Figure 6-5 (b) - As in the *configuration C* the Nusselt numbers starts increasing well before the first wire, therefore also in this case the firs wire was positioned at $x = 70$. Also in this configuration the Nusselt number on the two walls oscillates around a "U" shape curve. Unlike the *configuration C* the profile on the upper wall is above the profile on the lower wall. The amplitude of oscillations is more or less constant. On the first wire the Nusselt number has the highest peak (around 15 % higher than 8.235 on the upper wall). The peak on the last wire is a bit lower. On the central wires the Nusselt Number on the lower wall is around the undisturbed value, while on the upper wall it is about 2 % greater.

6-1-5 Magnetic field effect on the Nusselt number

The magnetic field acts on the flow mainly through its component in z direction (B_z). In fact the current density is given by the cross product between $\mathbf{B}$ and $\mathbf{u}$, and B_z is orthogonal to the flow direction, while B_x is parallel.

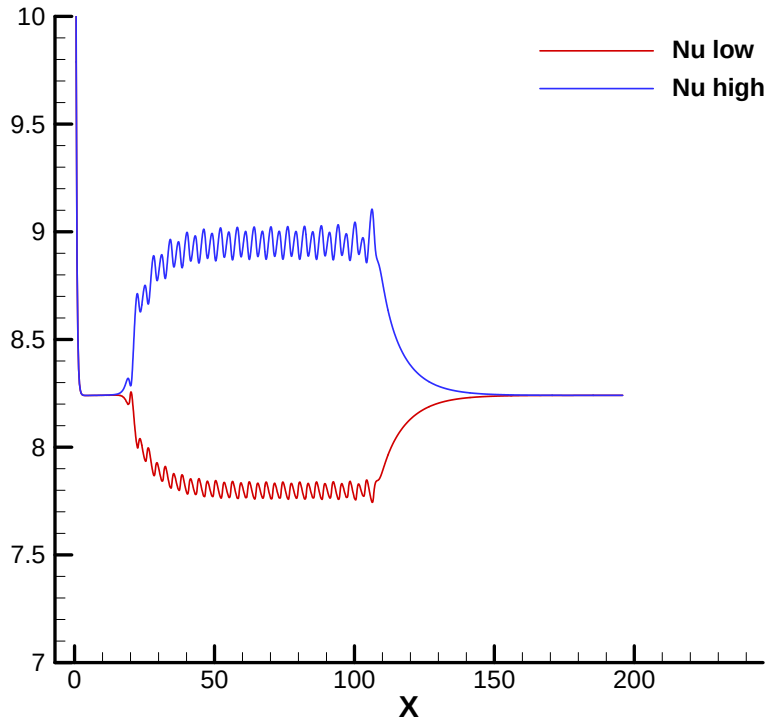

(a) Nusselt number profiles for configuration A

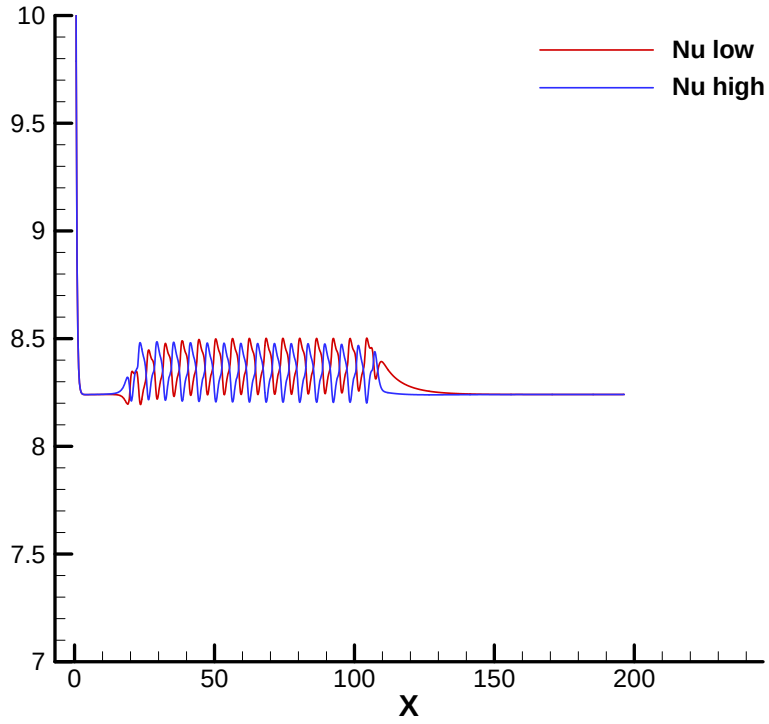

(b) Nusselt number profiles for configuration B

Figure 6-4: Nusselt number profiles for configurations A and B

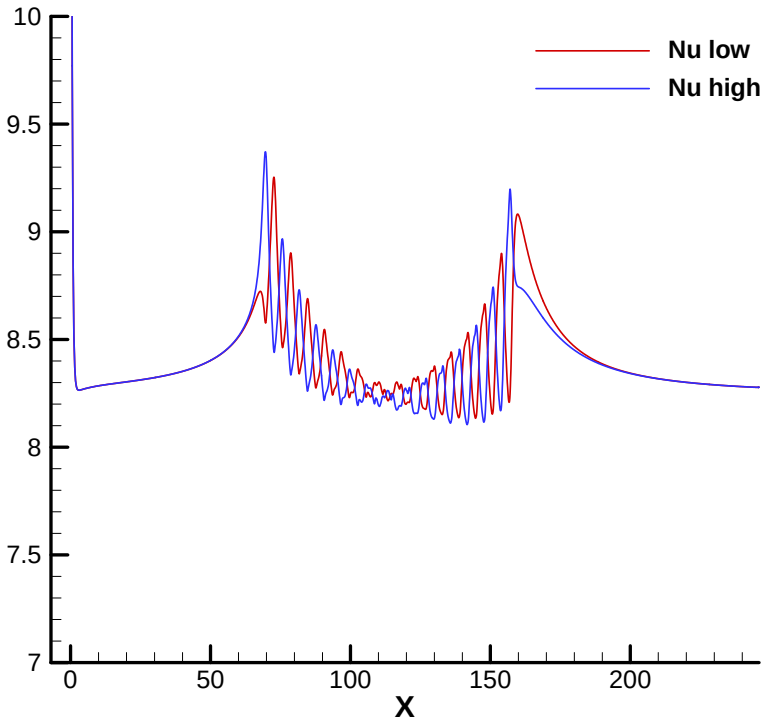

(a) Nusselt number profiles for configuration C

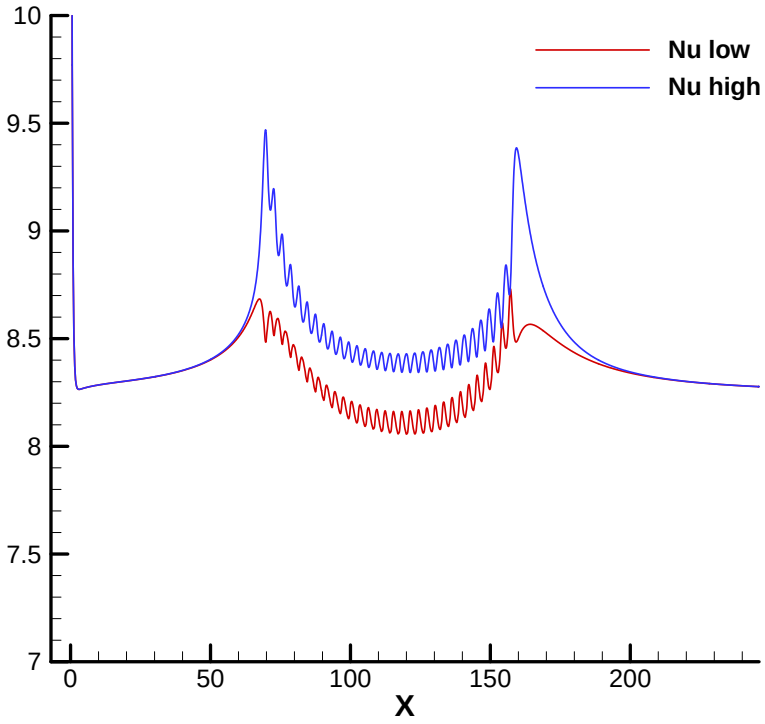

(b) Nusselt number profiles for configuration D

Figure 6-5: Nusselt number profiles for configurations C and D

Figure 6-6 shows the magnetic field component in z direction in the four configuration. The channel region where last wires are and the region immediately after are shown. In configuration A and B B_z varies periodically along x and goes to zero shortly after the last wire. In configuration C and D, conversely, B_z has low values before the last wire, but it rapidly rises going towards the last wire. On that point B_z reaches its maximum value, higher in module than in configuration A and B. In configuration C and D B_z decreases much more slowly after the last wire rather than in configuration A and B.

6-2 The selected configuration - relevant quantities analysis

Configuration A seems to be the most interesting among the four. It has the advantage that in the region where the wires are the Nusselt number oscillates around a constant value that deviates considerably from the reference value (8.235). It is higher on the upper wall and lower on the lower wall. A further advantage with respect to other configuration is that the oscillations amplitude is small and constant, so that the temperature of the cooled surface is more uniform.

In this section an analysis of all the most relevant physical quantities characterizing the flow with wires in *configurations A* is carried out. In figures from 6-8 to 6-11 show the values of these quantities in $z-x$ planes. In order to keep the ratio between x and z axis equal to 1 and, at the same time, to have pictures of the analyzed domain enough high, a limited range of x coordinate is shown. This range is between 55 and 69, so it is approximately in the middle of the space where the wires are. $z-x$ planes graphs are shown because all the quantities do not depend on the y coordinate. Figure 6-7 shows by way of example the Lorentz force component in x direction in an $x-y$ plane, being $z = 0.5$.

6-2-1 Magnetic field

In Figures 6-8 (a) and (b) the magnetic field components in x and in z direction are shown. Semicircular areas with positive and negative component in x direction alternate. This semicircles are centered in the wires position. Half-moon shape areas with positive and negative magnetic component in z direction alternate. Each of these areas stretches between two wires. In fact two wires adjacent develop a magnetic field with the same direction of the z component in the space between them. The component of the magnetic field in y direction is not shown since it is equal to zero in all the domain.

In Figure 6-8 (c) the magnetic field modulus is shown.

6-2-2 Electric current density

Figure 6-9 (a) shows the electric current density component in y direction. Approximately oval shape areas with positive and negative values of current density alternate. Like for the magnetic field component in z direction each of these areas stretches between two adjacent wires.

Boundary condition of perfect electrically insulating walls was used, so the electric current in z direction was imposed to be equal to zero on the walls. For all the four configuration the

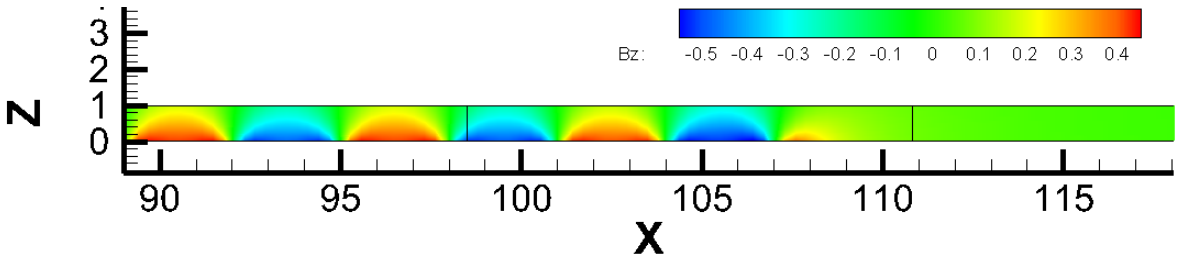

(a) Configuration A

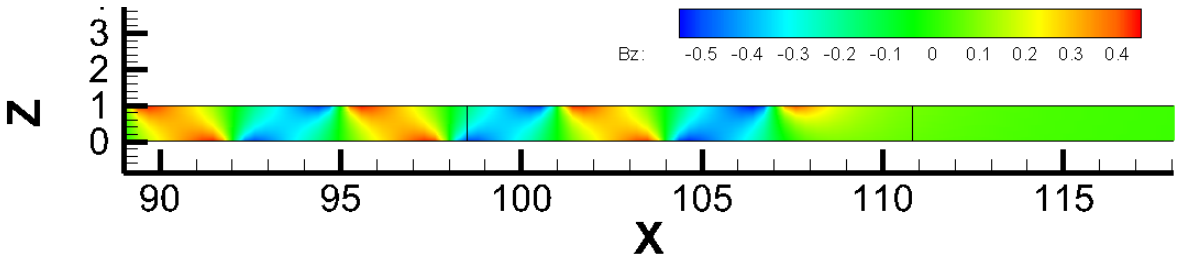

(b) Configuration B

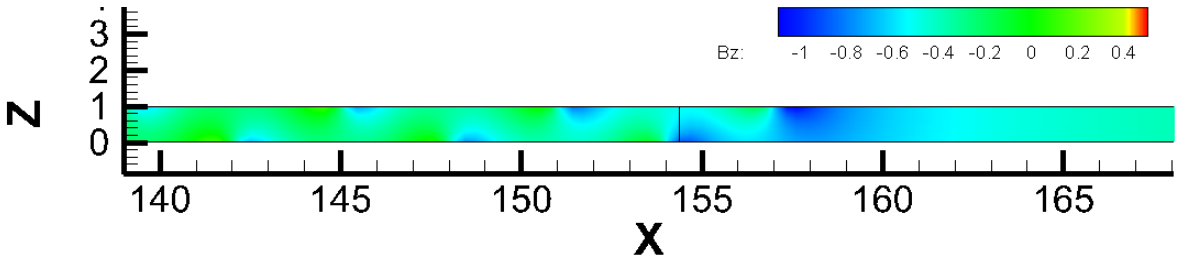

(c) Configuration C

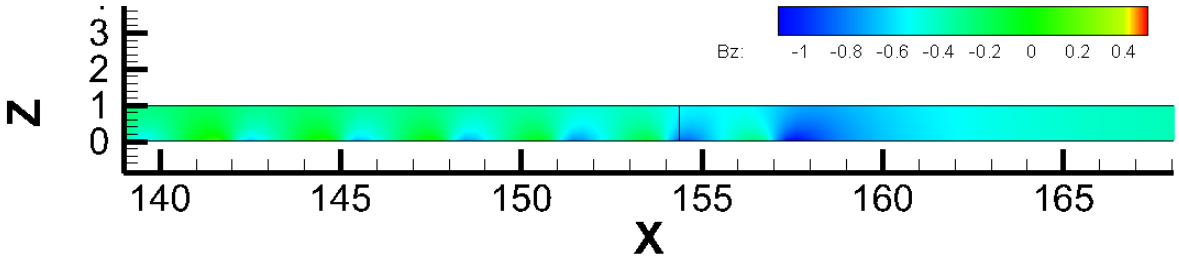

(d) Configuration D

Figure 6-6: Magnetic field component in z direction in the four configuration

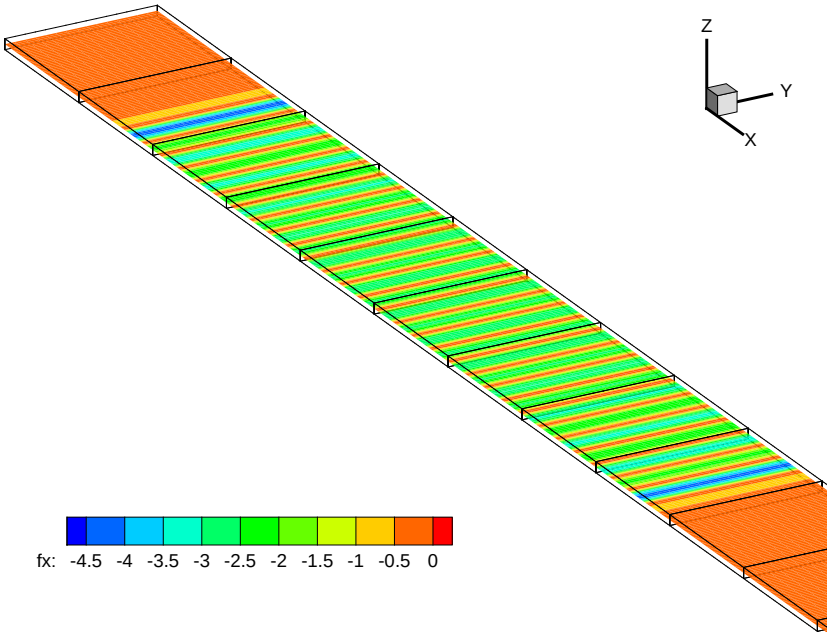

Figure 6-7: Lorentz force x direction component in $x - y$ plane

only not zero component of the current density is the one in y direction. The components in x and in z directions are equal to zero in all the domain. The electric conductivity of the walls is therefore an irrelevant parameter.

6-2-3 Lorentz force

As it is mentioned at the beginning of the Chapter 4 the Lorentz force is generally directed so as to inhibit the relative movement of the magnetic field and the fluid. The force in x direction, shown in Figures 6-9 (b), is, indeed, negative in all the domain. There are oval shape areas, located in the same position of the ones for the current, with a value of the force around -2.5. Outside these areas the force is about -0.5.

Figure 6-9 (c) shows the z component of the Lorentz force. At the right hand of each wire a little almost circular area is generated with positive values of this force component. The same shape area with negative values is at the left hand of each wire. Outside these areas the force in z direction is about equal to zero.

The Lorentz force component in y direction is equal to zero in all the domain.

6-2-4 Velocity

Figure 6-10 (a) shows the x direction component of the velocity. To highlight its weak dependence on x coordinate, the part of the channel with $40 \leq x \leq 90$ is shown and the ratio between z and x axis is much lower than 1. Respect with other figures, moreover, the coloring is banded rather than continuous. Figure 6-10 (a) shows u as function of z coordinate

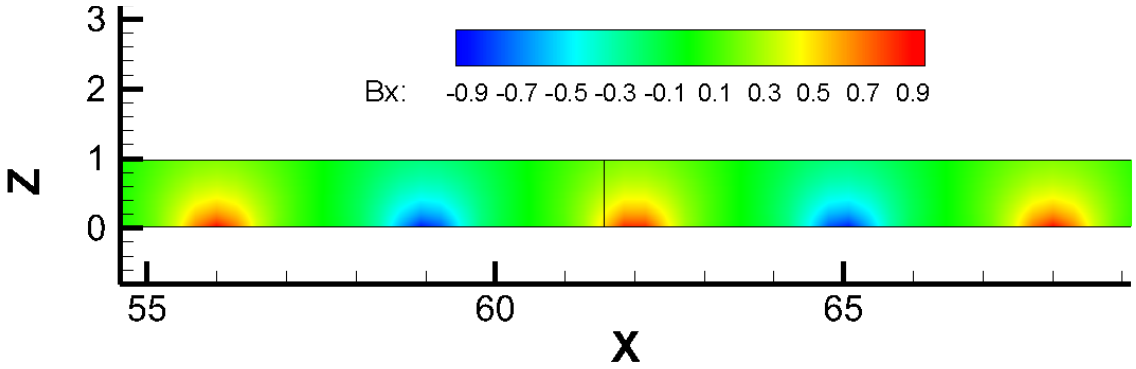

(a) magnetic field component in x direction

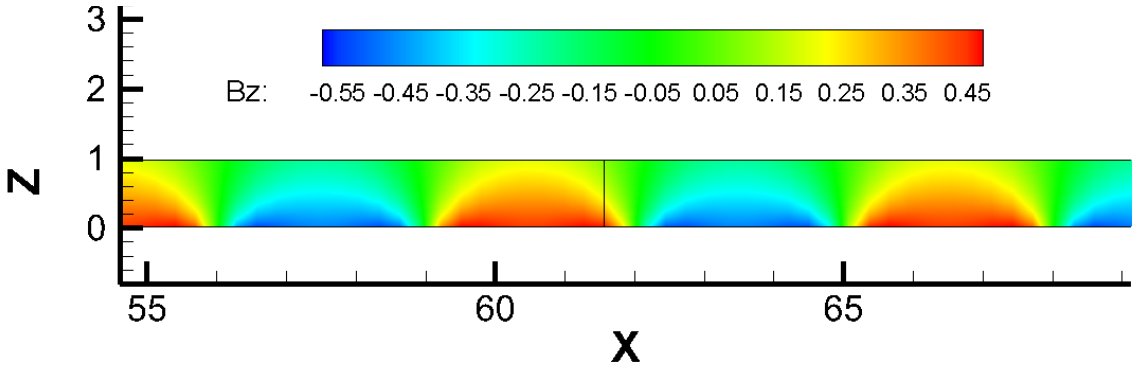

(b) magnetic field component in z direction

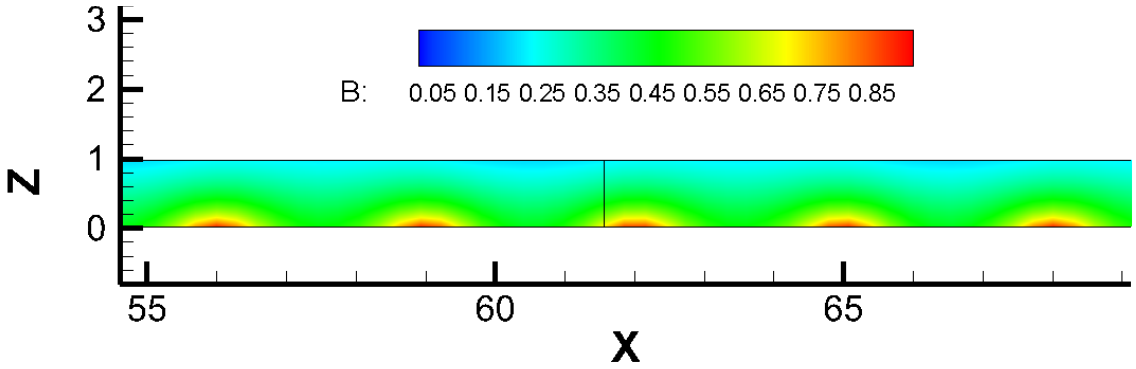

(c) magnetic field modulus

Figure 6-8: Magnetic field

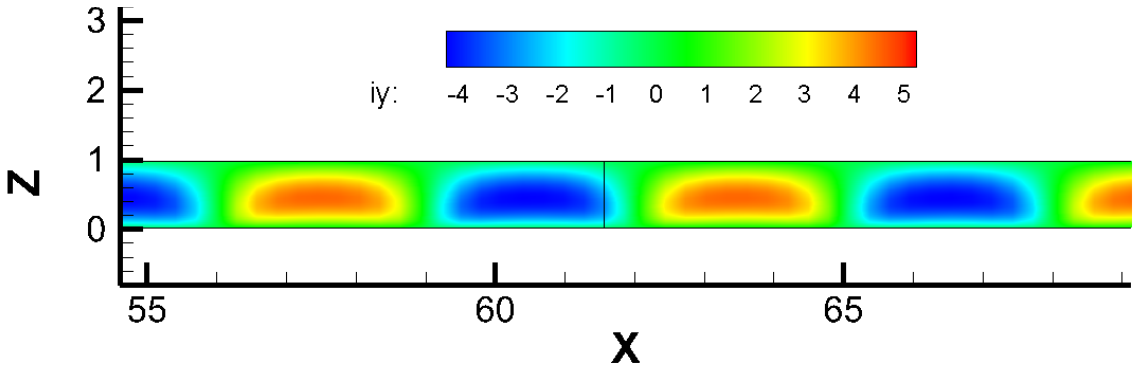

(a) electric current density in y direction

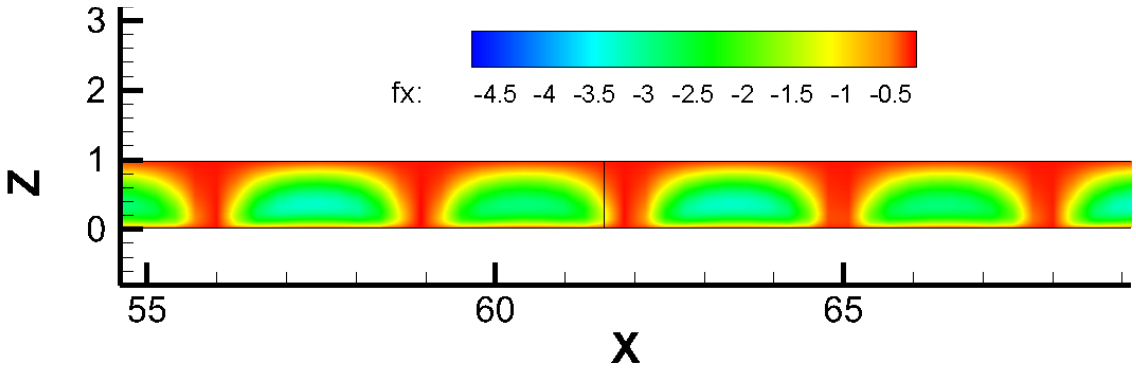

(b) Lorentz force component in x direction

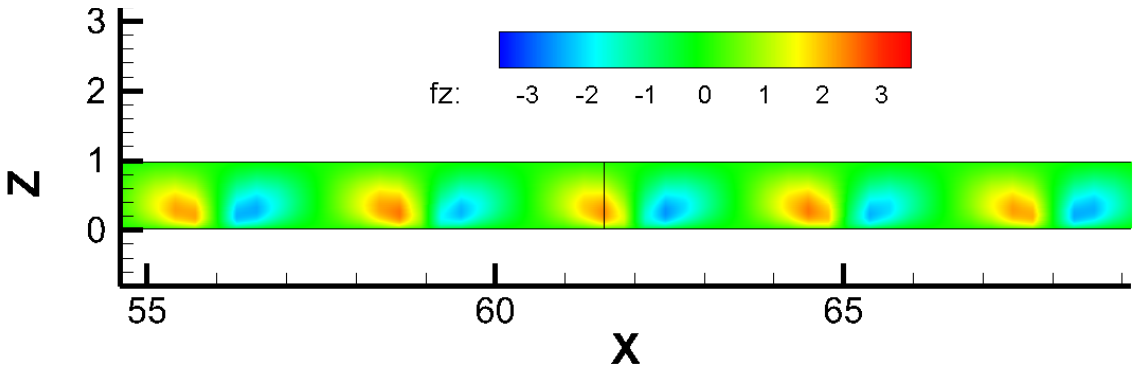

(c) Lorentz force component in z direction

Figure 6-9: Current density and Lorentz force

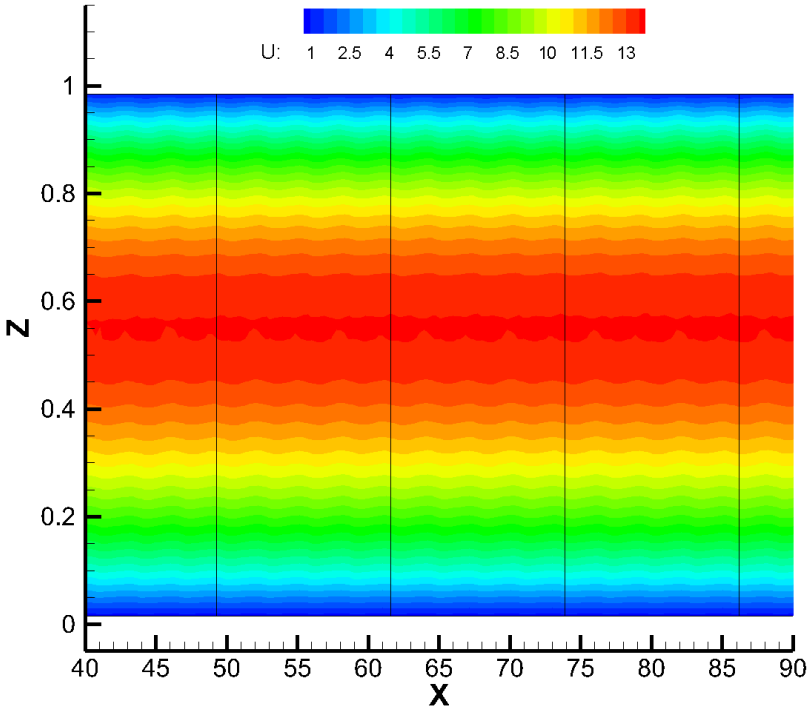

(a) velocity component in x direction

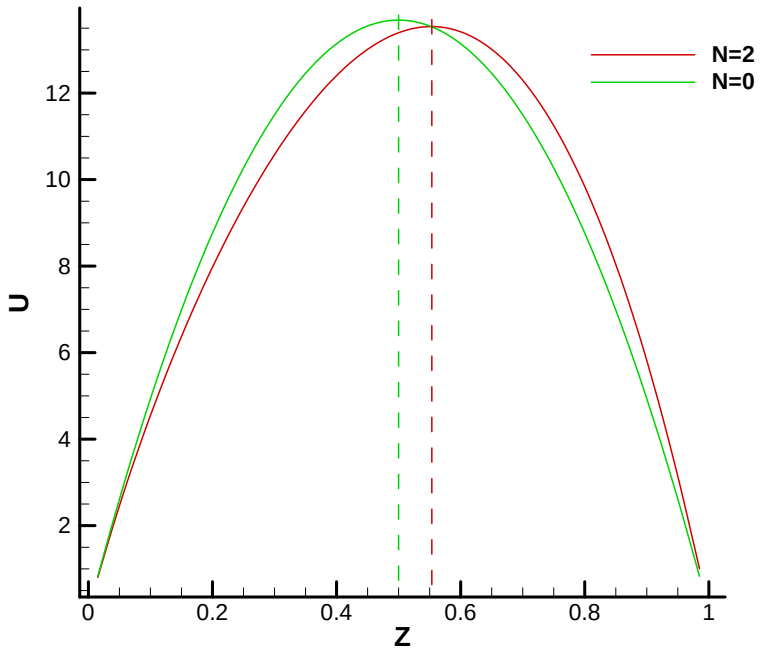

(b) Velocity profiles for N=0 and N=2 in $x = 65$

Figure 6-10: Velocity component in x direction

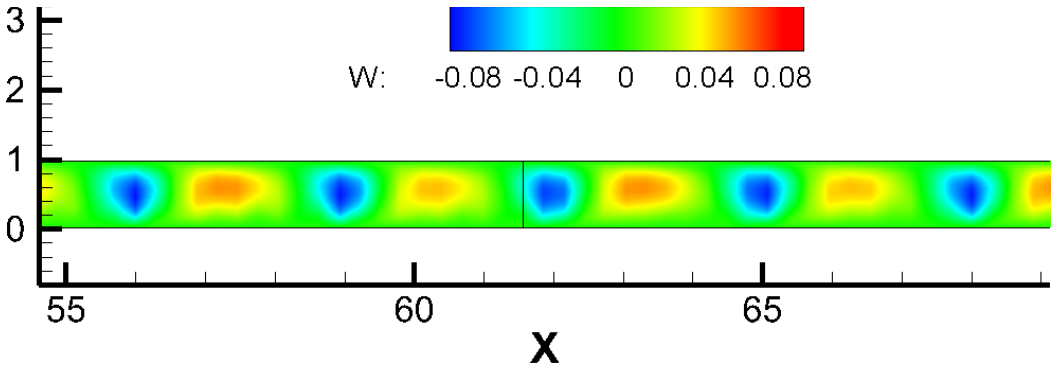

(a) velocity component in z direction

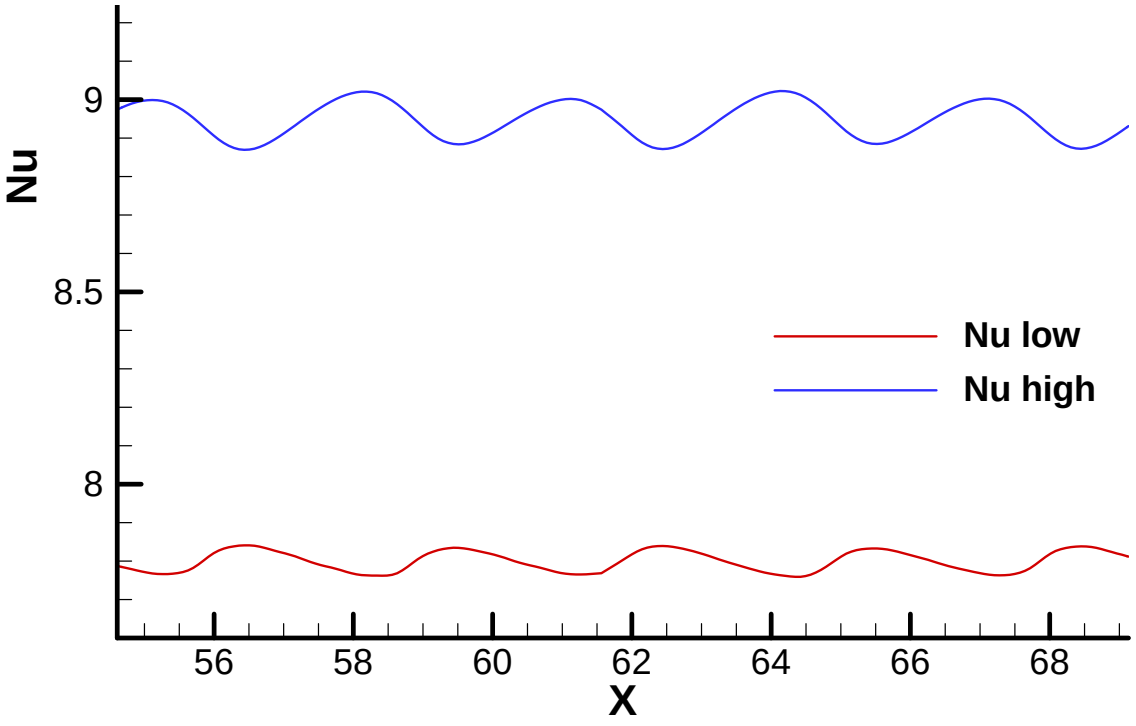

(b) Nusselt number profiles

Figure 6-11: Velocity components fields and Nusselt number profiles

in $x = 65$. Only one velocity profile is given since, as it was said, it depends really slightly on x. The velocity profile is not exactly symmetric respect to the centerline, but it is slightly perturbed. The velocity increases in the high half of the channel and decreases in the low half. The magnetic field influences the average Nusselt number by means of the effect on the velocity in streamwise direction. The increase of the velocity in the high half of the channel promotes the convection on the upper wall as well as the decrease of the velocity in the low half inhibits it on the lower wall.

The velocity component in z direction is shown in Figure 6-11 (a). Almost circular shape areas with negative values are in correspondence of the wires position. They alternate with bigger, almost circular shape areas with positive values. Outside these areas the velocity component in z direction is about equal to zero. This velocity component is responsible for the oscillations of the Nusselt number. Figures 6-11 (b) and (c) show that the maximum of Nusselt number oscillations on the upper and higher wall are immediately after areas with flow impinging against the considered wall. The oscillations on the upper wall are bigger than on the lower wall because the areas with velocity impinging on the upper wall are wider. The period of oscillations is equal to the dimensionless distance between wires, which is equal to 3 in this case.

The velocity component in y direction is equal to zero in all the domain.

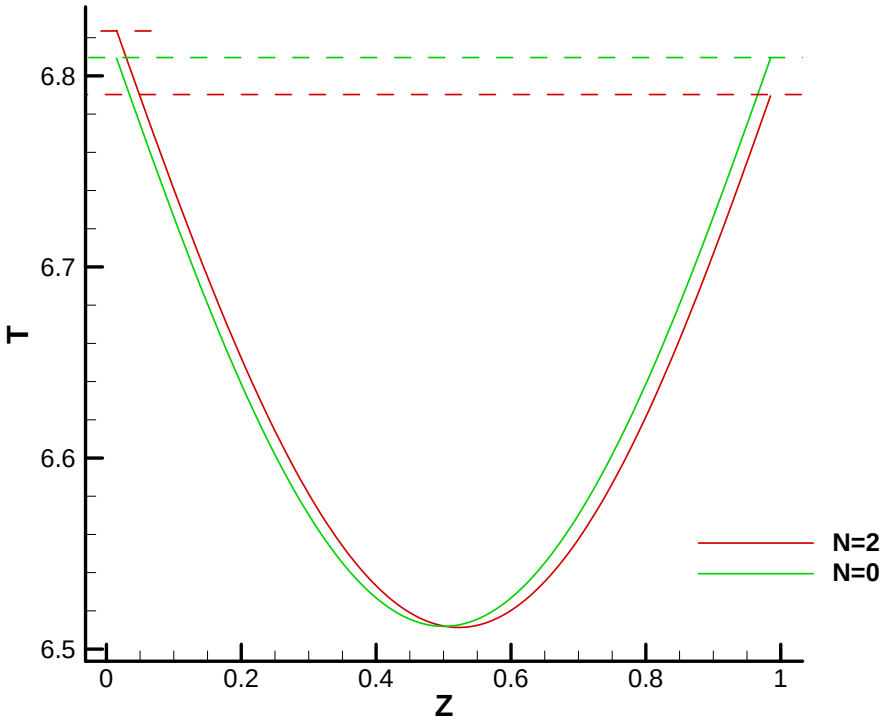

Figure 6-12: Temperature profiles for N=0 and N=2 in $x = 65$

6-2-5 Temperature profile

The red curve in Figure 6-12 represents the temperature profile in $x = 65$. While in the non magnetic case (green curve) the temperature profile is perfectly symmetric, for $N = 2$ it is not. Indeed the temperature on the upper wall ($z = 1$) is less than 1 % lower than the non magnetic case.

6-3 The selected configuration - parametric study

In this section the influence of the relevant dimensionless parameters, characterizing the studied phenomenon, on the convective heat transfer is analyzed. These parameters are:

- Re (Reynolds number)
- N (Stuart number)
- Pr (Prandtl number)
- dw (distance between wires in x direction) = 3
- dwz (distance between wires and walls) = 0.5

The effect on the Nusselt number profiles on lower and upper wall of these parameters is shown and commented. Wires configuration A was always used in the simulations whose results are presented.

6-3-1 Influence of Reynolds number

Figure 6-13 gives Nusselt profiles for four different values of Reynolds number (250, 500, 750 and 1000). The other parameters, kept the same for all the four cases, are:

- nw (number of wires) = 30
- dw (distance between wires in x direction) = 3
- dwz (distance between wires and walls) = 0.5
- mfw (x coordinate of first wire) = 20
- mlw (channel length after last wire) = 90
- $Pr = 0.03$
- $N = 2$

It is recalled that the parameters dw, dwz, mfw and mlw are dimensionless, being L_z the reference length.

As it is explained in Chapter 5, the dimensionless bulk velocity, being u_τ the reference velocity, is given by $u_b = (Re/6)^{1/2}$. Therefore the by increasing the Reynolds number the velocity increases. According to the Ohm's law introduced in Chapter 4, the higher the velocity the higher the electric current density induced into the flow and therefore the higher the Lorentz force.

$$\mathbf{J} = -\nabla V + \mathbf{u} \times \mathbf{B_{imp}}$$

If the velocity increases the action of the magnetic filed on the velocity field rises and consequently also the effect on the Nusselt number becomes stronger. As the Reynolds number rises the development length required for the stabilization of the average Nusselt number increases. Also the space required after the last wire to make the Nusselt number go back to the value 8.235 increases with the Reynolds number. The amplitude of oscillations around the average value, conversely, slightly decreases as the Reynolds number goes up.

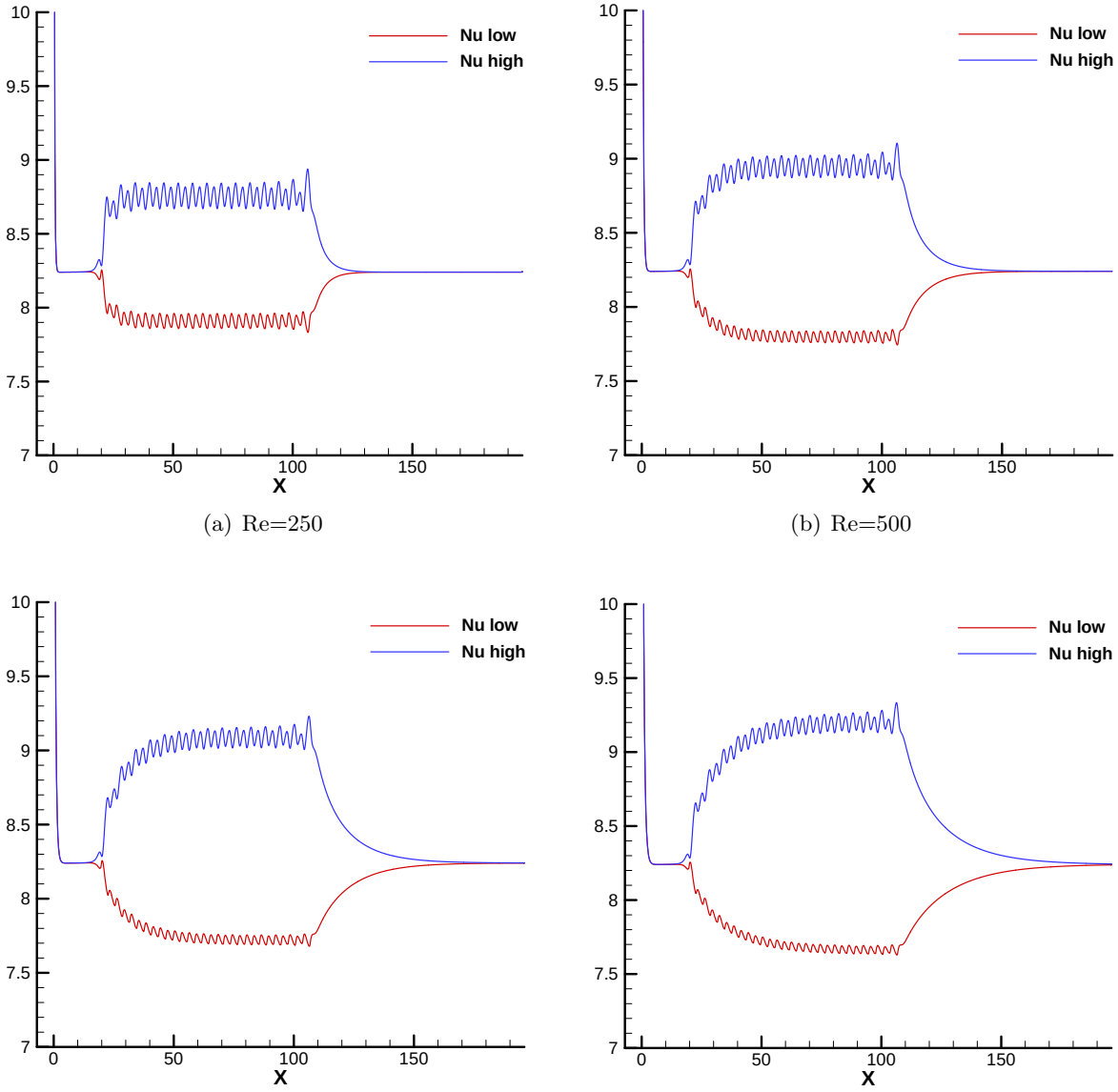

(a) Re=250

(b) Re=500

(c) Re=750

(d) Re=1000

Figure 6-13: Reynolds number influence on Nusselt number profiles

6-3-2 Influence of Prandtl number

Figure 6-14 gives Nusselt profiles for two different values of Prandtl number (0.005 and 0.03), representative of the typical values of liquid metals. The other parameters, kept the same, for all the two cases are:

- nw (number of wires) = 30
- dw (distance between wires in x direction) = 3
- dwz (distance between wires and walls) = 0.5
- mfw (x coordinate of first wire) = 20
- mlw (channel length after last wire) = 90
- $Re = 1000$
- $N = 2$

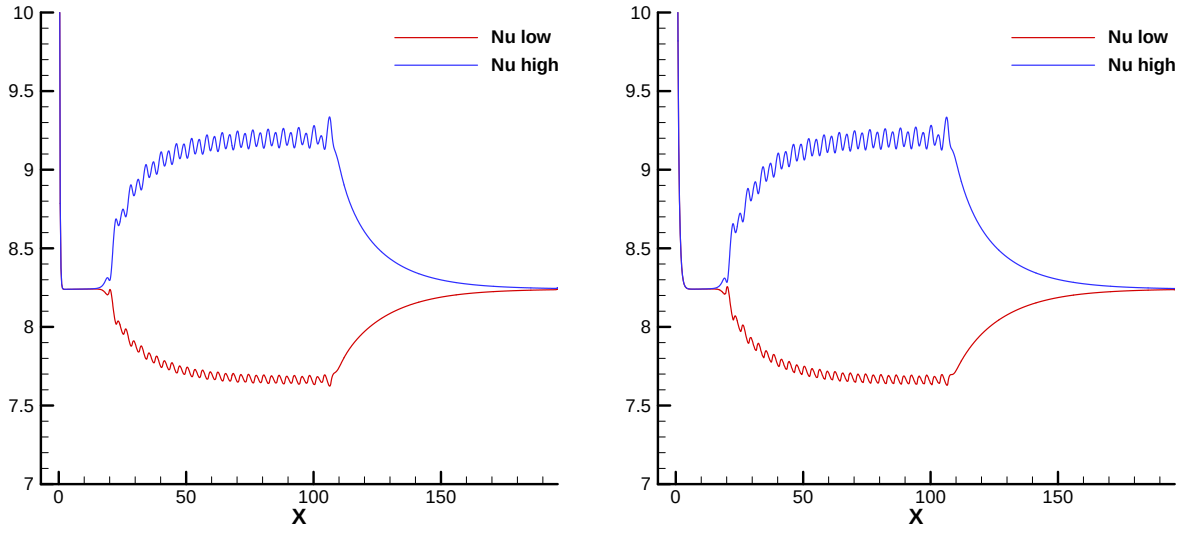

(a) Pr=0.005 (b) Pr=0.03

Figure 6-14: Prandtl number influence on Nusselt number profiles

The Figure 6-14 (a) and (b) are hardly distinguishable, although the two considered value differ of an order of magnitude. The Prandtl number turns, therefore, out to be an almost irrelevant parameter in the context of liquid metals. In Figure 6-14 it is, however, evident that for Pr=0.03 the thermal entrance length is greater than for Pr=0.005. The oscillations amplitude is slightly greater for Pr=0.03. After the first wire the average Nusselt number increases a bit more quickly for Pr=0.005 and a bit more quickly it goes back to the undisturbed value (8.325) as well.

6-3-3 Influence of Stuart number

Figure 6-15 gives Nusselt profiles for four different values of Stuart number (0.5, 2, 5 and 8). The other parameters, kept the same for all the four cases, are:

- nw (number of wires) = 30
- dw (distance between wires in x direction) = 3
- dwz (distance between wires and walls) = 0.5
- mfw (x coordinate of first wire) = 20
- mlw (channel length after last wire) = 90
- $Re = 1000$
- $Pr = 0.005$

By increasing the Stuart number the dimensionless Lorentz force in the momentum equation rises. The action of the magnetic field on the velocity field is enhanced and consequently also the effect on the Nusselt number gets stronger. The Stuart number value does not influence the length required for the stabilization of the average Nusselt number. The amplitude of oscillations around the average value, conversely, increases significantly as the Stuart number goes up.

It is of fundamental importance to estimate the dimensional order of magnitude of the imposed magnetic field that generates the shown effect on the Nusselt number in order to evaluate the feasibility of the proposed innovative system for the heat transfer enhancement. The symbol * is used in the rest of this subsection as superscript of dimensionless values in order to distinguish them from dimensional values.

By the Stuart number definition and by Equations 5-22 the magnetic field reference value (B_0) can be calculated as follows

$$N = \frac{\sigma\ B_0^2\ L_z}{\rho\ u_\tau} \quad \rightarrow$$

$$\rightarrow \quad B_0 = \left(\frac{N\ \rho\ u_\tau}{\sigma L_z}\right)^{1/2} = \left(\frac{N\ \rho\ \dfrac{\nu}{L_z}\sqrt{6\ Re}}{\sigma L_z}\right)^{1/2} = \left(\frac{N\ \mu}{\sigma\ L_z^2}\sqrt{6\ Re}\right)^{1/2} \quad \rightarrow$$

$$B_0 = \frac{1}{L_z}\left(\frac{N\mu}{\sigma}\right)^{1/2}\ (6\ Re)^{1/4} \tag{6-1}$$

The maximum value of the dimensionless magnetic field modulus inside the channel is 0.9 (see Figure 6-8 (c)). The dimensional value can be calculated as it follows:

$$B_{max} = B_0 \cdot B^*_{max} \tag{6-2}$$

The fluid flowing into the channel influences the value of B_0 trough the ratio μ/σ.

The sodium was chosen for this calculation because among the eight metals considered in Chapter 3 it has the lowest value of this ratio, therefore it allows the lowest value of B_0. The properties of sodium were evaluated at 400 °C.

Values of the dimensional and dimensionless parameters appearing in the Equation 6-2 are therefore:

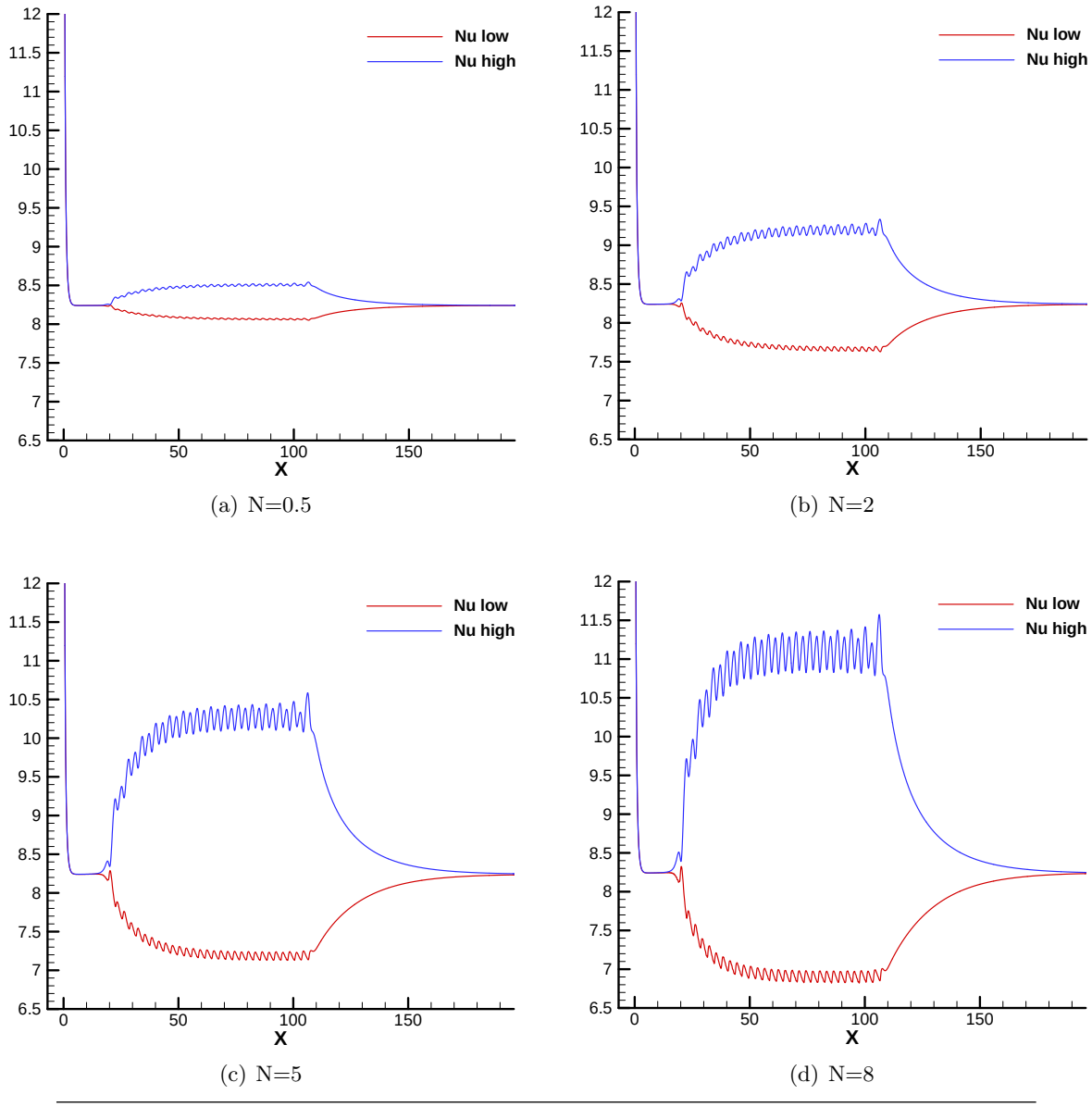

(a) N=0.5

(b) N=2

(c) N=5

(d) N=8

Figure 6-15: Stuart number influence on Nusselt number profiles

N	Δ % Nu_{high}	Δ % Nu_{low}	B_{max} [T]
0.5	+3.2	-2.5	0.027
2	+11.7	-6.7	0.054
5	+25	-12.8	0.087
8	+35	-16	0.109

Table 6-1: Dimensional magnetic field intensity

- $Re = 1000$
- $L_z = 5\ mm$
- $\sigma = 4.64 \cdot 10^6\ (\Omega \cdot m)^{-1}$
- $\mu = 0.271\ mPa \cdot s$

Being $L_z = 5mm$ it results also:

- $dw = dw^* \cdot L_z = 3 \cdot L_z = 15\ mm$
- $dwz = dwz^* \cdot L_z = 0.5 \cdot L_z = 2.5\ mm$

Table 6-1 shows for each of the four considered Stuart number the Nusselt number percentage variation on the upper and the lower wall. The the maximum value of the magnetic field modulus inside the channel is given.

With a magnetic field whose maximum value inside the channel is slightly higher than 0.1 Tesla an increase of 35 % of Nusselt number is achieved at the upper wall. Magnetic fields of such intensity are easily obtainable with common permanent magnets. Therefore the conducted analysis demonstrates the feasibility of the innovative system proposed for the cooling enhancement.

6-3-4 Influence of distance between wires

As it was explained in the first section of this chapter, one of the first actions made on the code was to allow to directly set the distance between. Its influence on the Nusselt number is shown in Figure 6-16. The four different value of dimensionless inter-wires distance are 2, 3, 4 and 5. The space occupied by wires was kept about equal to 87 in all four cases, so the number of wires was respectively 45, 30, 23 and 18. The other parameters, kept the same for all the four cases, are:

- nw (number of wires) = 30
- dwz (distance between wires and walls) = 0.5
- mfw (x coordinate of first wire) = 20
- dwz (channel length after last wire) = 90

- $Re = 1000$
- $Pr = 0.03$
- $N = 2$

The effect on the Nusselt number become stronger as the wires get closer to each other. The amplitude of oscillations around the average value, conversely, decreases as the distance between wires decreases. As already noticed, the period of oscillations is equal to the distance between wires, so ,as it is easy to see in Figure 6-16 it is higher as the distance between wires increases.

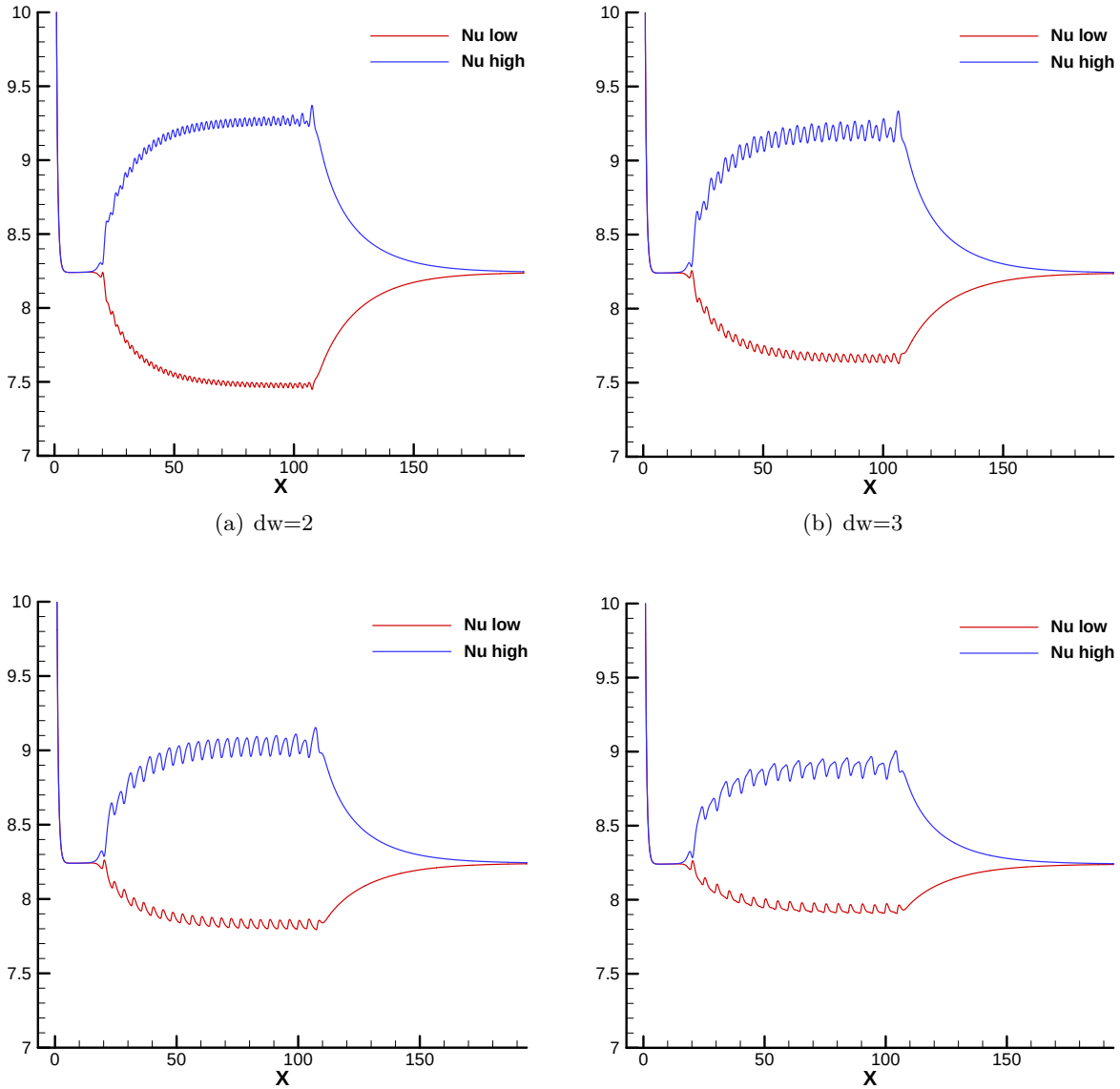

(a) dw=2 (b) dw=3

(c) dw=4 (d) dw=5

Figure 6-16: Distance between wires influence on Nusselt number profiles

6-3-5 Influence of wires distance from the walls

The last parameter analyzed is the distance of wires from the wall. The influence of this parameter on the Nusselt number profiles is shown in figure Figure 6-17. The four different value of dimensionless distance between wires and walls are 0.25, 0.5, 0.75 and 1.

The other parameters, kept the same for all the four cases, are:

- nw (number of wires) = 30
- dw (distance between wires in x direction) = 3
- mfw (x coordinate of first wire) = 20
- dwz (channel length after last wire) = 90
- $Re = 1000$
- $Pr = 0.03$
- $N = 2$

The magnetic field intensity in a certain point increases as the distance from the wire decreases (Biot-Savart law). Indeed the lower the distance of wires from the wall, the stronger the effect on the Nusselt number. Both average value and oscillations decrease as the distance of the wires from the wall increases. As Figure 6-17 shows the influence of this parameter on the Nusselt number profiles is very strong.

6-3-6 Parametric analysis synthesis

Figure 6-18 shows the average Nusselt number on the upper and on the lower wall as function of Re, N, dw and dwz.

The curves with Re, N and dwz on the horizontal axis have derivative decreasing in module. The one with dw on the horizontal axis is approximately linear.

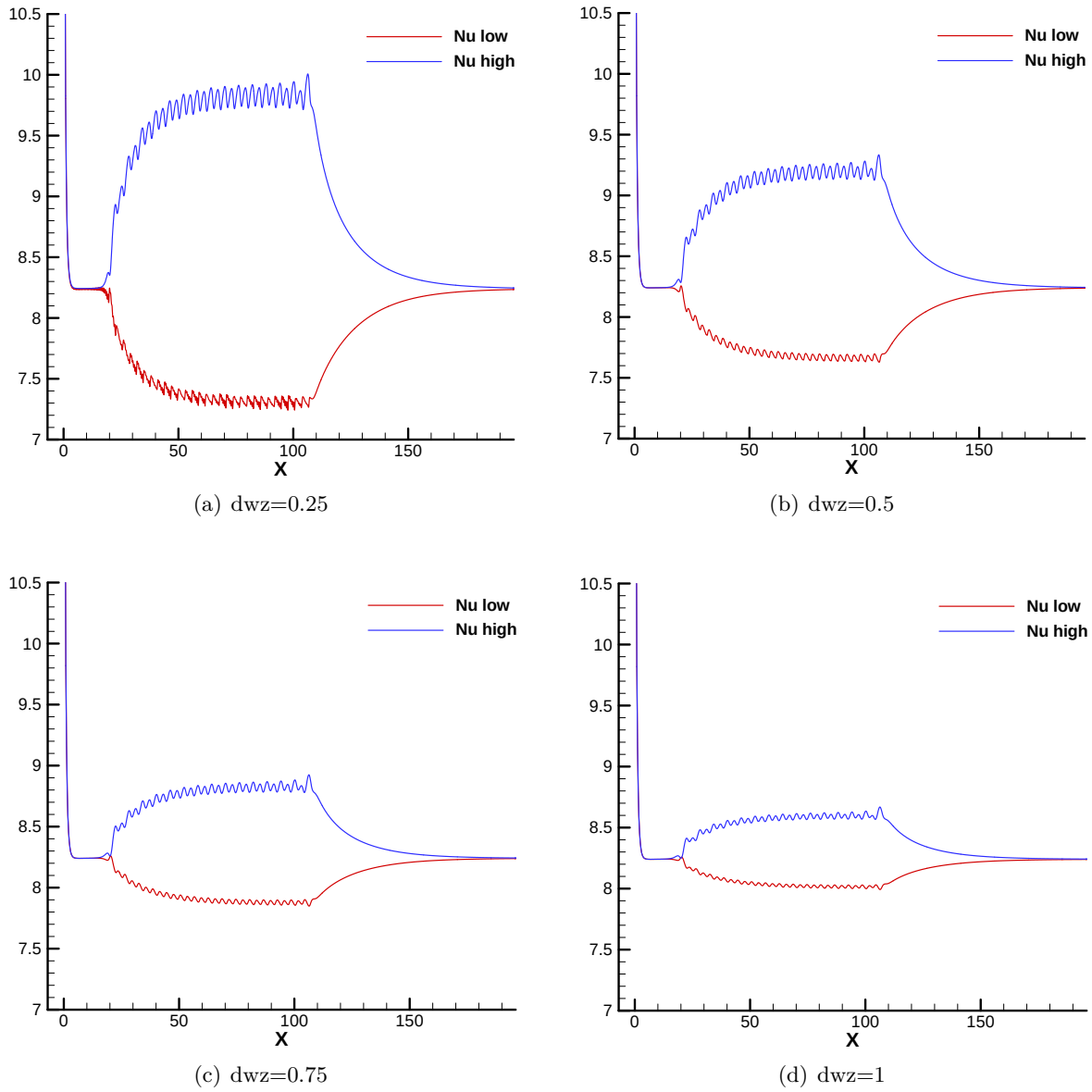

(a) dwz=0.25

(b) dwz=0.5

(c) dwz=0.75

(d) dwz=1

Figure 6-17: Distance between wires and walls influence on Nusselt number profiles

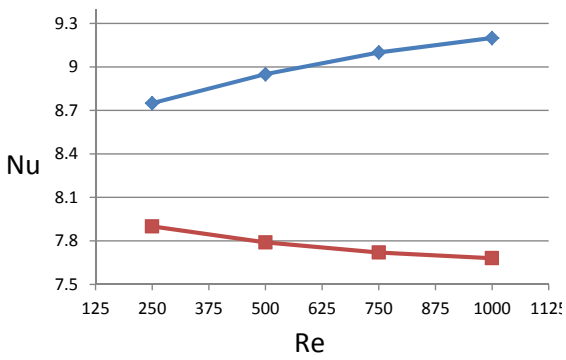

(a) Reynolds number

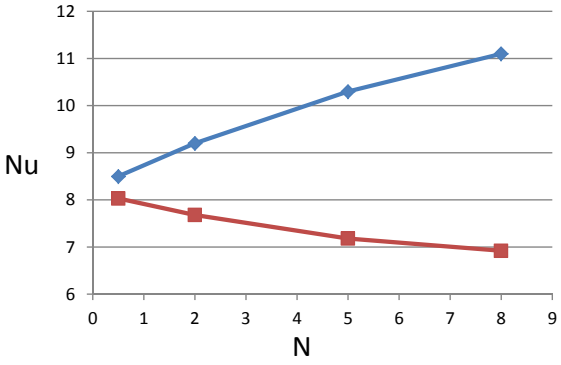

(b) Stuart number

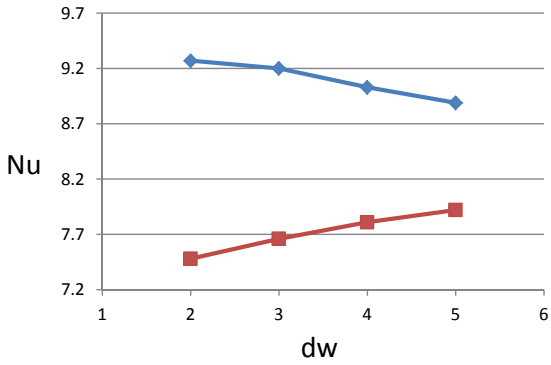

(c) Distance between wires

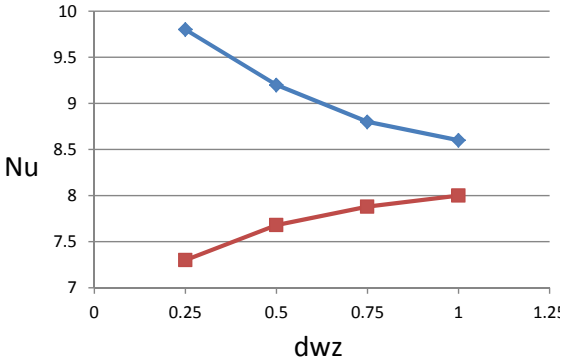

(d) Distance between wires and wall

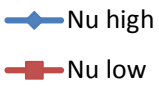

(e) Legend

Figure 6-18: Influence of analyzed parameters on the average Nusselt number

Chapter 7

Conclusions

This thesis work presents an innovative system for enhancing the cooling of turbine blades with liquid metals. The idea is to exploit the high electric conductivity of liquid metals acting on their flow by means of non-uniform magnetic fields.

A simplified evaluation of the high potential of liquid metals as coolants is performed. A circular duct with hot air in external cross flow is simulated to be cooled by air and by different liquid metals. The temperature of the cylindric wall exceeds 900 °C with air as coolant, while liquid metals are able to keep the wall temperature much lower. Lithium, even in laminar regime, maintains the maximum wall temperature slightly above 600 °C. The excellent heat transfer properties of liquid metals would allow much higher TITs, therefore higher cycle efficiencies, than the ones currently achievable with air cooling systems. Not only an increase of the TIT could be possible, but also a lower hot sections part temperature, then a relevant cost reduction of the equipment, because less expensive materials could be employed. Moreover, the magnetic field generation becomes more and more critical as the temperature increases, thus having low blades temperatures is important also for this reason.

By means of a DNS code a laminar liquid metal flow between two parallel plates is studied. Ideal current-carrying wires generate a non-uniform magnetic field inside the channel. They are positioned behind the channel plates and are directed orthogonally to the flow. Four different wires configurations are compared on the basis of their effect on the convective heat transfer. The magnetic field generated by wires all positioned behind the same wall, with currents direction alternating, produces the most interesting effect on the Nusselt number profile. This configuration allows a considerable enhancement of the heat transfer at the wall opposite to the one behind which the wires are positioned. The Nusselt number increases rapidly when the flow encounters the magnetic field. The heat transfer coefficient slightly oscillates around a constant value. The others configurations produce more irregular profiles of the Nusselt number or with a lower increase in the average value.

The influence of some dimensionless parameters characterizing the phenomenon on the heat transfer enhancement for the selected configuration is assessed. These parameters are: Reynolds number (Re), Stuart number (N), Prandtl number (Pr), distance between wires (dw), distance of wires from plate (dwz). The Prandtl number in the typical values range of liquid

metals ($10^2 \div 10^{-3}$) does not influence significantly the effect of the magnetic field on the Nusselt number. All the other parameters are, on the contrary, relevant. The average Nusselt number rises as Re and N increase and as dw and dwz decrease. The oscillations amplitude always grows when the average Nusselt number is higher, except for the parameter dw. When the wires get closer two benefits are gained: an increase of the average Nusselt number and a reduction of oscillations amplitude.

Finally the analysis of a dimensional case was performed, namely a Sodium flow, between plates distant 5 mm each other, in laminar regime ($Re_{D_H} = 2000$). An augmentation of the Nusselt number of 35 % can be reached by means of a magnetic field whose maximum value inside the channel is 0.11 Tesla. The magnetic field intensity required is inversely proportional to the distance between the plates.

The proposed system has a further advantage if the magnetic field is produced by electric currents. In that case, in fact, it is also possible to adjust the cooling intensity according to the thermal loads on the blades.

Appendix A

Metal properties

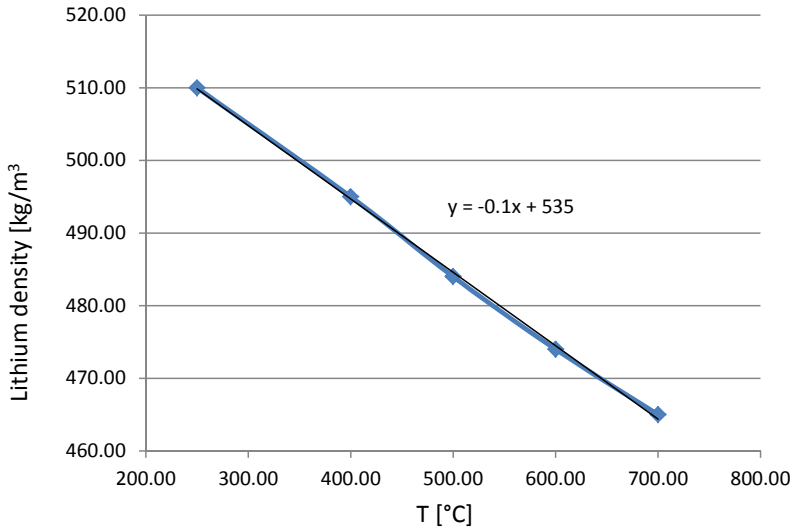

(a) Lithium density

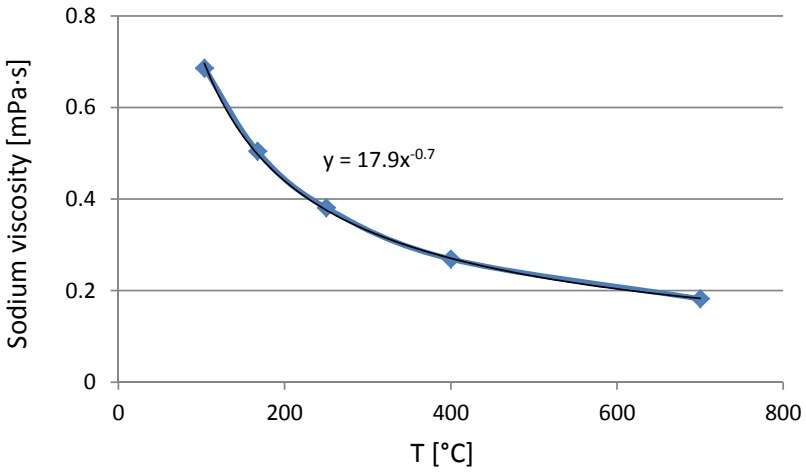

(b) Sodium viscosity

Figure A-1: Lithium density and sodium viscosity curves

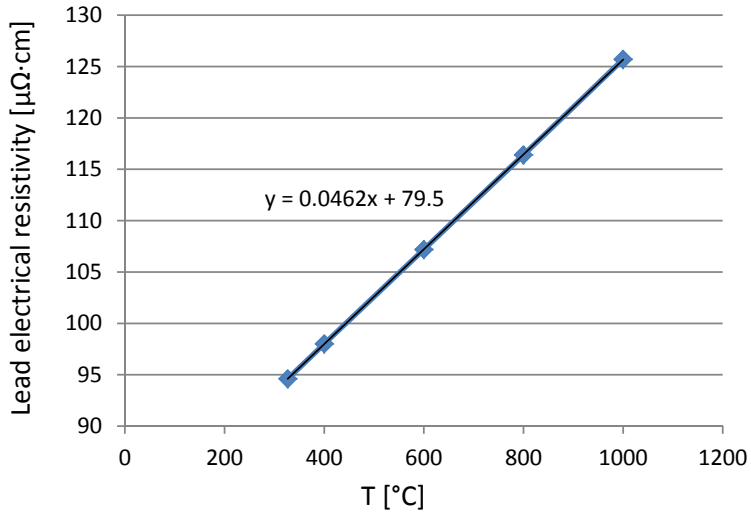

(a) Lead electrical resistivity

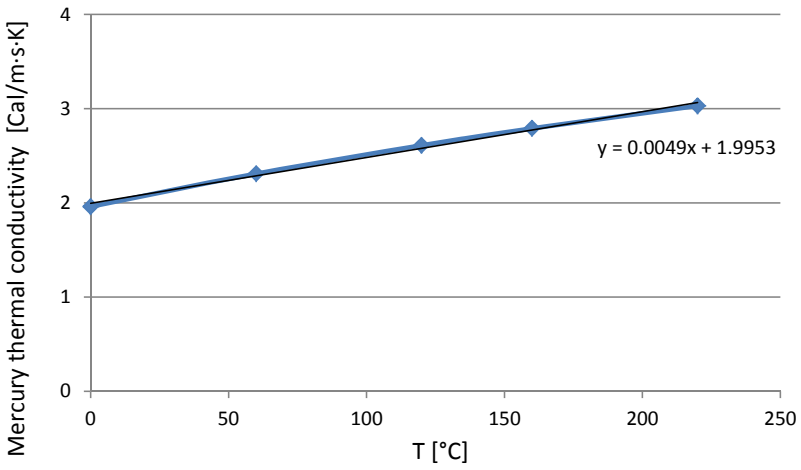

(b) Mercury thermal conductivity

Figure A-2: Lead electrical resistivity and mercury thermal conductivity curves

BISMUTH	Points	Range	Interpolated function
Density $\left[\frac{kg}{m^3}\right]$	3	$300 \leq T \leq 1000$	$\rho = 10450 - 1.32\ T$
Electrical resitivity $[\mu\Omega \cdot cm]$	4	$300 \leq T \leq 750$	$\rho_{el} = 0.0548\ T + 112$
Heat capacity $\left[\frac{cal}{kg \cdot K}\right]$	/	$280 \leq T \leq 700$	$c_p = 36$
Thermal conductivity $\left[\frac{cal}{m \cdot s \cdot K}\right]$	3	$300 \leq T \leq 650$	$k = 0.00214\ T + 2.86$
Viscosity $[mPa \cdot s]$	3	$304 \leq T \leq 600$	$\mu = 2.34e^{-6}\ T^2 - 0.00437\ T + 2.77$

Table A-1: Properties Bismuth

CADMIUM	Points	Range	Interpolated function
Density $\left[\frac{kg}{m^3}\right]$	3	$330 \leq T \leq 600$	$\rho = -0.1069\ T + 836.05$
Electrical resitivity $[\mu\Omega \cdot cm]$	5	$325 \leq T \leq 700$	$\rho_{el} = 9e^{-11}\ T^4 - 2e^{-7}\ T^3 + 0.0002\ T^2 - 0.0671\ T + 42.619$
Heat capacity $\left[\frac{cal}{kg \cdot K}\right]$	/	$322 \leq T \leq 1000$	$c_p = 63.2$
Thermal conductivity $\left[\frac{cal}{m \cdot s \cdot K}\right]$	3	$355 \leq T \leq 435$	$k = 0.0003\ T^2 - 0.234\ T + 53.4$
Viscosity $[mPa \cdot s]$	4	$350 \leq T \leq 600$	$\mu = 2.62e^{-6}\ T^2 - 0.00577\ T + 4.06$

Table A-2: Properties Cadmium

GALLIUM	Points	Range [°C]	Interpolated function
Density $\left[\frac{kg}{m^3}\right]$	3	$30 \leq T \leq 1100$	$\rho = 6105 - 0.691\ T + 8.3 \cdot 10^{-5}\ T^2$
Electrical resitivity $[\mu\Omega \cdot cm]$	3	$29.75 \leq T \leq 46.1$	$\rho_{el} = 0.117\ T + 23$
Heat capacity $\left[\frac{cal}{kg \cdot K}\right]$	/	$30 \leq T \leq 1100$	$c_p = 82$
Thermal conductivity $\left[\frac{cal}{m \cdot s \cdot K}\right]$	3	$... \leq T \leq ...$	$k = 8$
Viscosity $[mPa \cdot s]$	5	$52.9 \leq T \leq 806$	$\mu = -5.61e^{-9}\ T^3 + 1.016^{-5}\ T^2 - 0.00648\ T + 2.21$

Table A-3: Properties Gallium

LEAD	Points	Range [°C]	Interpolated function
Density $\left[\frac{kg}{m^3}\right]$	5	$400 \leq T \leq 1000$	$\rho = -1.16\ T + 10973$
Electrical resitivity $[\mu\Omega \cdot cm]$	5	$327 \leq T \leq 1000$	$\rho_{el} = 0.0462\ T + 79.511$
Heat capacity $\left[\frac{cal}{kg \cdot K}\right]$	/	$400 \leq T \leq 800$	$c_p = 35.2$
Thermal conductivity $\left[\frac{cal}{m \cdot s \cdot K}\right]$	4	$400 \leq T \leq 800$	$k = 8.33e^{-6}\ T^2 - 0.00728\ T + 5.21$
Viscosity $[mPa \cdot s]$	5	$441 \leq T \leq 844$	$\mu = 4.68e^{-6}\ T^2 - 0.00832\ T + 4.87$

Table A-4: Properties Lead

LITHIUM	Points	Range [°C]	Interpolated function
Density $\left[\frac{kg}{m^3}\right]$	5	$250 \leq T \leq 700$	$\rho = -0.101\ T + 535$
Electrical resitivity $[\mu\Omega \cdot cm]$	/	$T = 230$	$\rho_{el} = 45.25$
Heat capacity $\left[\frac{cal}{kg \cdot K}\right]$	/	$200 \leq T \leq 1000$	$c_p = 1000$
Thermal conductivity $\left[\frac{cal}{m \cdot s \cdot K}\right]$	4	$250 \leq T \leq 700$	$k = 0.00119\ T + 10.8$
Viscosity $[mPa \cdot s]$	5	$183.4 \leq T \leq 285.5$	$\mu = 3.49e^{-6}\ T^2 - 0.00299\ T + 1.02$

Table A-5: Properties Lithium

MERCURY	Points	Range [°C]	Interpolated function
Density $\left[\frac{kg}{m^3}\right]$	5	$-20 \leq T \leq 300$	$\rho = -2.4\ T + 13594$
Electrical resitivity $[\mu\Omega \cdot cm]$	5	$50 \leq T \leq 350$	$\rho_{el} = 0.123\ T + 91.16$
Heat capacity $\left[\frac{cal}{kg \cdot K}\right]$	/	$0 \leq T \leq 450$	$c_p = 6.8e^{-5}\ T^2 - 0.0122\ T + 33.34$
Thermal conductivity $\left[\frac{cal}{m \cdot s \cdot K}\right]$	5	$0 \leq T \leq 220$	$k = 0.0049\ T + 2$
Viscosity $[mPa \cdot s]$	5	$-20 \leq T \leq 200$	$\mu = 1.58e^{-5}\ T^2 - 0.00656\ T + 1.69$

Table A-6: Properties Mercury

POTASSIUM	Points	Range [°C]	Interpolated function
Density $\left[\frac{kg}{m^3}\right]$	5	$64 \leq T \leq 1250$	$\rho = 841 - 0.217\ T - 2.7 \cdot 10^{-5}\ T^2 + 4.77 \cdot 10^{-9}\ T^3$
Electrical resitivity $[\mu\Omega \cdot cm]$	/	$93.3 \leq T \leq 1933.3$	$\rho_{el} = 7.99 + 6.37 \cdot 10^{-2}\ T - 1.4 \cdot 10^{-5}\ T^2 + 5.3 \cdot 10^{-8}\ T^3$
Heat capacity $\left[\frac{cal}{kg \cdot K}\right]$	/	$64 \leq T \leq 770$	$c_p = 200.4 - 0.0878\ T + 1.1 \cdot 10^{-4}\ T^2$
Thermal conductivity $\left[\frac{cal}{m \cdot s \cdot K}\right]$	5	$100 \leq T \leq 800$	$k = 10.5 - 5.3 \cdot 10^{-3}\ T + 2828/(T + 273.2)$
Viscosity $[mPa \cdot s]$	5	$69.6 \leq T \leq 700$	$\mu = 6.25\ T^{-0.581}$

Table A-7: Properties Potassium

SODIUM	Points	Range [°C]	Interpolated function
Density $\left[\frac{kg}{m^3}\right]$	3	$98 \leq T \leq 1370$	$\rho = 950.1 - 0.23\ T - 1.46 \cdot 10^{-5}\ T^2 + 5.64 \cdot 10^{-9}\ T^3$
Electrical resitivity $[\mu\Omega \cdot cm]$	/	$98 \leq T \leq 1100$	$\rho_{el} = 7.756 - 2.05 \cdot 10^{-2}\ T + 3.48 \cdot 10^{-5}\ T^2$
Heat capacity $\left[\frac{cal}{kg \cdot K}\right]$	/	$98 \leq T \leq 900$	$c_p = 343 - 0.139\ T + 1.1 \cdot 10^{-4}\ T^2$
Thermal conductivity $\left[\frac{cal}{m \cdot s \cdot K}\right]$	/	$98 \leq T \leq 890$	$k = 21.8 - 0.0117\ T$
Viscosity $[mPa \cdot s]$	5	$103.7 \leq T \leq 700$	$\mu = 17.9\ T^{-0.7}$

Table A-8: Properties Sodium

(a)

	Melting point (1 atm) [°C]	Boiling point (1 atm) [°C]	Density [kg/m^3]	Electrical resistivity [μΩ·cm]	Heat capacity [kJ/kg K]	Thermal conducivity [W/m K]	Kinematic Viscosity [m^2/s]	Thermal diffusivity [m^2/s]	Pr	μ_r (B.P.)
Bismuth	271	1477								
Cadmium	321,09	765								
Gallium	29,78	2403	6.071	28,88	0,34	33,49	3,15E-07	1,61E-05	0,0196	1,0000019
Lead	327,4	1744								
Lithium	180,54	1317								
Mercury	-38,87	356,58	13.474	97	0,14	9,38	1,04E-07	5,05E-06	0,0206	0,9999705
Potassium	63,63	774								
Sodium	97,81	892								
Air			16,2	$2.5\text{-}10^{32}$	1,03	0,028	1,23E-06	1,70E-06	0,7244	1,0000004

(b)

	Melting point (1 atm) [°C]	Boiling point (1 atm) [°C]	Density [kg/m^3]	Electrical resistivity [μΩ·cm]	Heat capacity [kJ/kg K]	Thermal conducivity [W/m K]	Kinematic Viscosity [m^2/s]	Thermal diffusivity [m^2/s]	Pr	μ_r (B.P.)
Bismuth	271	1477								
Cadmium	321,09	765								
Gallium	29,78	2403	6.003	40,59	0,34	33,49	2,41E-07	1,63E-05	0,0148	1,0000019
Lead	327,4	1744								
Lithium	180,54	1317								
Mercury	-38,87	356,58	13.235	110	0,14	11,43	8,05E-08	6,24E-06	0,0129	0,9999705
Potassium	63,63	774	808	17,41	0,79	68,42	4,21E-07	1,07E-04	0,0039	1,0000049
Sodium	97,81	892	915	11,61	1,36	83,78	5,88E-07	6,73E-05	0,0087	1,0000079
Air			12,3	$2.5\text{-}10^{32}$	1,03	0,035	1,97E-06	2,76E-06	0,7144	1,0000004

Table A-9: Thermophysical properties of metals and air at 50 °C (a) and 150 °C (b).

Properties of metals with melting point higher than the considered temperature are not shown. Air is considered to be at 15 bar. The last column shows the value of relative magnetic permeability at the melting point, so they do not change with temperature.

(a)

	Melting point (1 atm) [°C]	Boiling point (1 atm) [°C]	Density [kg/m^3]	Electrical resistivity [μΩ·cm]	Heat capacity [kJ/kg K]	Thermal conducivity [W/m K]	Kinematic Viscosity [m^2/s]	Thermal diffusivity [m^2/s]	Pr	μ_r (B.P.)
Bismuth	271	1477	9.988	131,55	0,15	15,12	1,53E-07	1,00E-05	0,0153	0,9999942
Cadmium	321,09	765	799	33,19	0,26	34,78	2,96E-06	1,65E-04	0,0180	0,9999837
Gallium	29,78	2403	5.873	64,01	0,34	33,49	1,61E-07	1,66E-05	0,0097	1,0000019
Lead	327,4	1744	10.565	95,68	0,15	15,42	2,41E-07	9,90E-06	0,0243	0,9999902
Lithium	180,54	1317	500	45,25	4,19	46,79	8,10E-07	2,24E-05	0,0362	1,0000226
Mercury	-38,87	356,58	12.755	134	0,16	15,53	1,05E-07	7,78E-06	0,0135	0,9999705
Potassium	63,63	774	762	30,86	0,77	55,01	2,73E-07	9,41E-05	0,0029	1,0000049
Sodium	97,81	892	868	19,20	1,29	73,98	3,42E-07	6,60E-05	0,0052	1,0000079
Air			8,3	$2.5 \cdot 10^{32}$	1,06	0,047	3,81E-06	5,30E-06	0,7194	1,0000004

(b)

	Melting point (1 atm) [°C]	Boiling point (1 atm) [°C]	Density [kg/m^3]	Electrical resistivity [μΩ·cm]	Heat capacity [kJ/kg K]	Thermal conducivity [W/m K]	Kinematic Viscosity [m^2/s]	Thermal diffusivity [m^2/s]	Pr	μ_r (B.P.)
Bismuth	271	1477	9.790	139,77	0,15	16,46	1,20E-07	1,12E-05	0,0108	0,9999942
Cadmium	321,09	765	783	33,05	0,26	48,04	2,34E-06	2,32E-04	0,0101	0,9999837
Gallium	29,78	2403	5.780	81,58	0,34	33,49	1,40E-07	1,69E-05	0,0083	1,0000019
Lead	327,4	1744	10.391	102,61	0,15	15,30	1,82E-07	9,99E-06	0,0182	0,9999902
Lithium	180,54	1317	485	45,25	4,19	47,54	8,29E-07	2,34E-05	0,0354	1,0000226
Mercury	-38,87	356,58	12.396	153	0,19	18,61	1,91E-07	8,11E-06	0,0236	0,9999705
Potassium	63,63	774	727	42,99	0,77	47,99	2,32E-07	8,57E-05	0,0027	1,0000049
Sodium	97,81	892	832	26,71	1,26	66,64	2,78E-07	6,34E-05	0,0044	1,0000079
Air			6,7	$2.5 \cdot 10^{32}$	1,10	0,055	5,46E-06	7,47E-06	0,7309	1,0000004

Table A-10: Thermophysical properties of metals and air at 350 °C (a) and 500 °C (b) .

Air is considered to be at 15 bar. The last column shows the value of relative magnetic permeability at the melting point, so they do not change with temperature.

Bibliography

[1] G. J. van Fossen Jr. and F. S. Stepka, "Liquid-cooling technology for gas turbines review and status.," *Proceedings of the Intersociety Energy Conversion Engineering Conference*, 1979.

[2] C. Henry and F. Bayley, "Heat-transfer problems of liquid-cooled gas-turbine blades," 1955.

[3] G. Lozza, *Turbine a gas e cicli combinati*. Esculapio, 2006.

[4] http://www.ligrani.com.

[5] M. Gallo, T. Astarita, and G. Carlomagno, "Thermo-fluid-dynamic analysis of the flow in a rotating channel with a sharp "u" turn," 2012.

[6] P. Davidson, *An Introduction to Magnetohydrodynamics*. Cambridge Texts in Applied Mathematics, Cambridge University Press, 2001.

[7] F. J. Bayley and B. W. Martin, "Review and status of liquid-cooling technology for gas turbines," 1970.

[8] J. Edwards, *Liquid and Vapour Cooling Systems for Gas Turbines*. Current papers, Stationery Office, 1970.

[9] en.wikipedia.org.

[10] www.magnet.fsu.edu.

[11] K. Buschow, *Encyclopedia of materials: science and technology*. No. v. 10 in Encyclopedia of Materials: Science and Technology, Elsevier, 2001.

[12] C. Kittel, *Introduction to Solid State Physics*. Wiley, 2005.

[13] A. Pashayev, C. Ardil, D. Askerov, R. Sadiqov, and A. Samedov, "Mathematical modeling of gas turbine blade cooling," *Azerbaijan National Academy of Aviation*, 2008.

[14] www.azom.com.

[15] S. Jarungthammachote, "Entropy generation analysis for fully developed laminar convection in hexagonal duct subjected to constant heat flux," *Energy*, vol. 35, no. 12, pp. 5374–5379, 2010. Cited By (since 1996):3.

[16] A. O. Ukanwa, "Diffusion in liquid metal systems - final report," *NASA contractor technical report*, 1975.

[17] R. n. Lyon United States Office of Naval Research. Committee on the Basic Properties of Liquid Metals, U. A. E. Commission, and U. S. N. D. B. of Ships, *Liquid-metals Handbook*. U.S. Government Printing Office, 1955.

[18] M. Shimoji, *Liquid metals: an introduction to the physics and chemistry of metals in the liquid state*. Academic Press, 1977.

[19] F. Incropera, *Fundamentals of Heat and Mass Transfer*. John Wiley & Sons Canada, Limited, 1993.

[20] W. Rohsenow, J. Hartnett, and Y. Cho, *Handbook of heat transfer*. McGraw-Hill handbooks, McGraw-Hill, 1998.

[21] R. Shah and A. London, *Laminar flow forced convection in ducts: a source book for compact heat exchanger analytical data*. Advances in heat transfer : Supplement, Academic Press, 1978.

[22] H. Versteeg and W. Malalasekera, *An introduction to computational fluid dynamics: the finite volume method*. Pearson Education Australia, 2007.

[23] J. Ferziger and M. Perić, *Computational methods for fluid dynamics*. Springer London, Limited, 2002.

[24] S. Ghiaasiaan, *Convective Heat and Mass Transfer*. Convective Heat and Mass Transfer, Cambridge University Press, 2011.

Glossary

List of Acronyms

MHD	Magnetohydrodynamics
DNS	direct mumerical simulation
TIT	Turbine Inlet Temperature
emf	Electromotive force